Severe Weather Intensity Index using the 1-km Global Environmental Multiscale Limited Area Model Output

by

Anna-Belle Filion

Department of Atmospheric and Oceanic Sciences

McGill University, Montréal

August 2013

A thesis submitted to the Faculty of Graduate Studies and Research in partial fulfillment of the requirements of the degree of Master of Science

Abstract

Severe weather (SW) can have a huge impact on someone's life and property. Presently at Environment Canada (EC), there is no useful automated tool to help the forecasters in their SW forecast. The goal of this thesis was to develop a useful automated tool to help the SW forecasters in their SW predictions. A severe weather intensity (SWI) index was created from the 1-km Global Environmental Multiscale Limited Area Model (GEM-LAM) outputs. The GEM-LAM 1-km was run on summer days in 2008 and 2009 over Alberta, Ontario, and Quebec. The dataset of summer 2009 was used to create algorithms that use the model's outputs to detect severe thunderstorm structural features, compute the quantity of the ingredients needed to initiate severe thunderstorms, and estimate the intensity and the type of SW expected. The post-processed fields were subjectively verified with the SW observations and radar images for the summer of 2009 leading to a decision tree for the SWI index for each region. An object-oriented method was used to verify the SWI index forecasts with the SW observations for the summer of 2008. The results showed that the SWI index forecast was very accurate over Ontario, accurate over Quebec, and much less accurate over Alberta. The lack of SW observations and the model's spin up mainly affected the results. Finally, the skill of the SWI index forecast was compared to the forecaster-derived SW forecast to verify if the index could help the SW forecasters to improve their SW forecast. The results indicate that the SWI index could improve the prediction of SW events, but not the positioning.

Résumé

Le temps violent (TV) estival peut avoir un impact important sur la vie des gens et leurs biens. En ce moment, aucun outil n'est assez performant pour aider les prévisionnistes à prévoir le TV. Cette thèse a pour but de créer un outil automatisé pour aider les prévisionnistes dans leurs prévisions de TV d'été. Un indice d'intensité de TV à été créé à partir des données du modèle global environnemental à multiéchelles à aire limitée (GEM-LAM) avec une résolution horizontale de 1 km. Le GEM-LAM 1-km à été roulé pour tous les jours d'été 2008 et 2009 sur les régions de l'Alberta, le sud de l'Ontario et le sud du Québec. Les données de l'été 2009 ont été utilisées pour créer des algorithmes qui utilisent les sorties du modèle pour détecter les structures particulières aux orages violents, évaluer les quantités de plusieurs éléments nécessaires à la formation d'orages violents, et estimer l'intensité et le type de TV attendu. Les champs post-traités ont été subjectivement analysé avec les observations de TV et les images radar pour l'été 2009 permettant de bâtir un arbre de décision pour l'indice d'intensité de TV pour chaque région. Une méthode par objet a été utilisée pour faire une vérification des prévisions de l'indice d'intensité de TV avec les observations de TV pour l'été 2008. Les résultats montrent que la prévision de l'indice d'intensité de TV est très juste pour l'Ontario, est assez juste pour le Québec, mais l'ai beaucoup moins pour l'Alberta. Le faible nombre d'observations de TV et le temps d'ajustement du modèle affectent les résultats. Finalement, la précision de l'indice d'intensité de TV et celle de la prévision de TV émit par un prévisionniste

ont été comparées de façon à vérifier si l'indice peut aider le prévisionniste à améliorer sa prévision. Les résultats démontrent que l'indice d'intensité de TV pourrait améliorer la prévision d'un évènement, mais pas son positionnement.

Acknowledgements

First, and foremost, I would like to thank my supervisor, Frederic Fabry, for his guidance, support, and flexibility throughout this master project. Despite the special circumstances, taking a leave of one year after the first year of my master's degree to become an operational forecaster at Environment Canada (EC) and then continuing my master's degree while working full time, Mr. Fabry always gave me the time and guidance that I needed to evolve and advance in my master project. Mr. Fabry is a wonderful person, easy to work with, and the best supervisor that someone can have.

In addition, my master project is the result of collaboration between McGill University and EC. Therefore, it is very important to mention the help and the opportunity that the High Impact Weather National Laboratory at EC has given me. This collaboration procured me an awe-inspiring master thesis project. I must thank, most particularly, Denis Jacob and Ronald Frenette, who were always available to answer technical questions or help me resolve some issues that I had throughout this project.

Finally, I must express all my gratitude to the heads of the Quebec Storm Prediction Centre and to the general director of the Quebec operational Meteorological Service of Canada to allow me to take as much vacation as I needed to finish my master thesis. I am also grateful to the department's administrative staff, Vaughn Tomassin, Ornella Cavaliere, and Paula Domingues,

for their precious assistance. Lastly, I must thank my proofreader, Amelie Wong, who did a wonderful work.

Table of contents

List of tables

List of figures

Chapter 1

Introduction

Severe weather (SW) such as heavy rain, tornados, strong winds, and large hail is a rare event, but it can have huge impact on our lives and any economic sector. For the average person, SW normally induces damages to their house, cars, and other material goods. On the other hand, industries are mainly affected in either work planning, to avoid any inconvenience, or in dealing with the consequences of the thunderstorms. The most important consequence of SW is the loss of human life. Since severe thunderstorms have repercussions on people and every economic sector, it is of high importance of having access to accurate severe thunderstorm forecasts.

1.1 Severe weather and its characterization

1.1.1 Convection review

At Environment Canada (EC), a meteorological event is classified as a severe thunderstorm if it produces 50 mm of rainfall (EC, 2013), tornados, hail larger than 2 cm in diameter, and wind speeds higher than or equal to 90 km/h (Verkaik and Verkaik, 2000).

One must be aware that only a few thunderstorms lead to SW, since specific elements are required to produce a severe thunderstorm. First, in order to get a thunderstorm, we need an unstable air parcel (Byers and Braham, 1949). The

stability of an air parcel is defined as its resistance to vertical motion. Trigger mechanisms such as lifting and destabilizing mechanisms such as heating of the surface and/or cooling aloft, or saturation, can cause an air mass to become less stable or even unstable (Byers and Braham, 1949). The next necessary ingredient is high moisture content in the air mass (Byers and Braham, 1949). High moisture content is needed in order to supply latent heat, as the water vapor condenses, to build and strengthen the storm. High moisture content is also needed to produce heavy precipitation. The last ingredient, which differentiates a thunderstorm from a severe thunderstorm, is the wind shear. One can correlate the longevity of a thunderstorm with the wind shear. For example, in an environment with weak wind shear, the updraft will not be tilted. In this scenario, the precipitation falls in the updraft and suppresses the updraft (Byers and Braham, 1949). This type of thunderstorm is called a single cell thunderstorm. These are short-lived and usually do not produce SW (Byers and Braham, 1949). However, if many single cell thunderstorms pass through the same path over a short period of time, flooding may occur. If this scenario occurs, the event will be considered a severe thunderstorm event.

A type of thunderstorm often associated with intense SW is the supercell thunderstorm (Browning, 1965). These storms require the same basic conditions to form as any thunderstorms. In contrast to single cell thunderstorms, supercell thunderstorms also require strong wind shear, as shown in the numerical simulations (eg., Weisman and Klemp, 1982, 1984, 1986; Weisman and Rotunno, 2000), which allows the supercell to live up to a few hours because the strong wind shear tilts the updraft. Consequently, the precipitation does not fall in the

updraft, which allows the thunderstorm to be self-sustaining. Supercellular thunderstorms have rotation in their updraft, which can be seen as a circular motion in the clouds, called a mesocyclone (Burgess and Brown, 1973). The mesocyclone is an important feature of the supercellular thunderstorms because low-level mesocyclone, once the rotation has extended all the way to the surface, is often associated to tornados (Trapp et al., 2005). In addition, supercell thunderstorms are prolific producers of tornados and large hail compared to other types of thunderstorms, but they also produce strong winds and flooding (Duda and Gallus, 2010).

The final kind of thunderstorm is the multicell thunderstorm. Multicell thunderstorms are many thunderstorm cells at different stages in their development (Chen, 1980). The same basic ingredients for a thunderstorm are needed, however, multicellular thunderstorms also need low to moderate wind shear (Marwitz, 1972). Consequently, the updraft is a bit tilted and the lifetime of the cell is longer than a single cell thunderstorm. The wind shear also helps to generate new cells along the gust front (Chen, 1980). In addition, multicell thunderstorms can evolve to become a supercell thunderstorm. Multicellular thunderstorms can produce SW such as strong winds, flooding, large hail, and short-lived tornados.

1.1.2 Overview of indices use to forecast severe weather

Some indices were created to help forecasters evaluate the state of the atmosphere. SW forecasters use many of them in their daily methodology in order to forecast SW. However, it is important to note that the forecaster cannot

evaluate whether or not there will be SW from the values of indices alone. These indices only give insight as to the area on which the forecaster should focus his/her attention.

The Lifted Index (LI) is used to evaluate the instability of the atmosphere by subtracting the environmental temperature at 500 hPa from the temperature of the air parcel lifted from the surface to 500 hPa (Galway, 1956). If LI is negative, the air is unstable; the forecaster then evaluates the possibility of having thunderstorms in this area by looking for any lifting mechanisms that could start convection. The Showalter Index (SI) also characterizes the instability of an air parcel (Showalter, 1953). SI is the difference between the temperature of an air parcel lifted from 850 hPa to 500 hPa and the environmental temperature at 500 hPa (Showalter, 1953). The smaller the index, the greater the instability. Both SI and LI are useful to evaluate the potential for thunderstorms. However, SI does not work in mountainous regions where the 850 hPa level is underground. Another index that evaluates the instability of the air is the George Index (K) (George, 1960). This index is different from both LI and SI as it also has another term to account for the moisture content and the vertical extent of the moist layer. K gives the thunderstorm potential, but does not give any information about the intensity of the storm (George, 1960).

An index that assesses more completely the convective instability, which is a necessary ingredient for thunderstorms to be initiated, is the Convective Available Potential Energy (CAPE). The CAPE evaluates the positive energy that a conditionally unstable air mass would have if lifted to the level of free convection (Moncrieff and Miller, 1976). Similarly, the Convective Inhibition

(CINH) is the energy needed to lift the air parcel to the level of free convection (Colby, 1984). Knowing the CAPE, the CINH, and the lifting mechanisms present, the forecaster is able to approximate the strength of the lifting mechanisms needed in order to reach the level of free convection. If there is a possibility that the level of free convection can be reached, the forecaster will assess the intensity of the possible storm.

There exist indices that evaluate the intensity of the storm. These indices take into account the shear, since, as mentioned previously, severe thunderstorms need wind shear to form. The Severe Weather Threat Index (SWEAT) considers the instability, the humidity, and the wind shear. By considering all these elements together, this index is able to differentiate ordinary and severe convection (Bidner, 1971). The Storm Relative Helicity (SRH) index is useful to identify where supercell thunderstorms might develop (Davies-Jones et al., 1990). If some regions are identified as having potential for supercellular thunderstorms to develop, the Energy Helicity Index (EHI) can be used to evaluate the potential for the occurrence and predict the intensity of tornados (Hart and Korotky, 1991). Finally, the last index presented in this research, the Storm Severity Index (SSI), also assesses the thunderstorm severity by using the wind shear and the CAPE (Turcotte and Vigneux, 1987).

1.1.3 Model available at EC to forecast severe weather

The Global Environmental Multiscales Limited Area Model (GEM-LAM) is an operational model from EC. The model is available at two different operational horizontal resolutions — 10-km and 2.5-km. The operational GEM-

LAM 10-km, also called REG-LAM, has 80 staggered Charney-Phillips vertical coordinates (Charney and Phillips, 1953) with the lid at 0.1 hPa (Vaillancourt et al., 2012). It has 996 x 1028 grid points (Vaillancourt et al., 2012) centered on North America. It is important to mention that at this resolution, the GEM-LAM is a hydrostatic model (Côté et al., 1998), since the hydrostatic assumption holds for atmospheric phenomena down to scales around 10 km. In other words, the GEM-LAM 10-km assumes that the atmosphere is hydrostatic by using the hydrostatic primitive equation (Côté et al., 1998). Therefore, it does not resolve convection. The GEM-LAM 10-km uses implicit physical parameterizations for sub-grid scale phenomenon such as convection (Côté et al., 1998). At this resolution, the GEM-LAM is better at forecasting synoptic scale phenomenon, such as fronts and low-pressure systems. On the other hand, the operational GEM-LAM 2.5-km is a non-hydrostatic model (Côté et al., 1998), and has 58 staggered Charney-Phillips vertical coordinates with the lid at 10 hPa (Giguère and Milbrandt, 2011). The GEM-LAM 2.5-km explicitly resolves convection (Rombough et al., 2010). The grid size of the GEM-LAM 2.5-km depends on the domain and this model is run on four domains: West, East, Arctic, and Atlantic (Fig. 1.1). A different SW index is used for each resolution. In that way, the additional information provided by the higher resolution model can be processed, since the model with higher resolution resolves processes that the lower resolution model could not. Thus, the SW indices must be interpreted differently as they were built to access processes at different scales.

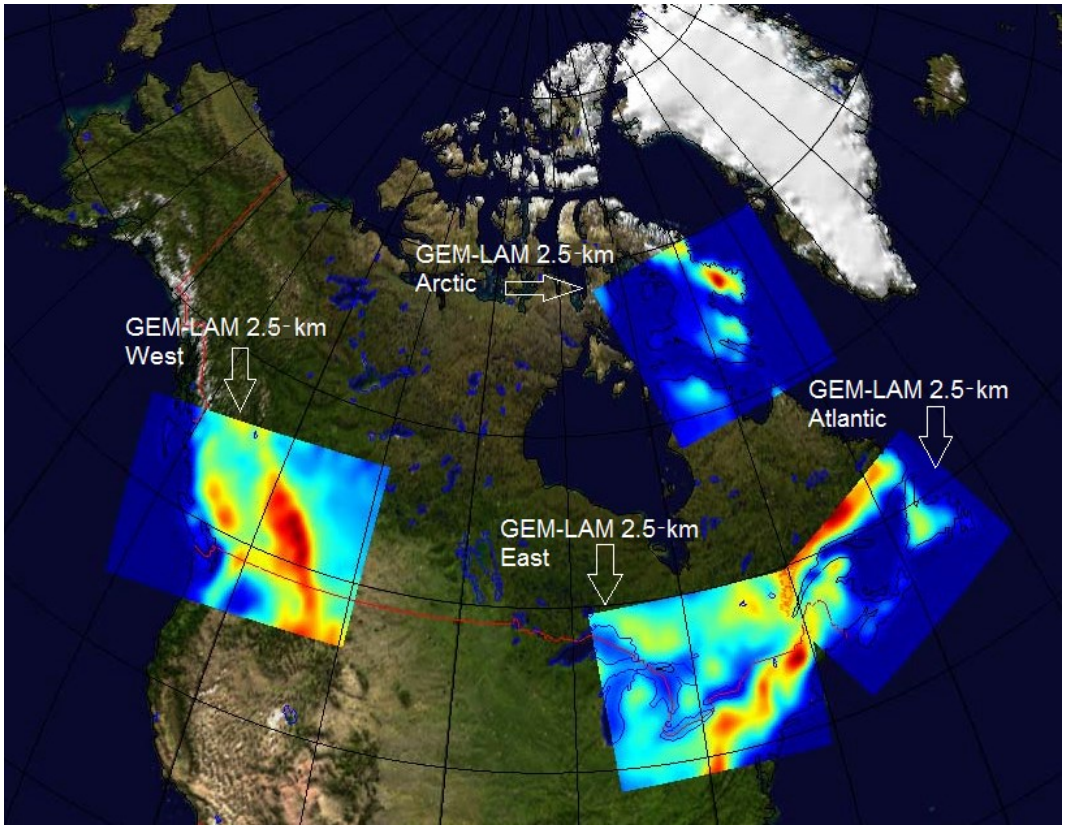

Fig. 1.1: The four operational domains of the GEM-LAM 2.5-km. Picture adapted from Rombough et al. (2010).

As mentioned earlier, the GEM-LAM at 2.5-km resolution uses explicit physical equations to resolve convection (Rombough et al., 2010). Thus, the GEM-LAM at 2.5-km should simulate the atmosphere more realistically than with a 10-km resolution. The GEM-LAM 2.5-km has been verified subjectively by Vaillancourt (2006b), a radar and SW specialist at EC, to evaluate the potential of this high-resolution model to forecast convection and SW. His findings show that the GEM-LAM 2.5-km is able to simulate convective features horizontally with an acceptable time difference from the radar (Vaillancourt, 2006b). One of the fields he examined to determine if the model well represented the reality was the relative vorticity. He noticed that the GEM-LAM 2.5-km is able to simulate

vorticity couplets (Vaillancourt, 2006b). Vorticity couplets are associated with supercell storms, which in turn often produce tornados. The correlation between the model forecasts and what was observed on the radar was accurate overall (Vaillancourt, 2006b).

Before this study, atmospheric scientists at EC were wondering if the model was able to simulate the vertical structure of a convective storm. To answer this question, Vaillancourt (2006b) compared a vertical view of the model with the radar. A vertical view of the vorticity field and the cloud liquid and solid water content was studied in a region of the model where convection was simulated. As one can see in Fig. 1.2, the model is able to simulate an overhang, a tilted region of echo overlaying a weaker region of echo on a small portion of its horizontal extent due to the environmental wind shear and a strong updraft, which is associated with the growth of a supercell. During his study, he also noted that, as the supercell intensifies, the rotation intensifies towards the ground. Therefore, the model simulates the vertical structure of the storm correctly. From the subjective verification done on the GEM-LAM 2.5-km, one can conclude that it can capture many processes observed in real storms.

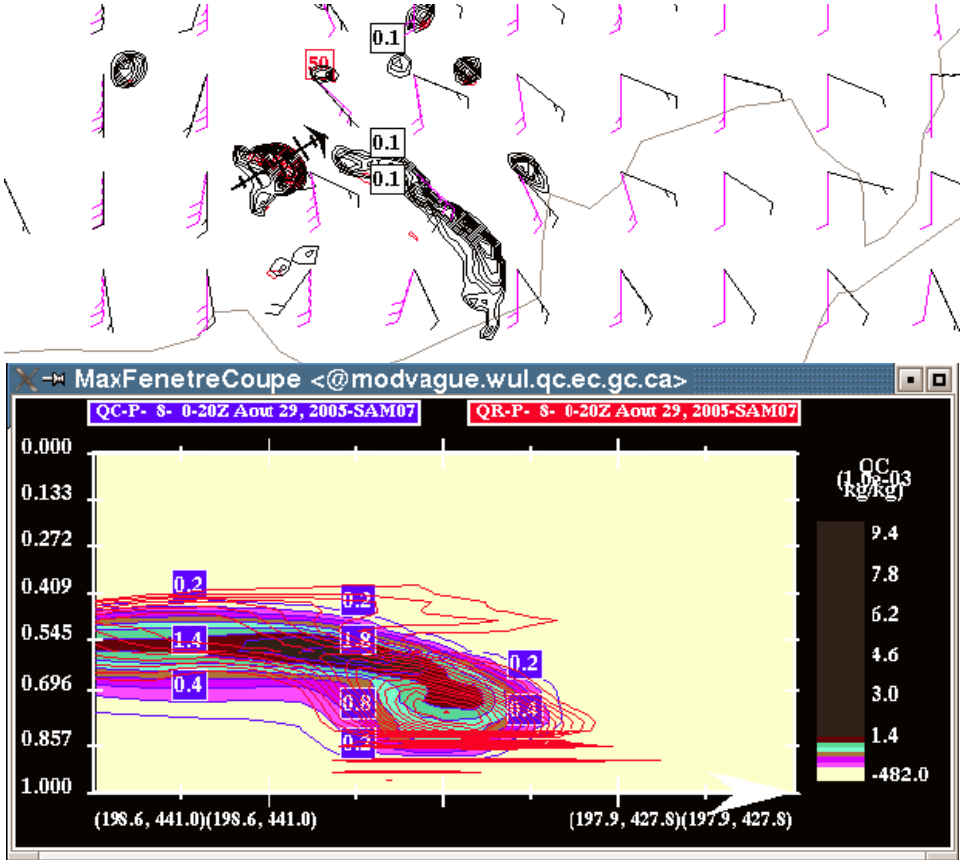

Fig. 1.2: Illustration of the ability of the model to simulate convection. In the top picture, the wind barbs from different levels, the cloud solid and liquid water content, and the relative vorticity from the GEM-LAM 2.5-km are illustrated. Black wind barbs are from the 925 hPa level, and the pink wind barbs are from the 800 hPa level. The black contours represent the cloud solid and liquid water content and the red contours represent the relative vorticity, both at the 0.810 sigma level. The approximate dimension of the image is 450 km by 150 km. The bottom picture is the vertical cross-section, indicated by the bold arrow in the top picture, of a severe thunderstorm simulated by the GEM-LAM 2.5-km. It contains the liquid and solid water content in the atmosphere (color) and relative vorticity (red) where the cross-section was made (Vaillancourt, 2006b). The vertical axis of this cross-section is in sigma level, terrain-following coordinate (Phillips, 1957).

1.1.4 Post-processed severe weather indices developed at EC

A SW probability algorithm was developed by the High Impact Weather National Laboratory at EC to detect radar-like SW feature signatures from the

outputs of the GEM-LAM 2.5-km (Roy et al., 2007). The algorithm was designed to detect SW radar features such as mesocyclones, overhangs, and bounded weak echo regions from model outputs (Vaillancourt, 2006b). These SW signatures are important when forecasting the occurrence of SW, since these features are mostly associated to the structure of supercell thunderstorms which are prolific producer of SW. However, it is even more important to forecast and evaluate the potential of SW events such as large hail, strong winds, and heavy rain to warn the public about what kind of SW is expected in order to better handle emergency. Therefore, the algorithm also detects regions that might contain large hail, evaluates the maximum wind gusts in the thunderstorm, and evaluates the potential for heavy rain (Vaillancourt, 2006b). All the variables computed in this algorithm are combined and weighted to produce a probability of having SW at any given point (Roy et al., 2007).

The High Impact Weather National Laboratory at EC has objectively verified all the preceding variables. However, it is important to note that the verification was made on an older model version. At that time, the model had 58 unstaggered vertical eta levels (Taylor and al., 2010) while the operational GEM-LAM 2.5-km now has 58 staggered Charney-Phillips vertical coordinates (Giguère and Milbrandt, 2011). The main difference between the eta and the staggered Charney-Phillips vertical level is that Charney-Phillips grid contains separated momentum and thermodynamic levels. In that way, dynamical constraints can be maintained. However, the most important change is the condensation scheme. At the time of this documented verification, the GEM-LAM 2.5-km had the Milbrandt-Yau single moment microphysics scheme (Taylor

et al., 2010), and now it uses the Milbrandt-Yau double moment microphysics scheme (Giguère and Milbrandt, 2011). No objective verification has been done with the new version, and no report was made from the subjective verification. From the results of the objective verification done on the old version of the GEM-LAM 2.5-km, it was concluded that the bounded weak echo region algorithm was useless, since bounded weak echo regions are smaller than the model's resolution, and consequently, the model cannot simulate them (Roy et al., 2007). The results from the verification also showed that the algorithms that compute the maximum wind gust in the thunderstorm, the hail and the potential for heavy rain were unable to detect successfully these types of SW. Moreover, the conclusion was that the SW probability depended mostly on the mesocyclone and overhang variable (Roy et al., 2007). Based on the results of this verification, the algorithms were modified in order to increase their accuracy and efficiency. Mesocyclone and overhang algorithms were modified in order to forecast fewer mesocyclone and overhang (Turcotte, 2007). Furthermore, the SW probability algorithm was modified to no longer take into account inefficient variables. It is now computed only with the mesocyclone and overhang variables, since the other SW algorithms and radar-like structure feature algorithms have no skill (Turcotte, 2007).

An algorithm was developed from the GEM-LAM 15-km outputs to identify thunderstorm regions and classify them into three categories: ordinary thunderstorm, potentially severe thunderstorm, and severe thunderstorm (Bachand, 2006). A subjective and objective verification was done to evaluate the algorithm (Frenette, 2006). The verification rapport that is available was made with the GEM-LAM 15-km. It is now applied to the GEM-LAM 10-km, but we

expect the same results since its resolution, as with the GEM-LAM 15-km, is too low to simulate convection. First, the program identifies if there is wind shear, instability, and available moisture since, as mentioned earlier, these are the three ingredients needed for severe thunderstorms. To verify if these elements are present, the program considers the wind speed, SWEAT, CAPE, EHI, SSI, and LI (Bachand, 2006). Vaillancourt (2006a) objectively and subjectively verified the outputs from the algorithm using lightning observations, satellite imagery, radar data, and reports from observers (Vaillancourt, 2006a). Frenette (2006) also objectively and subjectively verified the outputs from the algorithm with lightning observations for the month of August 2005. The results show that the regions flagged as thunderstorms are large (Frenette, 2006). The results also indicate that the area flagged as a potentially severe thunderstorm should be flagged as an ordinary thunderstorm instead, since a potentially severe thunderstorm area corresponds to an area where lightning was observed (Vaillancourt, 2006a). These are major problems for a forecaster, since the algorithm does not help to reduce his/her SW forecast region.

1.1.5 Methodology of the severe weather forecaster

As mentioned previously, in order to initiate convection, we need a moist, conditionally unstable airmass with a trigger mechanism that will lift the airmass to its level of free convection. In order to evaluate the potential for convection, the forecaster has to identify the presence of lifting mechanisms and mechanisms which destabilize the airmass.

The first thing that the forecaster needs to be aware of when arriving at the office is the current synoptic situation, along with the meteorological events that happened before his/her shift. In doing so, the forecaster is informed about the previous SW events that could generate other convective cells during his/her shift. It is also very important for the forecaster to look at the recent weather in regions adjacent to his/her forecast's regions as well, since SW coming from other provinces or countries may reach his/her forecast's regions.

Throughout his/her shift, the forecaster keeps an eye on the satellite imagery to follow the displacement and location of clouds. It is essential to follow the boundary between low-level clouds and observe the period of time that they stay over the same region. This is important because, if clouds shade a region, it will cause this region to warm up less than a cloud-free adjacent region. If this happens for a long enough period of time, differential heating will occur and might initiate convection due to convergence along the boundary (Weiss and Purdom, 1974).

Secondly, one of the most important tasks of the SW desk to forecast SW is to do a synchronous analysis. The goal of the synchronous analysis is to position all thermodynamic and dynamic triggers on a map in order to evaluate where the SW is most likely to be. The SW is most likely to occur where many trigger mechanisms and destabilizing mechanisms overlap and where the three ingredients to produce severe thunderstorms are present: convective instability, high moisture availability, and wind shear. The forecaster will do the synchronous analysis at a few different times to cover the period of convection of the forecasted region with the most recent model outputs, and will re-evaluate his

analysis as new model outputs are available. The position of low-pressure systems should be indicated first on the analysis. Then, the fronts are drawn. Fronts are important to locate, since they can initiate convection (Sanders and Paine, 1975) by inducing rising motion due to convergence at the surface and aloft. Also, the passage of a cold front destabilizes an air mass, which might lead to convection. On the other hand, the warm air advection, associated with a warm front, stabilizes an air mass, but it also produces rising motion along its boundary. Therefore, in a region of strong conditionally unstable air, the lift along a warm front might be sufficient to trigger convection (Maddox and Doswell, 1982). Next, the forecaster locates the 500 hPa short wave trough, analyzes its position, and draws it on the analysis since it can initiate severe thunderstorms (Galway, 1958). By looking at the 500 hPa trough, the forecaster indicates the region where he/she believes there will be rising motion ahead of the trough caused by positive vorticity advection and divergence (Kloth and Davies-Jones, 1980). However, in a pattern of weak vorticity, vertical motion will be mainly forced by warm air advection (Maddox and Doswell, 1982). Now, at the 250 hPa level, the forecaster looks at where the jets are positioned to locate regions of divergence. The right entrance and the left exit regions of the high level jet are usually divergent regions where there is vertical motion. It has been shown that the rising motion is strong enough and extends far enough down into the atmosphere to initiate convection or at least be part of the initiation process (Bluestein and Thomas, 1984). In a stable atmosphere, the rising motion induced by the divergent regions of a jet decreases the stability below the non-divergent level (Uccellini and Johnson, 1979), cools the air to saturation and releases the convective instability (Bluestein and Thomas,

1984), and brings moisture into the low levels (Bluestein and Thomas, 1984). However, the main role of the upper-level jet is to advect cool dry air in the upper and middle levels, increase upper-level divergence, and lead to the advection of sensible heat downstream from the convective area (Uccellini and Johnson, 1979). Thus, the forecaster draws the areas that correspond to the left exit and right entrance regions of the upper level jet on the synchronous analysis. Then, he/she looks for the presence of a low-level jet and its position. The main role of the low-level jet is to transport heat and moisture within the low levels (Uccellini and Johnson, 1979). One can easily picture that, when a low-level jet is combined with an upper-level jet, it produces a region of convective instability, since the warm moist air advection in the low-level coupled with dry cool air advection aloft destabilizes the airmass. Therefore, the forecaster also indicates the low-level jets on his/her analysis and analyses their position according to the upper-level jet. Generally, the synoptic lifting does not trigger convection, but it produces an environment favorable for convection by destabilizing the airmass (McNulty, 1995). Generally, not enough time is available to significantly destabilize the airmass with the synoptic lift mechanisms (Doswell, 1987), therefore mesoscale lift mechanisms supply the extra lift needed to reach the level of free convection and trigger convection. Differential heating is one of many mesoscale lift mechanisms, so the forecaster indicates regions where solar heating works with the topography and creates convergence, such as sea breeze (Chandik and Lyons, 1971), circulation driven by urban areas (Changnon, 1977), and the boundary between clear sky and cloudy sky (Weiss and Purdom, 1974). Convergence can also be induced by the interaction of wind and terrain, and trigger convection

(Chu and Lin, 2000). As mentioned earlier, one of the most important ingredients for deep moist convection is moisture availability. Thus, it is very important to verify if there is enough moisture available or if it will become available by advection on the region, by looking at the moisture advection, the moist tongue (Miller, 1972), an extension of an airmass with high relative humidity into an airmass of lower relative humidity, and the moisture convergence flux (Hudson, 1971). When the forecaster has finished positioning the thermodynamic and dynamic triggers, he/she will look in detail at the indices. The main ones are SSI, CAPE, LI, SWEAT, and SRH. Once the forecaster has looked at everything possible in the amount of time that he/she had, he/she draws a thunderstorm region according to where the most important features on his/her synchronous analysis are located and where they overlap.

In order to determine if thunderstorms will be severe or not, the forecaster needs to do a tephigram analysis to see if enough shear is present in the atmosphere, and evaluate the depth of the convection. First, the forecaster needs to select tephigrams that are representative of the airmass that is currently affecting, or will affect, his/her region of forecast. From his/her previous analysis he/she modifies the surface temperature and dew point for the one currently forecasted. From this, the forecaster evaluates if the solar heating, moisture advection, and/or air advection will be enough to trigger convection. The forecaster can adjust the surface dew point and temperature until the tephigram profile is favorable for convection. In doing so, it gives the forecaster an idea of the surface temperature and dew point needed to have convection. While the forecaster is adjusting the surface temperature and dew point, he/she is also

looking at indices and other fields computed directly from the profile, such as LI, CAPE, precipitable water, vertical wind shear, SRH, and EHI. As mentioned previously, by analyzing the CAPE and the CINH, the forecaster evaluates the depth of the possible convection (Moncrieff and Miller, 1976) and the energy needed to achieve convection (Colby, 1984). Moreover, the forecaster verifies subjectively if lift mechanisms are strong enough to initiate convection. Up to this point, the forecaster has a good idea if deep moist convection can occur. The only ingredient left to verify is the wind shear. So, the forecaster looks at the hodograph to see if there is wind shear present in the lower troposphere and whether it is unidirectional or curved. This is to access the potential of single cell thunderstorms, multicellular thunderstorms, and supercellular thunderstorms (Klemp and Wilhelmson, 1978; Weisman and Klemp, 1982). However, there are a few more things that are useful with the tephigram — the low-level jet and its intensity can be located, and the freezing level can be found to access the potential for hail (Pappas, 1962). Also, the precipitable water value computed from the profile indicates the potential for heavy rain from thunderstorms (Mogil and Groper, 1976).

At this point, the forecaster, with everything he/she has analyzed, has to emit a severe thunderstorm map, which indicates the area where thunderstorms are possible, where thunderstorms are expected, and where severe thunderstorms are predicted (Fig. 1.3). It is quite obvious that the SW forecast is a long process. The analysis is difficult and complex, as there are so many factors to take into consideration over a huge region. Therefore, there is a constant need to develop useful and precise SW forecast tools to help the forecaster focus his/her process

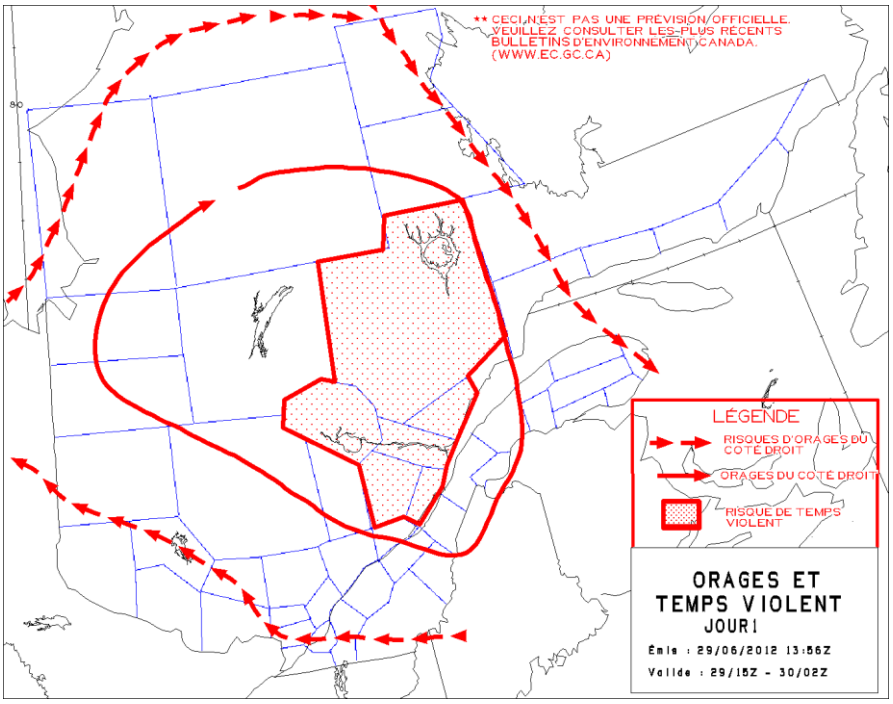

Fig. 1.3: Forecaster-derived day-1 SW forecast. In this case, the region surrounded by the dashed arrows indicates where there is a risk of thunderstorms. The region surrounded by the solid arrow shows where thunderstorms are expected. Inside the dotted box, severe thunderstorms are expected.

over a smaller area. The previous section describes how the present available SW forecast tools are inadequate for the SW forecaster.

1.1.6 Severe weather development

From the previous section, the SW forecaster has a lot of data to analyze. Forced by the forecast deadline and the other duties of his function, the forecaster might lack the time to do a thorough analysis of the situation. This is the reason why SW algorithms have been created, to facilitate forecaster's work by merging information together and saving some of his/her time to finish other important duties.

At this moment, many algorithms exist to diagnose SW and evaluate its potential from radar data. One of the first radar-based SW potential algorithms involved detecting convective cells and associating them with a SW index. This index was based on the vertically integrated liquid (VIL) and the horizontal size of the storm (Kitzmiller et al., 1995). However, the developers of the algorithm knew that it could be greatly improved by increasing the number of predictors and by using Doppler radar (Kitzmiller et al., 1995). The operational Doppler radars were installed throughout the United States (US) in the mid 90's (Evans and Weber, 2000). At the time, the major use of Doppler radars was to detect microbursts to avoid aviation accidents. The first microburst detection algorithm came out with the first experimental Doppler radars, and it kept improving over the years (Evans and Weber, 2000). In addition, Doppler radar can detect mesocylones, as first noticed by Donaldson et al. (1969). Since the 90's mesocyclone detection algorithms have been invented and continue to improve (Desrochers and Donaldson, 1992). Obviously, since it was already possible to detect two SW features, it was evident that the algorithms had to be expanded to accomplish a storm cell ranking based on detected SW features. The Warning Decision Support System (WDSS) and the Canadian Radar Decision System (CARDS), to name only two of them, are algorithms that detect many SW features (Joe et al., 2004). The CARDS can assess the presence of mesocyclones, downbursts, and gust potential, as well as evaluate hail size and the tornado potential based on radar data (Joe et al., 2004). On the other hand, the WDSS takes many different forms of data as input: radar data, lightning data, surface data, and other weather data (Joe et al., 2004). The main difference between

WDSS and CARDS is that WDSS, after processing the presence and the intensity of mesocyclone, hail, and tornado, will output each detected cell and its rank indicating the storm's severity (Joe et al., 2004). These tools are of great help to the forecaster. They alert the forecaster that some cells are potentially dangerous. Consequently, to verify the accuracy of the tool and to assess the associated threat the forecaster will start analyzing specific storm cells by doing a further meticulous analysis of the cells' structure, features, and VIL.

However, the index from SW detection radar algorithms provides only a short lead time, in the order of a few tens of minutes. Thus, the SW radar algorithms are useful in the nowcast of severe thunderstorms. High-resolution model outputs are more useful to generate thunderstorm forecasts, since most model outputs are available at each hour and for a period of at least 12 hours. It has been shown by Kain et al. (2006) that when forecasters had access to a high-resolution model, there was a small but significant improvement in the human forecasts. This suggests that high-resolution models have unique information that is very advantageous to forecasters. However, the model used had a 4-km resolution and was not able to detect convective scale features accurately (Kain et al., 2006). Thus, a cloud convective resolving scale model would give a forecaster a great advantage in forecasting SW.

The resolution of a cloud scale resolution model is close to radar resolution, which is 1 km. Therefore, radar algorithms that were designed to detect the presence of SW were seen as a good way to forecast SW if they were modified and applied to the outputs of a high-resolution model. This has been done at EC with the GEM-LAM 2.5-km outputs, and the results were the ones mentioned

previously. One can wonder if better results could have been obtained with a higher-resolution model. Simulations done with the GEM-LAM 1-km showed that the convection simulated at this resolution was more realistic than at 2.5-km (Taylor et al., 2010). Also, one can wonder if SW radar criteria applied directly to a model of such resolution allow us to better forecast SW than by other methods.

1.2 Objectives

There is a huge need to improve the ability to forecast SW at EC. In response to the pressing need to improve forecasting ability and to better understand the physical processes that lead to the development of thunderstorms, the Understanding Severe Thunderstorms and Alberta Boundary Layers Experiment (UNSTABLE) project collected data in 2008 and 2009. One of their goals was to examine how well a high-resolution model can forecast severe convection (Taylor et al., 2008). During the summers of 2008 and 2009, the UNSTABLE project ran the experimental GEM-LAM 1-km over the Alberta Foothills. The details of the GEM-LAM 1-km are based on the experimental 2010 Vancouver Olympics (VO2010) High-Resolution Modelling System (HRMS) with 1-km resolution (High Resolution GEM-LAM Visualization Platform, 2009). Simulations showed that the GEM-LAM 1-km simulates a more realistic convective mode than the 2.5-km (Taylor et al., 2010). This research will use the same model as the UNSTABLE project, the GEM-LAM 1-km.

In this thesis, I will investigate the best way to use the GEM-LAM 1-km outputs to produce a severe weather intensity (SWI) index. The most frequently

used indices by the forecaster to forecast severe thunderstorms will be computed. Algorithms to search for storm structures and features will be designed. The model will be run over three windows: Alberta, Southern Ontario, and Southern Quebec. The objectives of this thesis are the following:

- To find the best variables to forecast SW using the observations and the model outputs from the summer of 2009.
- To create a SWI index based on the best predictors.
- To analyze the skill of our SWI index by comparing it to observations from the summer of 2008.
- To see if the following severe storm features are well-simulated by the model: bounded weak echo region, overhang, mesocyclone.

Chapter 2 will address the observations analyzed in this research and the way they were manipulated. The details of the model used in this research will also be discussed in Chapter 2. Chapter 3 will cover the algorithms developed to detect SW, radar-like severe thunderstorm feature elements, and necessary ingredients to develop severe convection from the GEM-LAM 1-km outputs. It will also include a brief overview of all the indices computed and other variables coming directly from the model outputs. The method used to choose the best predictors and to build our SWI index will be discussed in Chapter 4. The objective method chosen to verify our index will also be explained in Chapter 4. The accuracy of our index will be computed and analyzed in Chapter 5. Chapter 6 consists of a discussion. Chapter 7 contains a conclusion.

Chapter 2

Data

2.1 Observations

The Canadian SW observations used in this thesis were taken from the Storm Event Data Capture System (SEDCS), which is a web interface database at EC. Reports of thunderstorms having produced tornados, funnel clouds, mesocyclones, flash floods, severe winds, and hail are archived in the SEDCS web interface database. In the SEDCS database, the majority of the events are narratively described. A description of the damage caused by the thunderstorms, a comparison to a common object to describe hail size, and/or an adjective to describe the intensity of rain, are usually found in the SEDCS database. Moreover, only for a few events, the database procures measured values for the wind speed, rain amount, or hail size. Thus, for most of the events, one has to deduce such quantities from the narrative description of the event. It also includes observation of tornados, funnel clouds, and mesocyclones.

To describe hail size, coins are often used as well as common objects. Table 2.1 shows the different coins used to describe hail size and their diameter. Table 2.2 demonstrates the different common objects used to describe hail size, and also indicates their diameter. For the purpose of this research, I have rounded up hail size according to the measured value or estimated value to the nearest multiple of 5, so that the hail size in the database of this research ranges from 0 to 110 mm

with an increment of 5. In my database, I do not differentiate hail diameter that was measured from the one estimated based on the size of common objects.

Only few severe thunderstorm reports have measured wind speed, the others usually have a description of the damage caused by the wind. The Beaufort scale is used to estimate the wind speed according to the damage caused by the thunderstorm. In our database, the measured wind speed was distinguished from the estimated wind speed. The measured wind speeds have positive values, and the estimated wind speeds were assigned negative values.

Coins	**Diameter (mm)**
Dime	18.03
Penny	19.05
Nickel	21.2
Quarter	23.88
Dollar coin (Loonie)	26.5
50 Cent/Half Dollar coin	27.13
Two Dollar coin (Toonie)	28

Table 2.1: Size of Canadian coins used to describe hail size.

Object	Diameter (mm)
Pea	6.4
Marble	13
Walnut/Ping-pong ball	38
Golf ball	44
Lime/Chicken's egg	51
Tennis ball	64
Baseball	70
Apple/Teacup	76
Grapefruit	102
Softball	114

Table 2.2: Table of common objects' size used to describe hail size.

Moreover, observation reports for tornados, funnel clouds, and mesocyclones were also extracted from the SEDCS database for this research. However, I separate observations of funnel clouds from tornados. That way, I can easily do my verification with or without either observation. Near the Rocky mountain foothill, cold core tornados and non-supercell funnel clouds are important phenomena (McDonald, 2000). So, during the verification, we might want to avoid considering funnel cloud and/or tornado reports for Alberta so as not to be biased by the cold core events. Mesocyclone reports are important to keep, since

mesocyclones are generally associated with supercell thunderstorms (Burgess and Brown, 1973) that often produce SW.

It was more difficult to extract severe rain events when the intensity of the rainfall was subjectively described and no measure was available. In that case, archived radar images, if available, were useful to evaluate severe rain potential. First of all, I should mention that the severe convective rain criteria changed in 2010. As mentioned previously, the actual severe convective rainfall criterion is 50 mm in one hour. However, prior to the summer of 2010, the severe convective rainfall criterion was 25 mm in one hour. The severe synoptic rainfall criterion has always been 50 mm in less than 24 hours. In this study, we used data from the summers of 2008 and 2009. Thus, I am using 25 mm in one hour as a severe rainfall criterion. First, I made two categories — one was when 25 mm of rain fell in one hour and the second was when 50 mm of rain fell in less than 24 hours. It was easy to categorize severe rain events with measured quantities of rain and duration. However, with a subjectively and qualitatively described event, I had to look at the severity of the terms used and the duration of the event to evaluate the possibility of a severe rain event. For example, if an event was described as strong rain with a 15-minute duration, I made an evaluation that there was no potential of severe rain. However, if an event was described as a heavy downpour with a 15-minute duration, I evaluated that there was severe rain potential. Also, flooding reports of house's basement were categorized as severe rain events. In my database, I distinguish the two categories mentioned previously, as well as the measured events from the narratively described events.

SW observations from the US are also used in this research (http://www.spc.noaa.gov/wcm/#data). SW data, such as hail, tornados, and wind, were extracted from the Storm Prediction Center (SPC) as compiled in Storm Data. Hail size was converted to millimeters, and the wind speed was converted to kilometers per hour.

SW reports were extracted from the SEDCS and the SPC Storm Data for the summers of 2008 and 2009. Canadian SW reports were extracted for these periods over the province of Alberta, Ontario, and Quebec. The US's SW reports were extracted for these periods over the states of Washington, Idaho, Montana, Michigan, Indiana, Ohio, Pennsylvania, New York, Vermont, New Hampshire, and Maine.

2.2 Model

For this research, the experimental GEM-LAM with a resolution of 1 km is used, the same model version as the one used during the Vancouver Olympics of 2010. It is a one-way nested model (Rombough et al., 2010). Since no mesoscale data assimilation is available for high-resolution models at EC, a cascade of integrations is made. Figure 2.1 clearly illustrates this procedure. However, the following description of the cascade of integration is valid for the years 2008 and 2009, for which the model will be used. Presently, it follows the same procedure, but using the GEM-LAM 10-km instead of the GEM-LAM 15-km. First, the GEM-LAM 15-km run is initialized from the 6-hour forecast of the Regional GEM 15-km run, which started at 0000 UTC (Mailhot et al., 2010). The

boundary conditions for the GEM-LAM 15-km are also provided by the regional run (Mailhot et al., 2010), and it is integrated for 30 hours. Then, the GEM-LAM 2.5-km run is initialized at 1200 UTC from the 6-hour forecast of the GEM-LAM 15-km run, which started at 0600 UTC (Rombough et al., 2010). The GEM-LAM 2.5-km is initialized six hours after the GEM-LAM 15-km to allow time for the model to spin-up (Mailhot et al., 2010). The GEM-LAM 15-km also provides the boundary conditions for the GEM-LAM 2.5-km (Mailhot et al., 2010). The GEM-LAM 2.5-km is integrated for 24 hours (Rombough et al., 2010). Finally, the GEM-LAM 1-km run is initialized at 1500 UTC from the 3- hour forecast of the 2.5-km run. It also provides the boundary conditions for the GEM-LAM 1-km that is integrated for 12 hours. Thus, the GEM-LAM 1-km is available from 1500 UTC to 0300 UTC the following day. The GEM-LAM 1-km is a non-hydrostatic

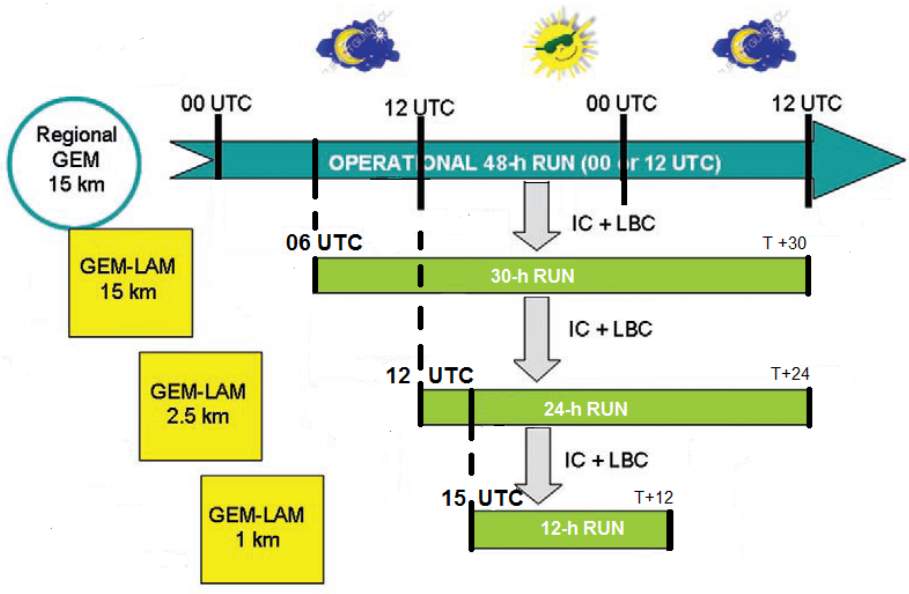

Fig. 2.1: The daytime configuration of the high-resolution modeling. IC is the abbreviation for initial condition. LBC is the abbreviation for lateral boundary condition.

model with 58 staggered Charney-Phillips vertical coordinates (Taylor and al., 2010). It was run over three domains: Alberta, Southern Ontario, and Southern Quebec (Fig. 2.2). The position of each 1-km domain was chosen according to the position of the GEM-LAM 2.5-km (Fig. 2.2) and the SW observations for the summer of 2009 (Fig. 2.3). The Alberta domain has 450 x 520 grid points, the Southern Ontario domain has 700 x 600, and the Southern Quebec domain has 600 x 600 grid points. The GEM-LAM 1-km uses the double moment version of the Milbrandt-Yau microphysics scheme (Milbrandt and Yau, 2005) which improves precipitation quantities, rates and identification of the type of precipitation compared to its single moment version (Mailhot et al., 2010). It also has new diagnostic output, such as the wind gust based on the method developed by Brasseur (2001).

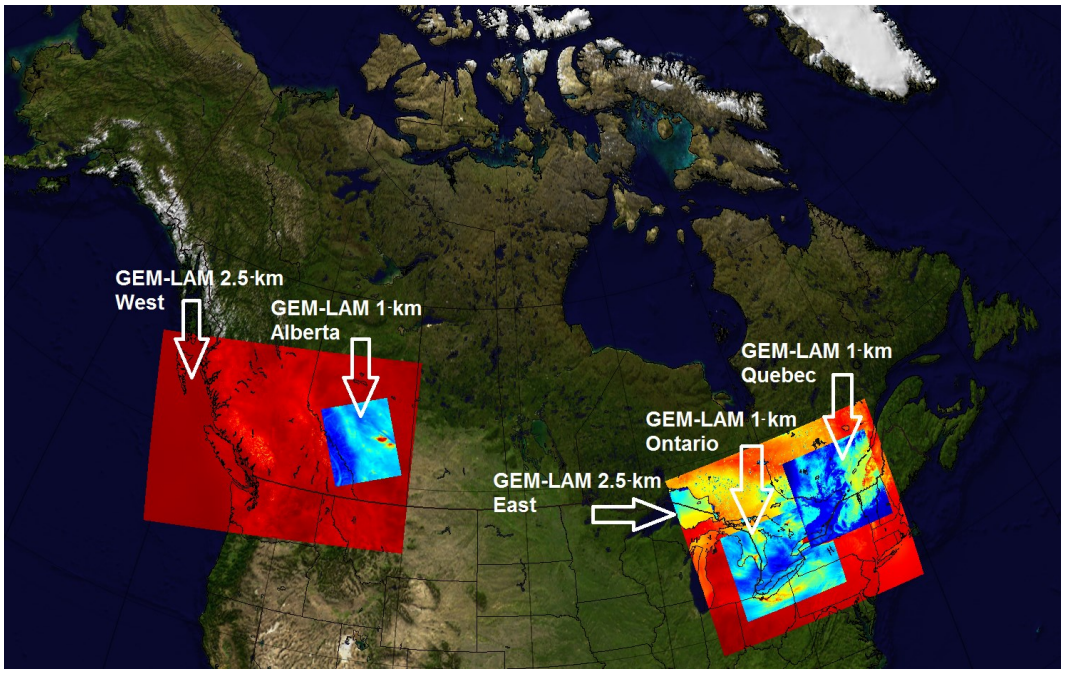

Fig. 2.2: Domains of the GEM-LAM 2.5-km (larger, mainly reddish domains) and the experimental GEM-LAM 1-km (smaller, mainly bluish domains).

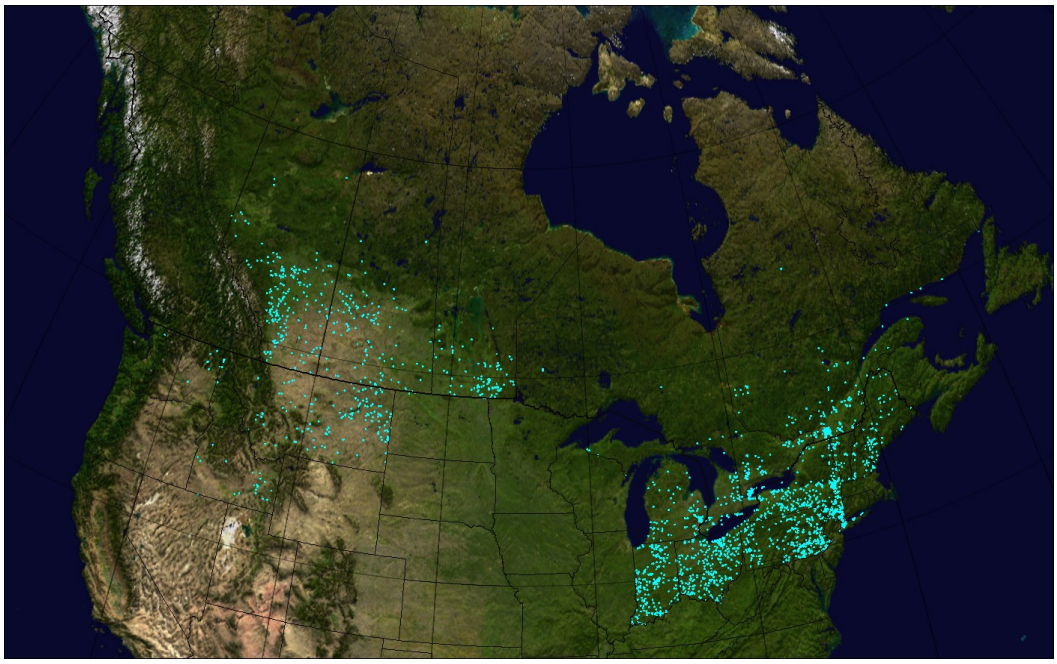

Fig. 2.3: SW observations for the summer of 2009 over the Prairies, Ontario, Quebec, and the states of Michigan, Indiana, Ohio, Pennsylvania, New York, Vermont, New Hampshire, Maine, Washington, Idaho, and Montana.

Chapter 3

Post-processed fields

Once a model run is completed and the outputs are generated, they can be used to detect whether the model has simulated the presence of SW. Many SW warning systems or indices have been automated and produced from algorithms that process model outputs to evaluate the potential and/or severity of thunderstorms. Therefore, for the purpose of this research, algorithms were

developed to assess the presence of severe thunderstorms from the GEM-LAM 1-km model outputs.

3.1 Detection of radar-like severe weather signatures

Severe thunderstorms have particular feature elements compared to ordinary thunderstorms. Therefore, I believe that, if the GEM-LAM 1-km simulates convection well and realistically, the best way to use the model outputs is to use them to search for the 3D structure of radar-like feature of severe thunderstorm. In this research, we limit ourselves to five radar-like severe convection features: mesocyclone, overhang, bounded weak echo region, severe updraft, and vorticity couplet. Moreover, algorithms based on the 3D structure should be more resilient to the model version's change, and therefore more operationally useful. In addition, algorithms based on the 3D structure do not exist at the High Impact Weather National Laboratory at EC. Currently, their algorithms use fixed reflectivity criteria at different height ranges and do not use the 3D structure of the model outputs to look for specific structures (Turcotte, 2007; Vaillancourt, 2006).

Let us first consider the overhang algorithm, since the bounded weak echo region algorithm and the mesocyclone algorithm use its output. An overhang is an important severe thunderstorm feature. Long-lived thunderstorms are the result of strong environmental wind shear and a strong updraft that cause the precipitation to be tilted so that it does not fall into the updraft. An overhang is the radar signature of such tilted precipitation. It is associated with multicellular and

supercellular thunderstorm. The overhang algorithm uses the following model outputs — the equivalent reflectivity, the maximum equivalent reflectivity in the vertical above freezing level, and the geopotential height. The geopotential height and the equivalent reflectivity are 3D fields, and the maximum equivalent reflectivity above freezing level is a 2D field. The overhang algorithm loops through the horizontal points and checks if the maximum equivalent reflectivity above freezing level is greater than 45 dBZ. If a point has a maximum equivalent reflectivity above freezing level greater than 45 dBZ, the algorithm does a 3D scan to find all the points connected to it that have an equivalent reflectivity greater than 30 dBZ (Fig. 3.1). If the difference between the top height and the base height of these points is greater than 5 km, then the algorithm checks if there is a weak echo region to identify these points as an overhang. If the algorithm identifies a weak echo region below 3 km above ground level (AGL), an equivalent reflectivity of less than or equal to 10 dBZ within the horizontal and vertical extent of the interconnected points (Fig. 3.1), then the algorithm flags these points as an overhang. The overhang field is a 2D field, so only the horizontal extent of the interconnected points found earlier is kept. A value of 1 indicates an overhang, and a value of 0 indicates no overhang.

The bounded weak echo algorithm is part of the overhang algorithm. If the necessary conditions are present to form a thunderstorm with a tilted updraft and that the updraft strongly intensifies, on the radar a vault will be noticed in the overhang. This vault is commonly named a bounded weak echo region and indicates that a thunderstorm has a severe updraft. It is important to mention that the overhang and the bounded weak echo region are not mutually exclusive. A

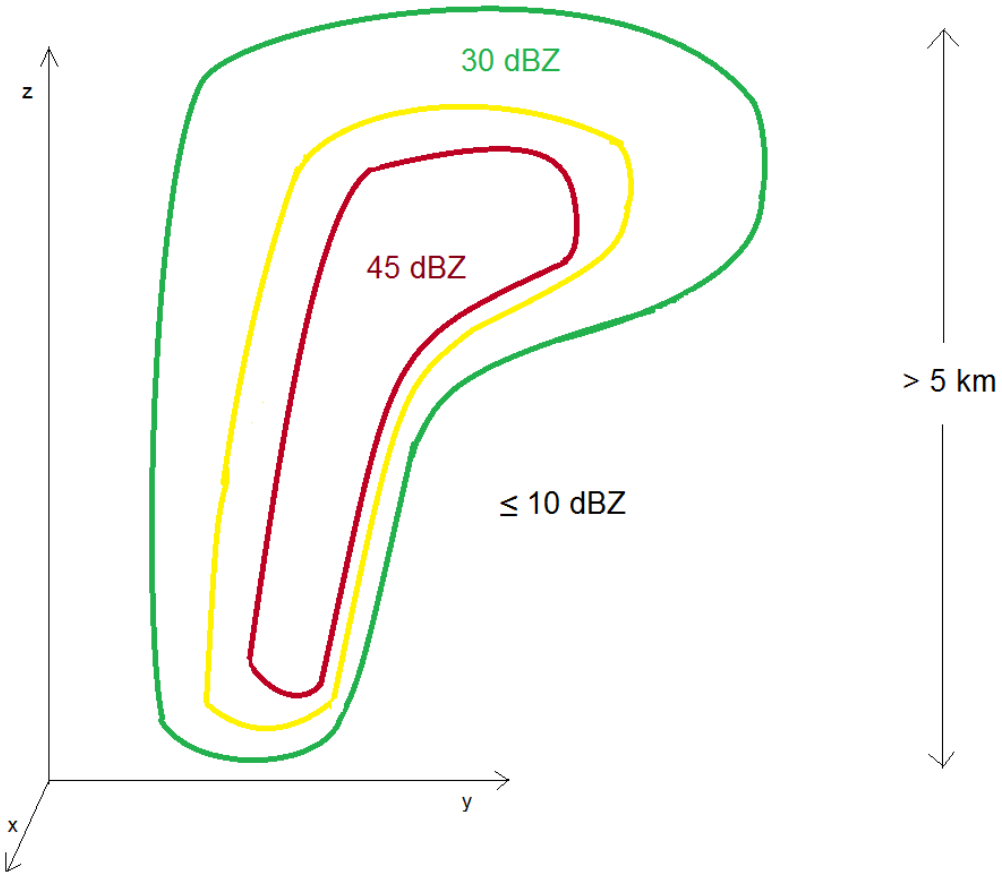

Fig. 3.1: Description of the overhang algorithm. First, it finds a point with a maximum vertical reflectivity above the freezing level greater than 45 dBZ. Then, it finds all the points interconnected to this one that have a reflectivity greater than 30 dBZ. To check if these points correspond to an overhang region, their vertical extent needs to be greater than 5 km. Finally, these points are identified as an overhang region if there is weak echo region — a region with reflectivity less than or equal to 10 dBZ below 3 km AGL and within the horizontal and vertical extent of the interconnected points.

bounded weak echo region is a special case of the overhang. Bounded weak echo region is mostly associated to supercellular thunderstorm and to large hail event. Therefore, once the overhang algorithm has found an overhang, it will look for a bounded weak echo region: the algorithm will look for the highest vertical point below the overhang with 0 dBZ reflectivity, given a maximum equivalent reflectivity above freezing level of at least 40 dBZ. If there is such a point, the

algorithm finds the highest point above this horizontal grid point and below the overhang where the equivalent reflectivity is less than or equal to 10 dBZ. At this vertical level, the algorithm checks within 5 surrounding horizontal grid points if the equivalent reflectivity is greater than 30 dBZ. If there is a point with this criterion, it also verifies that this point does not belong to the points found with the overhang algorithm (Fig. 3.2). If the algorithm has found all these requirements, the highest point vertically below the overhang with 0 dBZ reflectivity and a maximum equivalent reflectivity above freezing level of at least 40 dBZ is flagged as a bounded weak echo region. The bounded weak echo field is a 2D field, which corresponds to the flagged grid points associated to bounded weak echo regions. A value of 1 corresponds to a bounded weak echo region, and a value of 0 corresponds to no bounded weak echo region.

Next, mesocyclone, defined as a rotating updraft, is particular to supercellular thunderstorms which are prolific producer of SW. Also, tornados can be associated to mesocyclone if its rotation extends all the way to the surface. The strong environmental wind shear needed to produce supercell induces vortex tubes. The interaction between the updraft and the environmental vortex tubes produces a vortex couplet that straddles the updraft (Davies-Jones, 2002). As the storm propagates, the updraft becomes nearly positioned with one of the vortices, so the updraft acquires rotation which is identified as a mesocyclone (Davies-Jones, 2002). A rotating updraft at middle altitude corresponds to the first stage of a mesocyclone's evolution (Burgess et al., 1982). The mesocyclone algorithm uses the geopotential height, the relative vorticity, and the maximum equivalent reflectivity above freezing level. The geopotential height and the relative vorticity

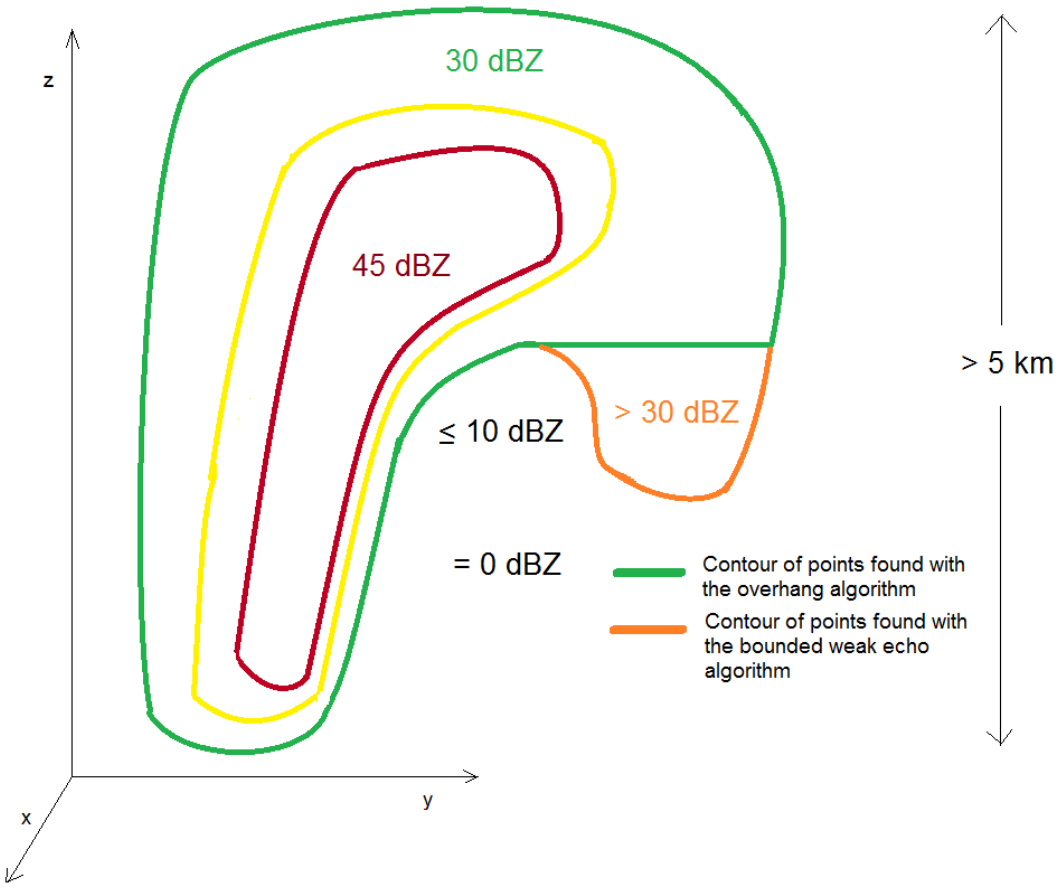

Fig. 3.2: Description of the bounded weak echo algorithm. It is a continuity of the overhang algorithm. Once an overhang region is found, the algorithm finds the highest point with 0 dBZ reflectivity below the overhang, given a maximum vertical reflectivity above the freezing level of at least 40 dBZ. Then, from this point, the highest point below the overhang with a reflectivity less than or equal to 10 dBZ is found. At this vertical level, the algorithm verifies if within surrounding 5 horizontal grid points there are points with a reflectivity greater than 30 dBZ that do not belong to the overhang region. Given that such points exist, the highest point with 0 dBZ reflectivity and a maximum vertical reflectivity above the freezing level greater than or equal to 40 dBZ is identified as a bounded weak echo region.

are 3D fields, but the maximum equivalent reflectivity above freezing level is a 2D field. In addition, the mesocyclone algorithm uses the overhang output from the overhang algorithm, which is a 2D field. The algorithm loops through all the points in the horizontal plane, and checks at each point if the maximum equivalent

reflectivity above freezing level is greater than 40 dBZ, also if an overhang was detected by the overhang algorithm. If this is the case, the algorithm does a 3D scan to find all the connected points between 2 km and 12 km AGL that have a relative vorticity greater than 0.004 s^{-1}. As shown by Cai (2005), the mesocyclone's vorticity is dependent on the grid's resolution of the dual Doppler analysis. In Cai's research, the mesocyclones' vertical vorticity were approximately 0.02 s^{-1} for 1-km grid spacing, 0.005 s^{-1} for 3-km grid spacing and 0.003 s^{-1} for 5-km grid spacing (Cai, 2005). Even if the model used in this thesis has a 1-km resolution, it cannot forecast atmospheric phenomena of scales smaller than 3 km, since at least three grid points are needed for a wave representation, and five to seven grid points are needed to well represent a wave and its discontinuities (Haltiner and Williams, 1980). Thus, based on the literature and the phenomenon's scale that the model can resolve, I took the mean of the 3-km and 5-km grid mesocyclone vorticity values from Cai (2005), which is approximately 0.004 s^{-1}, to identify a mesocyclone's vertical vorticity. We are aware that this value will have to be recalculated and changed whenever the resolution of the model changes. However, this happens less frequently than model version change. Once all the interconnected points have been found by the algorithm, the base and the top of these points have been kept in memory, so that the height of this strong vorticity region can be computed. If the height is greater than 2 km, the interconnected points found are flagged as a mesocyclone. The mesocyclone field is a 2D field: thus, only the horizontal extent of the interconnected points flagged as mesocyclone is kept in the mesocyclone field. A value of 1 indicates a mesocyclone, and a value of 0 indicates no mesocyclone.

The severe updraft algorithm uses the vertical velocity and the geopotential height from the model's outputs, which are both 3D fields. The algorithm loops horizontally and vertically to find points with a vertical velocity smaller than -50 Pa/s below 12 km AGL. If the algorithm finds one point reaching this criterion, it does a 3D scan to find all interconnected points with a vertical velocity smaller than -20 Pa/s below 12 km AGL. The values to locate severe updraft were estimated from Auer and Sand (1966). Updraft measurements were taken from the base of cumulonimbus clouds, and the average values for the updraft ranged from approximately 2 m/s (≈ -20 Pa/s) to 6 m/s (≈ -70 Pa/s), depending on rain intensity (Auer and Sand, 1966). Of course along the region of convergence, the updraft will be more severe, and over a short period of time, the updraft might be more intense than these average values (Auer and Sand, 1966). The average values are sufficient for the purpose of this algorithm, since severe peaks in an updraft are mostly at a smaller scale that the GEM-LAM 1-km can resolve, and last for shorter time periods than the interval between model outputs. The interconnected points must have a vertical extent of at least three vertical levels to be flagged as a severe updraft by the algorithm. The severe updraft is a 2D field that corresponds to the horizontal extent of the interconnected points found. A value of 1 corresponds to a severe updraft, and a value of 0 corresponds to a non-severe updraft.

As mentioned in the mesocyclone algorithm section, the vorticity couplet is associated to supercellular thunderstorm as it is prior the first stage of a mesocyclone's formation. Therefore, vorticity couplets are important to detect the potential of a storm's rotation. The vorticity couplet algorithm uses the relative

vorticity and the geopotential height from the model's outputs. First, the algorithm searches for positive vortices. It loops through all the grid points between 1 km and 8 km AGL and verifies if there are points with a relative vorticity value greater than 0.004 s^{-1}. If it finds such a point, the algorithm does a 3D scan to find all the interconnected points with a relative vorticity value greater than 0.002 s^{-1}. If this set of points extends over at least three vertical levels, it is considered to be a positive vortex. Next, the algorithm searches for negative vortices by looping through all the grid points between 1 km and 8 km AGL and verifying if there are points with a relative vorticity value of less than -0.003 s^{-1}. If it finds such a point, the algorithm does a 3D scan to find all the interconnected points with a relative vorticity value of less than -0.002 s^{-1}. If this set of points extends over at least three vertical levels, it is considered to be a negative vortex. The vorticity values from Cai (2005) were used to estimate the vorticity threshold to identify the vorticity couplet for the same reasons explained in the mesocyclone algorithm section and are in accordance with value used for the mesocyclone algorithm. The discrepancy of the relative vorticity value between the negative and positive vortex is due to the subjective analysis of the model outputs and its ability to realistically simulate severe thunderstorm structure. It was noticed that the negative vortex of a vorticity couplet is usually weaker than the positive vortex, which agrees with literatures because clockwise curved wind shear, commonly observed in the Northern Hemisphere, favor the positive vortex (Davies-Jones, 2002). Finally, the algorithm compares the position, as well as the horizontal and vertical extent of the positive and negative vortices, to identify vorticity couplets. In order to be considered a vorticity couplet, the positive and the negative vortices

must have common horizontal grid points and share common vertical levels (Fig. 3.3). The vorticity couplet is a 2D field, which contains the horizontal extent of the positive and negative vortices that were considered to be vorticity couplets. The value 1 indicates that a vorticity couplet was found, and the value 0 means that there was no vorticity couplet found.

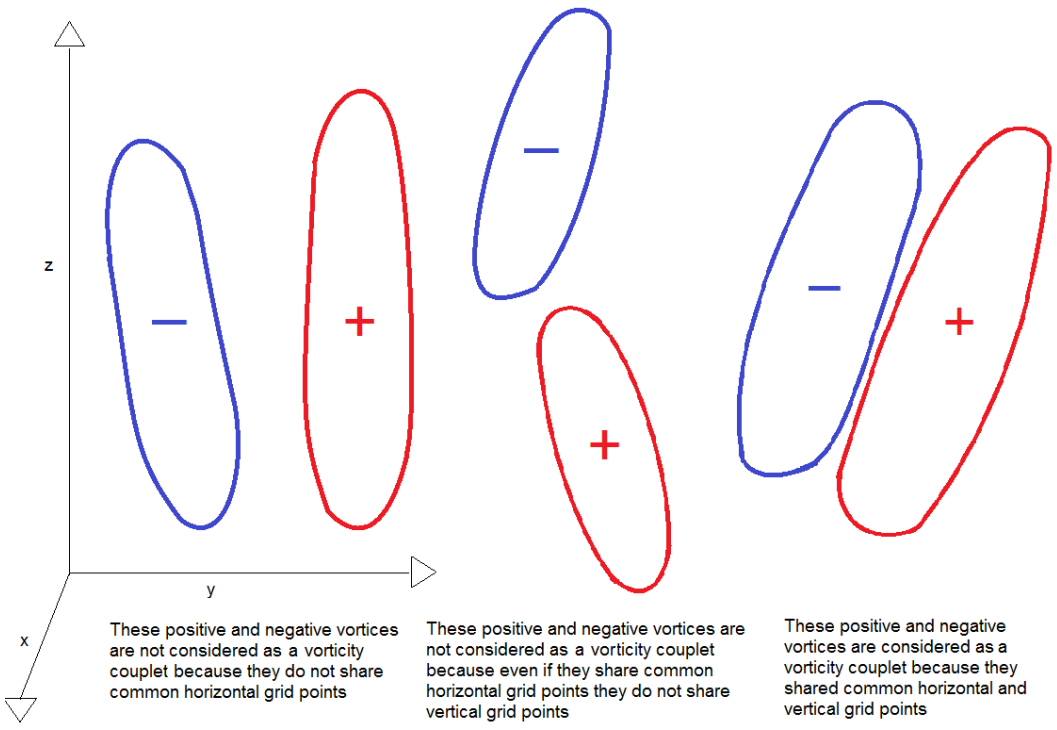

Fig. 3.3: Description of the vorticity couplet algorithm. First, the algorithm identifies the positive vortices by finding points with a relative vorticity greater than 0.004 s^{-1} and all interconnected points with a relative vorticity value greater than 0.002 s^{-1}. Then, it finds the negative vortices by finding points with a relative vorticity smaller than -0.003 s^{-1} and all interconnected points with a relative vorticity value smaller than -0.002 s^{-1}. Finally, it identifies vorticity couplets by locating positive and negative vortices that share common horizontal and vertical grid points.

3.2 Indices

The most frequently used indices operationally to forecast SW are computed in order to identify the best approach to use a high-resolution model to forecast SW. The STRATUS library available at EC was used to compute the indices needed and other fields from vertical profiles of atmospheric fields. The STRATUS library is part of a visualization tool used at the Quebec Storm Prediction Centre (QSPC) to visualize atmospheric soundings. The STRATUS library can be used on any vertical set of points. In order to use the STRATUS library, a vertical profile of pressure, temperature, dew point temperature, height, wind speed, wind direction, x-component of the wind, and y-component of the wind was provided at every horizontal grid point. In order to compute the CAPE and the CINH, a tephigram analysis was made for each horizontal grid point. That way, I could compare the CAPE calculated from the tephigram analysis done with the STRATUS library to the CAPE directly calculated by the model. The CAPE is sensitive to the details of the calculation (Doswell and Rasmussen, 1994). Therefore, there could be differences between the two computation methods, since the STRATUS library uses the most complete equation for each index, while, the model often uses approximation to save computer time, as is the case with LI as shown by Frenette (2006). The stratus library was also used to compute LI (Galway, 1956), SI (Showalter, 1953), K (George, 1960), TT (Miller, 1972), SWEAT (Bidner, 1971), SRH (Davies-Jones et al., 1990), EHI (Hart and Korotky, 1991), and SSI (Turcotte and Vigneux, 1987) in agreement with the corresponding literature. However, some indices, such as TT, K, and SWEAT are

computed only when the surface pressure is greater than or equal to 850 hPa. Thus, in the Alberta window, a major part of our window will not have these indices due to the Rockies being present.

3.3 Additional ingredients for severe thunderstorms

In this section, algorithms that compute additional ingredients required to make convection severe will be presented. As mentioned previously, the necessary ingredients are instability, moisture, and wind shear. In the previous section, many stability indices among the indices were computed for this research. Therefore, up to this point, algorithms to quantify the condensed water content and the wind shear are needed.

Moisture availability is of great importance for severe convection. Thus, I have two algorithms that compute the convergence of humidity. The first one calculates the convergence of humidity at 700 hPa at each grid point. The second one finds the convergence of humidity at its maximum in each column, and keeps the value and height. They both use the specific humidity and the divergence fields from the model's outputs. The first algorithm also uses the pressure field, and the second one also uses the geopotential height.

Next, we also need an algorithm that computes wind shear in the atmosphere, which is the only ingredient to differentiate severe convection from ordinary convection. There is an algorithm that calculates wind shear between 0-3 km and 0-6 km. The algorithm adds the magnitude of the wind shear vector between two consecutive levels from the surface to 3 km, and from the surface to

6 km. From these calculations, the total directional wind shear and speed shear is obtained. In other words, the algorithm considers the change in wind direction with height and the change of wind speed with height, which a simple addition of wind shear vectors does not. This algorithm uses the geopotential height, the wind speed, and the wind direction from the model's outputs.

3.4 Type of severe weather expected

In this section, algorithms that can be used to identify the type of SW expected — hail, heavy rain, strong winds, and tornados — and its severity will be introduced.

First, the algorithms that can be used to forecast hail and evaluate its size will be presented. There is an algorithm that computes the supercooled liquid water in every column. The value of the integrated supercooled liquid water is operationally useful to evaluate the potential for hail. The model's double moment microphysics scheme computes the cloud's supercooled liquid water, which can also be useful to evaluate the potential for hail. The other interesting algorithm to evaluate the potential for hail computes the vertical ice flux. It uses the vertical velocity, the mixing ratio of ice crystals, the hail mixing ratio, and the graupel mixing ratio, which are all 3D fields from the model's outputs. The algorithm calculates a sum of the vertical ice flux in each column above the -15°C level. Also, with the double moment microphysics scheme, the hail's diameter is available as a 3D model's output. Thus, there is an algorithm that finds the maximum hail size in each column based on the hail's diameter field.

Next, the algorithms that evaluate the microburst potential and the gust intensity are presented. The approach by Brasseur (2001) that provides an estimation of the range of the wind gust at the surface caused by the deflection of winds by turbulent mixing was recently added to the model's outputs. I wanted to evaluate its efficiency and compare it to other wind intensity algorithms. The gusts based on Brasseur's method consist of the estimated wind gust and the maximum wind gust. There is an algorithm that checks if Brasseur's method has forecasted near-severe gusts (larger than 70 km/h). If it has, it keeps the values for the estimated and maximum gust. I wanted to compare Brasseur's method to a wind index called the WINDEX. The WINDEX is a wind index from which the wet microburst potential can be estimated. The WINDEX is an approximation of the wind intensity in knots. There is also an algorithm that computes the WINDEX. For more information about this wind index, please consult McCann (1994). Also, since dry microburst is very important for the Prairies, there is an algorithm that verifies the operational criteria for dry microburst. Necessary atmospheric conditions for dry microburst are dry low-level with moisture present in the mid-level of the atmosphere (Wakimoto, 1985). Thus, the algorithm verifies if the dew point spread is greater than or equal to 8°C for every level below 3 km AGL, and if the dew point spread is smaller than or equal to 5°C for every level between 4 km and 7 km AGL. If these two conditions are met, the grid point will be flagged. A value of 1 corresponds to dry microburst, and a value of 0 corresponds to no microburst. However, for Ontario and Quebec, wet microburst is important. Thus, an algorithm to compute the operational criteria for wet microburst is needed. The operational way to evaluate the wet microburst

potential is to compare the potential temperature between the low-level and the mid-level of the atmosphere (Atkins and Wakimoto, 1991). Our algorithm calculates the difference between the potential temperature at 700 hPa and 500 hPa at each grid point. Values greater than 20 are considered to be at great risk of wet microburst (Atkins and Wakimoto, 1991).

Let us consider the algorithms evaluating the potential and the intensity of heavy rain. There are two model outputs that I use to evaluate the heavy rain potential and severity — the liquid water content in the column, and the liquid water content of 700 hPa and above at each grid point. There is also an algorithm that verifies if the accumulated rain forecasted by the double moment microphysics scheme is greater than or equal to 25 mm for the past hour, or if it is greater than or equal to 50 mm. In addition, the vertical moisture flux field can also be used to evaluate flash flood potential. Thus, the vertical moisture flux algorithm computes the total vertical moisture flux in each column. It uses the specific humidity and the vertical velocity from the model's outputs.

Finally, there is one algorithm to identify tornados. It passes through the relative vorticity field below 2 km AGL and checks if, on at least three consecutive levels, the relative vorticity has a value greater than or equal to 0.0037 s^{-1} in agreement with the mesocyclone algorithm and the vorticity measurements from Cai (2005). If these conditions are reached, the grid point will be flagged. A value of 1 implies that a tornado was detected, and a value of 0 means that no tornado was detected.

Chapter 4

Evaluation methodology

The methodology chapter is long and quite complex. Figure 4.1 is a flow chart that describes the important steps of this research. It is a useful chart to help the reader to navigate through the complex processes and their technical details. Therefore, people who are not familiar with the explained processes might have to refer to this figure often while reading the Chapter 4.

4.1 Execution of the model

The GEM-LAM 1-km was executed each day of the summers (June, July, and August) of 2008 and 2009 over the three regions shown previously in Chapter 2: Southern Quebec, Southern Ontario, and Alberta. As mentioned in Chapter 2, each run is initialized at 15 UTC and is integrated for a period of 12 hours. The model outputs are available for every hour from 15 UTC to 03 UTC the following day of the initialization. A list of the model outputs can be viewed in Table 4.1. When the runs for the summer of 2009 were completed, a subjective analysis was performed on the model outputs for a few SW days to evaluate which severe thunderstorm features are resolved by the model (described in Section 4.2). Afterwards, I started developing the algorithms presented in Chapter 3 to detect the severe thunderstorm features resolved by the model that were observed during the analysis of the model outputs for those few SW cases. In order to verify that

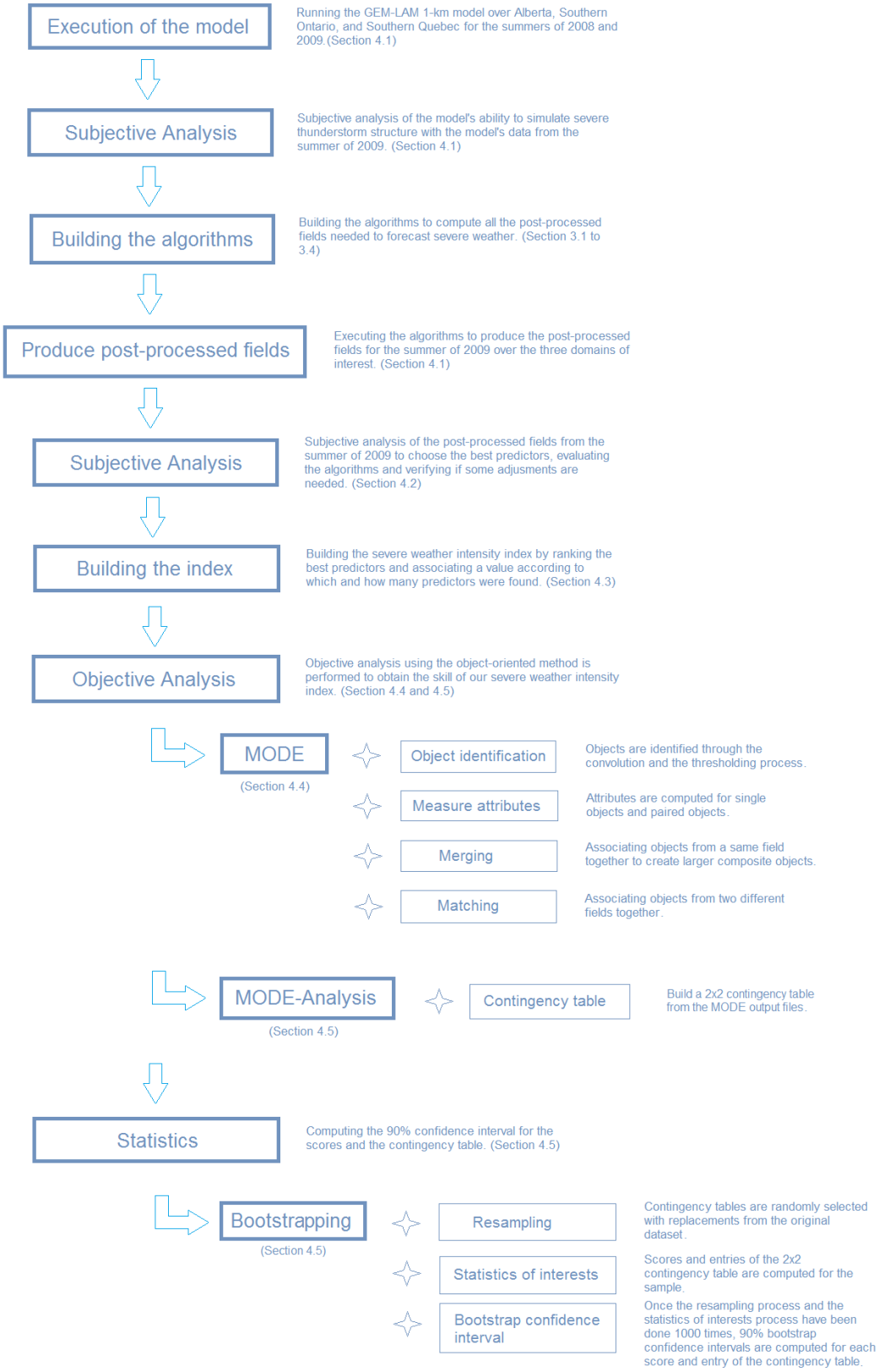

Fig. 4.1: Key processing steps of this research.

Name	Description	Unit	Dimension
MX	Filtered geopotential topography	m^2/s^2	2D
ME	Mountain	m	2D
PN	Sea level pressure	hPa	2D
TT	Air temperature	°C	3D
TD	Dew point temperature	°C	3D
HU	Specific humidity	kg/kg	3D
UU	X-component of the wind	kt	3D
VV	Y-component of the wind	kt	3D
UV	Wind modulus	kt	3D
WW	Vertical motion	Pa/s	3D
WD	Meteorological wind direction	degree	3D
GZ	Geopotential height	Dam	3D
PX	Pressure	hPa	3D
QR	Relative vorticity	s^{-1}	3D
DD	Divergence	s^{-1}	3D
QBT1	Cloud droplets mixing ratio	kg/kg	3D
QLT1	Rain drops mixing ratio	kg/kg	3D
QIT1	Mixing ratio of ice	kg/kg	3D
QNT1	Mixing ratio of snow	kg/kg	3D
QJT1	Graupel particles mixing ratio	kg/kg	3D
QHT1	Mixing ratio of hail	kg/kg	3D
NCT1	Number concentration of cloud droplets	m^{-3}	3D
NRT1	Number concentration of rain drops	m^{-3}	3D
NIT1	Number concentration of ice crystals	m^{-3}	3D
NNT1	Number concentration of snow crystals	m^{-3}	3D
NGT1	Number concentration of graupel particles	m^{-3}	3D
NHT1	Number concentration of hail particles	m^{-3}	3D
P0	Surface pressure	hPa	2D
LA	Geographical latitude	degree	2D
LO	Geographical longitude	degree	2D
IH	Water vapor vertical integration	kg/m^2	2D
IY	Integral of upper troposphere (700hPa) water vapor	m	2D
WGE	Wind gust estimate from turbulent kinetic energy	m/s	2D
WGX	Wind gust maximum from turbulent kinetic energy	m/s	2D
U4	CAPE from the convection scheme	J/kg	2D
K6	Maximum vertical velocity in convective cloud	m/s	2D
BE	Buoyant energy	J/kg	2D
IB	Integrated supercooled liquid water	kg/m^2	2D
SLW	Total supercooled liquid water content	kg/m^3	3D
PR	Quantity of precipitation	m	2D
SN	Snow	m	2D
A2	Accumulation of stratiform liquid precipitation	m	2D
A4	Accumulation of stratiform solid precipitation	m	2D
PZ	Shallow convection precipitation rate	m/s	2D
RRN1	Precipitation rate-liquid drizzle	m/s	2D
RRN2	Precipitation rate-liquid rain	m/s	2D
RFR1	Precipitation rate-freezing drizzle	m/s	2D
RFR2	Precipitation rate-freezing rain	m/s	2D
RSN1	Precipitation rate-ice crystals	m/s	2D
RSN2	Precipitation rate-snow	m/s	2D
RSN3	Precipitation rate-graupel	m/s	2D
RPE1	Precipitation rate-ice pellets	m/s	2D

RMX	Precipitation rate-mixed precipitation	m/s	2D
RN1	Accumulated liquid drizzle	m	2D
RN2	Accumulated liquid rain	m	2D
FR1	Accumulated freezing drizzle	m	2D
FR2	Accumulated freezing rain	m	2D
SN1	Accumulated ice crystals	m	2D
SN2	Accumulated snow	m	2D
SN3	Accumulated graupel	m	2D
PE1	Accumulated ice pellets	m	2D
PE2	Accumulated hail	m	2D
PE2L	Accumulated large hail	m	2D
AMX	Accumulated mixed precipitation	m	2D
EI	Outgoing infrared energy exiting the atmosphere	W/m^2	2D
FV	Upward surface latent heat flux	W/m^2	2D
FC	Upward surface sensible heat flux	W/m^2	2D
FQ	Momentum flux at surface	Pa	2D
FI	Surface incoming infrared flux	W/m^2	2D
EV	Outgoing visible energy exiting the atmosphere	W/m^2	2D
H	Height of boundary layer	m	2D
DMR	Mean mass diameter of rain	m	3D
DMG	Mean mass diameter of graupel	m	3D
DMH	Mean mass diameter of hail	m	3D
ZET	Total equivalent reflectivity	dBZ	3D
RT	Total precipitation rate	m/s	2D
P2	Stratiform liquid precipitation rate	m/s	2D
P4	Stratiform solid precipitation rate	m/s	2D
RPE2	Precipitation rate-hail	m/s	2D
RPEL	Precipitation rate-large hail	m/s	2D
ZEC	Maximum equivalent reflectivity in a vertical column	dBZ	2D

Table 4.1: List of the fields available from the GEM-LAM 1-km.

the algorithms were well designed and that there were no coding problems, the algorithms were run for those same SW days to see if the algorithms detected every feature that I detected visually. When the algorithms were working well, I executed my program over the three regions for the summer of 2009. The program involves using my algorithms and taking the model's outputs as inputs to produce post-processed fields.

4.2 Subjective analysis

A subjective analysis was done on the post-processed fields of the summer of 2009 for the Alberta, Southern, Ontario and Southern Quebec regions in order to choose the best predictors among the post-processed fields to build our SWI index. A subjective analysis was also necessary to evaluate our algorithms and verify if some adjustments were needed before using them for the summer of 2008's dataset. Usually, subjective analysis is not the most robust analysis since it procures no statistics, and an objective analysis is preferred by researchers. In our case, a subjective analysis was the most robust method to choose the best predictors and to evaluate our algorithms due to the high-resolution of our grids, the scarcity of SW observations, and the limited radar products available for past events. It was impossible to get archived radar data for the summer of 2009 over the three regions to compare it with the model and the post-processed fields, because it required a lot of resources that the Cloud Physics and Severe Weather Research Section of the Meteorological Research Division at EC did not have. Only the CAPPI radar images were archived and easily accessible on the EC website. Therefore, the construction of a decision tree with a statistical tool from the SW observations and the post-processed fields was not the most efficient method in this case, due to the limitations of a point-by-point comparison on high-resolution grids with rare events (Brown et al., 2002). A point-by-point comparison does not allow any tolerance in time and space (Brown et al., 2002), which is a major problem because even if a model simulates a severe thunderstorm well, it will rarely be at the exact same place and time that it was

observed, if observed at all. Even doing an upscaling of the observations and the post-processed fields would not have worked because the thresholds found for continuous fields by the decision tree statistic tool after the upscaling would have been biased. Therefore, the only way that I could compare the post-processed fields to the SW observations and the CAPPI radar images, in order to get a more complete analysis, was to do a subjective analysis. In addition, a subjective analysis allows some tolerance in space and time.

There were 45 post-processed fields to analyze and compare with the SW observations and the CAPPI radar images. The list of the post-processed fields can be seen in Table 4.2. Each day of the summer of 2009 was analyzed thoroughly over the three regions. It is important to specify that notes were taken about the value of each post-processed field and whether or not SW was observed or possible from the radar images.

Once the subjective analysis was done, some adjustments were made to a few algorithms according to the results of the analysis. However, the main changes were due to some coding errors in the algorithms. For example, before the adjustments, no vorticity couplets were detected, since there was a problem in the vorticity couplet algorithm where it associates a positive vortex with a negative vortex to identify them as a vorticity couplet.

Name	Description	Unit
SI	Showalter index	°C
SSI	Severe storm index	—
LI	Lifted index	°C
ITT	Total Totals index	°C
K	George index	°C
SRH	Storm relative helicity	m^2/s^2
EHI	Energy helicity index	—
SWEA	Severe weather threat index	—
CAPT	CAPE calculated from the tephigram analysis	J/kg
CINT	CINH calculated from the tephigram analysis	J/kg
MXRT	Maximum equivalent reflectivity above freezing level	dBZ
ZEC	Maximum equivalent reflectivity in a vertical column	dBZ
OH	Overhang occurrence	—
SU	Severe updraft occurrence	—
CH	Maximum convergence of humidity	g/kg·s
HCH	Height of the maximum convergence of humidity	m
VMF	Vertical moisture flux	Pa·g/kg·s
MESO	Mesocyclone occurrence	—
MESB	Height of the base of the mesocyclone	m
WER	Bounded weak echo region occurrence	—
WDX	Wind index (WINDEX)	kt
TOR	Tornado occurrence	—
HL	Hail occurrence in a vertical column	—
CV	Vorticity couplet occurrence	—
HLS	Hail size at the surface	mm
HLX	Maximum hail size in a vertical column	mm
SHR3	0-3 km wind shear	kt
SHR6	0-6 km wind shear	kt
ACC	Accumulated rain in the past hour	mm
ACCT	Total accumulated rain	mm
SVR	Severe rain occurrence	—
CH7	Convergence of humidity at 700 hPa	g/kg·s
PV	Positive vortex occurrence	—
NV	Negative vortex occurrence	—
TETA	Potential temperature difference between 700 hPa and 500 hPa	K
2DB	Downburst occurrence	—
VIF	Vertical ice flux	Pa·g/kg·s
SLW	Integrated supercooled liquid water	g/m^3
WGE	Wind gust estimate	km/h
WGX	Wind gust maximum	km/h
CAPM	CAPE from the convection scheme	J/kg
K6	Maximum vertical velocity in convective cloud	m/s
CSLW	Cloud supercooled liquid water	g/m^2
LWC	Integrated liquid water content	g/m^2
LWC7	Integrated liquid water content from 700 hPa	g/m^2

Table 4.2: List of the post-processed fields.

4.3 Building the index

To build our SWI index, the best predictors to forecast severe thunderstorms needed to be chosen from the post-processed fields. The purpose of the subjective analysis was to permit the ranking of the best predictors of severe thunderstorms. With the notes of the analysis, the best predictors and their associated thresholds, for non-binary predictors, were chosen. The 12 best common predictors can be seen in Table 4.3. As expected, the post-processed fields associated with the thunderstorm's structure were the best predictors for the three regions. Even if the best predictors are the same for the three regions, the thresholds for the continuous predictors are slightly different, since each region has, on average, a type of SW that is more frequent than the others. Moreover, it is important to mention that our index does not identify the SW expected, but predicts the occurrence of SW and evaluates its intensity based on the thunderstorm's structure and the basic ingredients for severe thunderstorms.

Names	Description	Unit
OH	Overhang occurrence	—
SU	Severe updraft occurrence	—
MESO	Mesocyclone occurrence	—
WER	Bounded weak echo region occurrence	—
MXRT	Maximum equivalent reflectivity above freezing level	dBZ
VMF	Vertical moisture flux	Pa·g/kg·s
LWC	Integrated liquid water content	g/m^2
LWC7	Integrated liquid water content from 700 hPa	g/m^2
SHR3	0-3 km wind shear	kt
SHR6	0-6 km wind shear	kt
SWEA	Severe weather threat index	—
VIF	Vertical ice flux	Pa·g/kg·s

Table 4.3: List of the best severe thunderstorm predictors.

Using these best predictors, a SWI index with values ranging from 0 to 100 was designed, 0 being a very low SWI and 100 being a high SWI. The SWI index is a cumulative index. In other words, each grid point is given an SWI index for the entire forecast period, which in our case, is from 15 UTC to 03 UTC. First, the SWI index algorithm goes through all the predictors listed in Table 4.3 every hour from 15 UTC to 03 UTC to find points where the maximum equivalent reflectivity is greater than 40 dBZ, and where there is also at least one of the following: overhang, severe updraft, mesocyclone. Then, the algorithm finds all the interconnected points that also have an overhang, a severe updraft, or a mesocyclone. Finally, the SWI index is given a value according to the decision tree of the region, which is based on the subjective analysis of the summer of 2009. The SWI index value depends on which and how many predictors were found in each set of points and the value of the continuous predictors. For the two highest classifications of the decision tree, the higher the number of predictors found associated to the thunderstorm's structure, the higher the SWI index. Mainly for the other classification, in a case where the same structure predictors are found, if the value of the continuous predictors increases (the basic ingredients for severe thunderstorms), the value of the SWI increases as well, although an increase in the value of some severe thunderstorm ingredients can compensate for a smaller number of structure predictors found. These behaviors can be seen in Tables 4.4, 4.5, 4.6 that describes the decision tree for each region. For example, in the decision tree developed for Quebec, if all the radar-like features of severe thunderstorms are found — an overhang, a severe updraft, a mesocyclone, and a bounded weak echo region — the SWI index has a value of 100. However, if only

an overhang, a severe updraft, and a bounded weak echo region are detected and that the vertical moisture flux, the liquid water content, and the SWEAT are greater than the highest threshold of the decision tree, the SWI index has a value of 80. It has a lower value than the previous one, since less structural features of severe thunderstorm were detected. In addition, if the same radar-like features are found — an overhang, a severe updraft, and a bounded weak echo region —, but that the vertical moisture flux, the liquid water content, and the SWEAT are lower than previously and are only higher than the lower threshold of the decision tree, the SWI index has a value of 50. In this case, the SWI index has a lower value because the moisture availability, which is a necessary ingredient to get severe convection, is lower than the previous case. However, the SWI index also has a value of 50 if an overhang and a severe updraft are detected and that the vertical moisture flux, the liquid water content, and the SWEAT have a value greater than the previous case. Even though less radar-like features are detected, the moisture availability is greater than the previous case. Thus, it compensate for the fewer number of structural features found.

The SWI index was generated for each day of the summer of 2009 over each region. Then, it was verified objectively using the Method for Object-Based Diagnostic Evaluation (MODE) tool from the Model Evaluation Tools package (MET), which was developed by the Verification Group at the Research Applications Laboratory at National Center for Atmospheric Research (NCAR). The MODE tool will be explained in the next section. The MODE tool was used to verify if the classification of our decision tree was designed correctly, so the

SWI	OH	SU	MESO	WER	LWC	LWC7	VMF	SHR3	SHR6	VIF	SWEAT
100	×	×	×	×	–	–	–	–	–	–	–
90	×	×	×	–	–	–	–	–	–	–	–
80	×	×	–	×	>25000	>10000	>4000	–	–	–	–
70	×	–	×	×	>20000	>10000	>3500	–	–	–	–
70	–	×	–	–	>30000	>12000	>5000	>60	–	>100	–
70	–	×	–	–	>30000	>12000	>5000	–	>90	>100	–
60	×	×	–	×	>20000	>10000	>3500	–	–	–	–
60	×	×	–	–	>25000	>10000	>4000	–	–	–	–
50	×	×	–	–	>20000	>10000	>3500	–	–	–	–
50	–	×	–	–	>25000	>11000	>4000	–	–	>150	–
40	×	–	×	–	>20000	>10000	>3500	–	–	–	–
40	×	–	–	–	>25000	>10000	>4000	–	–	–	–
40	–	×	–	–	>25000	>10000	>4000	>60	–	>100	–
40	–	×	–	–	>25000	>10000	>4000	–	>90	>100	–
30	×	–	–	×	>20000	>10000	>3500	–	–	–	–
20	×	–	–	–	>20000	>10000	>3500	–	–	–	–
20	×	–	–	–	>25000	>10000	<4000	–	–	–	–
10	×	–	–	–	>20000	>10000	<4000	–	–	–	–
10	–	×	–	–	>25000	>10000	>4000	>60	–	–	–

Table 4.4: Decision tree for the SWI index over the Alberta window. The first column is the value of the SWI index based on which predictors were found and their corresponding value. For the binary predictors, an '×' indicates that the predictor in the corresponding column is needed in order to assign the corrresponding value of the row of the SWI index and an '–' indicates that the predictor in the corresponding column is not needed. For the continous predictors, in order to assign the corrresponding value of the SWI index of the row the predictor needs to have a value greater than the value indicated its column.

SWI	OH	SU	MESO	WER	LWC	LWC7	VMF	SHR3	SHR6	VIF	SWEAT
100	×	×	×	×	–	–	–	–	–	–	–
90	×	×	×	–	–	–	–	–	–	–	–
80	×	×	–	×	>40000	>10000	>6000	–	–	–	>200
70	×	×	–	×	>35000	>9000	>5000	–	–	–	>200
70	×	–	×	×	>35000	>9000	>5000	–	–	–	>300
60	–	×	–	–	>40000	>10000	>5000	>60	>90	–	>200
50	×	×	–	×	>30000	>8000	>5000	–	–	–	>200
50	×	×	–	–	>35000	>10000	>5000	–	–	–	>200
40	–	×	–	–	>30000	>9000	>5000	>60	>90	–	>200
30	×	–	–	×	>35000	>10000	>5000	–	–	–	>200
30	×	–	–	–	>40000	>10000	>5000	–	–	–	>300
20	×	–	×	–	>35000	>9000	>5000	–	–	–	>200
10	–	×	–	–	>25000	>8000	>5000	>60	>90	–	>200

Table 4.5: Decision tree for the SWI index over the Quebec window. The same convention as Table 4.4 is used.

SWI	OH	SU	MESO	WER	LWC	LWC7	VMF	SHR3	SHR6	VIF	SWEAT
100	×	×	×	×	–	–	–	–	–	–	–
90	×	×	×	–	–	–	–	–	–	–	–
80	×	×	–	×	>40000	>10000	>6000	–	–	–	>200
70	×	×	–	–	>35000	>10000	>6000	–	–	–	>200
70	×	×	–	–	>30000	>9000	>5000	–	–	–	>300
60	×	–	–	–	>40000	>10000	>6000	–	–	–	>300
60	×	–	–	×	>35000	>10000	>5000	–	–	–	>200
50	×	×	–	×	>35000	>9000	>5000	–	–	–	>200
50	–	×	–	–	>40000	>12000	>6000	–	–	–	>200
40	×	–	×	×	>35000	>9000	>5000	–	–	–	>200
40	×	×	–	–	>30000	>9000	>5000	–	–	–	>200
30	×	×	–	–	>30000	>9000	<5000	–	–	–	>200
30	×	×	–	×	>30000	<9000	>5000	–	–	–	>200
30	×	×	–	–	<30000	>9000	>5000	–	–	–	>200
20	×	–	×	–	>40000	>10000	>5000	–	–	–	>200
20	×	×	–	–	>30000	>9000	>5000	–	–	–	<200
10	×	–	×	–	<40000	>10000	>6000	×	–	–	>200
10	×	–	×	–	>40000	<10000	>6000	×	–	–	>200
10	×	–	×	–	>40000	>10000	<6000	×	–	–	>200

Table 4.6: Decision tree for the SWI index over the Ontario window. The same convention as Table 4.4 is used.

verification was performed on the SWI index having a value equal to 10, 20, …, 100, and greater than or equal to 10, 20, …, 100.

Statistics such as the 90% confidence interval (CI) of the POD, FAR, and the entries of the 2×2 contingency table were then derived from the object-oriented verification for each value. The CIs were analyzed to decide whether the classification was correct. Finally, minor changes were made to the classification of the decision tree.

4.4 Objective analysis

The MODE tool from the MET package from NCAR is used for the objective analysis. We chose this method of verification because traditional verification measures, based on simple grid overlay, would have greatly penalized the skill of our SWI index forecast due to small location errors (Brown et al., 2002). Moreover, results from standard verification methods would not have agreed with the forecast's quality perceived by a forecaster (Davis et al., 2006). See Brown et al. (2002) for more details on the inadequacies of the measures-oriented method for convective forecasts. The major advantage of the object-oriented method is that it merges the traditional method with the subjective analysis by identifying features of the forecast and the observation and then deciding whether a given forecast feature reproduces an observation feature, but still deriving statistics. In other words, the object-oriented method resembles the forecast evaluation skill by a human analyst, but also provides meaningful statistical results (Brown et al., 2007). The MODE tool is an automated process

using the object-based approach. It takes as input a gridded forecast file, a gridded observation file, and a configuration file to set the criteria and thresholds defined by the user, and goes through the following steps: object identification, the computation of object attributes, the merging of forecasted and observed objects, the matching of forecasted objects with observed objects, a comparison of forecasted and observed object attributes, and the summarization and comparison of many cases. The MODE automated process will be summarized in the following paragraphs. For more details and information, please refer to Brown et al. (2007) and to the following website: http://www.dtcenter.org/met/users/docs/users_guide/MET_Users_Guide_v1.0.pdf.

For the first step, MODE will identify objects on a 2D scalar forecasted and observed field. The forecast and the observation field need to be on the same grid. To begin the object definition process, the forecast and the observation field are convolved with a circular shape with a radius defined by the user (Brown et al., 2007). The choice of radius depends on the goal of the user and the data that he/she is using. In our case, the convolution-disk radius is different for the observation and the forecast field. I have defined a larger convolution radius for the observation field than the forecast field because the forecast field is continuous, while the observation field is scattered and made of discrete points. Therefore, a convolution radius larger for the observation field than the forecast field takes into consideration the scarcity of the observations. During the convolution process, the value at each grid point will be replaced with an average value within a disk whose center is placed at each grid point (Davis et al., 2006).

In other words, the convolution process acts like a smoothing process. At this point, a threshold is applied on the convolved field in order to generate objects that look like objects that would have been drawn by a human analyst (Brown et al., 2007) — these are called single objects. The object generation process' final step is the restitution of the original data into the defined objects (Brown et al., 2007). Outside the defined objects, the value of the grid points is zero. The convolution process is demonstrated in Fig. 4.2. In this research, the forecasted objects are created from the SWI index forecast and the observed objects are created from SW observations. SW observations are binary — a value of 0 for no SW and a value of 1 for a SW occurrence of any type. A SW occurrence of any type is defined as either a tornado, a mesocyclone, hail with diameter larger than 20 mm, wind speeds higher than or equal to 90 km/h, or 25 mm of rainfall in less than one hour. Before the convolution process, a threshold is applied on the raw forecasted field in order to keep only the forecasted SWI index value in which we are interested. For our verification purpose, the following thresholds are used on the raw forecast before the convolution process: ≥ 10, ≥ 20, ≥ 30, ≥ 40, ≥ 50, ≥ 60, ≥ 70, ≥ 80, ≥ 90, and 100. No threshold is used on the observed field, since our SW observations are binary. Then, the convolution process is applied on the forecasted and observed fields. The convolution radius of the forecast field is 20 grid squares (approximately 20 km), and 35 grid squares (approximately 35 km), for the observation field. Also, the convolution threshold used to generate the objects is defined as any value greater than 0 will be kept. After the convolution process, the observed data and masked raw forecast data are restored into the

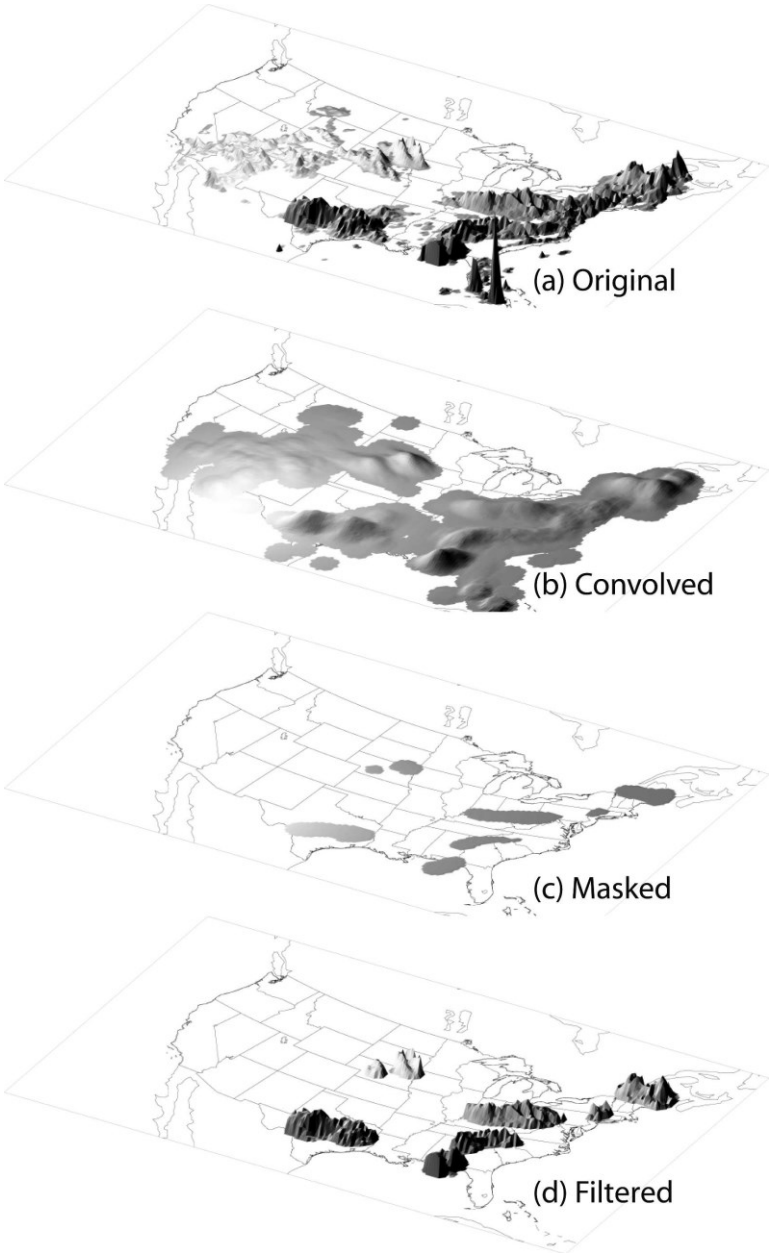

Fig. 4.2: Example of the application of object-identification approach to a particular WRF precipitation forecast grid: (a) original precipitation grid, with intensity presented as the vertical dimension; (b) convolved grid, after the smoothing operation has been applied; (c) masked grid, following the application of the intensity threshold; and (d) filtered grid, showing the precipitation intensities inside the identified objects (Davis et al., 2006).

objects.

The next step in the MODE automated process is the measurement of objects' attributes. The single objects are associated with a simple geometric shape, so that attributes can be computed for every single object (Davis et al., 2006). The attributes computed for single objects are:

- Intensity: A set of quantiles for each field to provide a good representation of the field's distribution.
- Area: Number of grid squares that the object occupies.
- Centroid: Center of mass of the object.
- Axis angle: Orientation of the object major axis.
- Curvature: Deviation from straightness by fitting a circular arc to the object.
- Complexity: Comparison of the object's area to its convex hull area
- Aspect ratio: Ratio of the width of a rectangle that just fits the object and has the same axis angle as the object by its length.

The boundary of an object is the line that defines its border. In the case of a composite object composed of many single objects, there will be several such outlines, one for each object. The convex hull is a shape that envelops an object or a set of objects, which can be visualized by the shape that a rubber band would have if it is stretched to fit an object or a set of objects. Figure 4.3 illustrates the convex hull and the boundary of an object. At this point, objects of the same field are compared to each other. Moreover, each object from the forecast field is compared to each object in the observation field. When two objects are compared

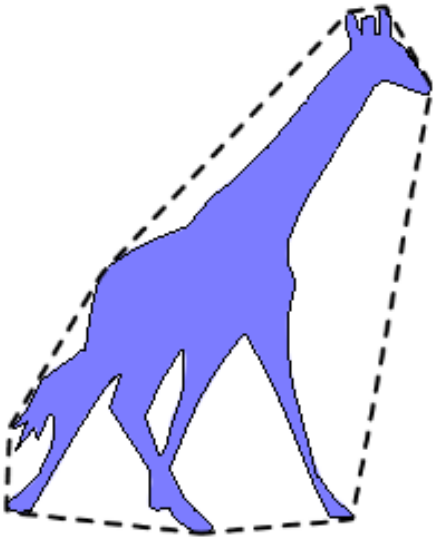

Fig. 4.3: The convex hull of this object is identified by the dashed line, and the black contour identifies the boundary of the object. The image is from the Developmental Testbed Center.

to each other they are called a paired object. Attributes also need to be computed for paired objects. Therefore, single object's attributes are used to compute the paired object's attributes. The attributes calculated for pairs of objects are:

- Centroid distance: Distance between the objects' centroids.
- Convex hull distance: Distance between the objects' convex hulls.
- Boundary distance: Distance between the objects' boundaries.
- Angle difference: Difference between the objects' axis angles.
- Area ratio: Ratio of the area of the paired objects.
- Intensity ratio: Ratio of the percentile intensity of two objects.
- Complexity ratio: Ratio of the complexity of two objects.
- Union area: Total area in either objects.
- Intersection area: Area inside both objects.
- Symmetric difference: Area inside one object, but not both.

Next, MODE matches and merges objects. The matching process associates objects from two different fields together. Merging objects consists in associating objects from a same field together to create larger composite objects, called a cluster. Presently, the MODE tool uses the fuzzy logic method (Yager et al., 1987) to match and merge objects. One of the main advantages of the fuzzy logic method is that it can take a large number of attributes into consideration to match and merge objects (Brown et al., 2007). Another advantage is that it objectively simulates how a human analyst would match objects (Brown et al., 2007). To achieve merging and matching, an interest map, $I_i(\alpha_i)$, is defined for each attribute, i, to specify the range over which the attribute is important and the range over which it is not (Brown et al., 2007). Figure 4.4 illustrates an interest map used in MODE. Also, confidence maps, $C_i(\alpha)$, are defined for each attribute to determine how confident the user is in the value of the attribute i (Brown et al., 2007). Confidence maps have values ranging from 0 to 1. However, in MODE, only the angle difference has a confidence map because this paired attribute is the most likely to have a large forecast error; all the other attributes have their confidence

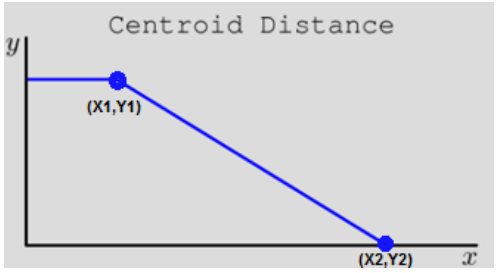

Fig. 4.4: Interest map (y) for the centroid distance (x). Here, we can see that the interest map is constant from 0 to X1, then the interest map decreases linearly down to 0 between X1 and X2.

maps set to a constant, 1. In addition, a scalar weight, w_i, is assigned by the user to each attribute, according to the importance that the user gives to each attribute for the matching process to follow (Brown et al., 2007). Finally, the interest maps, confidence maps, and weights are combined to compute to the total interest function $T(\alpha)$:

$$T(\alpha) = \frac{\sum_i w_i C_i(\alpha) I_i(\alpha_i)}{\sum_i w_i}. \tag{4.1}$$

The user defines the total interest threshold that is applied to the total interest value computed with the total interest function when two objects are compared during matching or merging (Brown et al., 2007). If the value of the total interest is greater than or equal to the threshold, the object will be considered a good match and will be matched or merged.

In this research, we are mainly interested in the distance separating the forecasted and the observed objects, since we only had access to discrete point observations. Consequently, results from the geometric attributes would be meaningless. Also, since we are comparing an index to an occurrence, intensity attribute are useless. Thus, the following paired attributes are the most important for this research, and they are listed by order of importance: the convex hull distance, the boundary distance, and the centroid distance. Equations 4.2 to 4.4 show the equations of the interest map of these three important paired attributes. According to the level of importance of each paired attribute, we give a weight of four to the convex hull distance, two to the boundary distance, and one to the

$$I(\alpha) = \begin{matrix} 1 & ,[0,60[\\ 1-\frac{\alpha}{600} & ,[60,600] \\ 0 & ,\ ]600,\infty \end{matrix}$$

Eqn. 4.2: The equation of the centroid distance's interest map, where α correspond to the centroid distance in grid size unit.

$$I(\alpha) = \begin{matrix} 1-\frac{\alpha}{400} & ,[0,400] \\ 0 & ,\ ]400,\infty \end{matrix}$$

Eqn. 4.3: The equation of the boundary distance's interest map, where α correspond to the boundary distance in grid size unit.

$$I(\alpha) = \begin{matrix} 1-\frac{\alpha}{400} & ,[0,400] \\ 0 & ,\ ]400,\infty \end{matrix}$$

Eqn. 4.4: The equation of the convex hull distance's interest map, where α correspond to the convex hull distance in grid size unit.

centroid distance. As mentioned earlier, a total interest value is computed using the total interest function, which uses the interest map and the weights, and is compared to the total interest threshold to decide which objects will be merged and matched. For the objectives of this study, the total interest threshold was set to 0.55. However, what does a total interest threshold value of 0.55 mean concretely? By looking to the interest map of our three important paired attributes; convex hull distance, boundary distance, and centroid distance, we can approximate the maximum distance separation of two paired single objects, created by the convolution process from a single point forecast and a single point

observation, that have a total interest of 0.55. The reader should refer to the equations in Eqns. 4.2 to 4.4 and to the total interest function equation (4.1). By plugging different distances into the total interest function, we find that a total interest threshold of 0.55 corresponds to a distance of approximately 190 km between two objects. The same threshold is applied for the merging process and the matching process. Therefore, in this research, if two objects are less than roughly 200 km apart, they will be merged or matched together. A distance of less than or equal to approximately 200 km is a reasonable distance. From a forecaster's point of view, 200 km roughly corresponds to the distance between the western edge of the island of Montréal and Trois-Rivières. In addition, the geometric shape of most Quebec warning regions has a diagonal that is approximately 200 km long. Figure 4.5 illustrates these previous arguments. Therefore, it seems to be a good distance to use to match observed and forecasted objects.

At this point, to get a better understanding of the merging process, we will go through an example. Figure 4.6 shows the raw forecast field and Fig. 4.7 illustrates the forecasted objects after the convolution process. In this example, six single objects are found in the forecast field. First, each single object is assigned an identification number from 1 to 6. In the merging process, all six objects are compared to each other and a total interest value is computed each time, according to the total interest function described earlier. Figure 4.8 demonstrates the merging process. The compared objects that have a total interest value greater than or equal to the total interest threshold are merged together. In Fig. 4.8, we

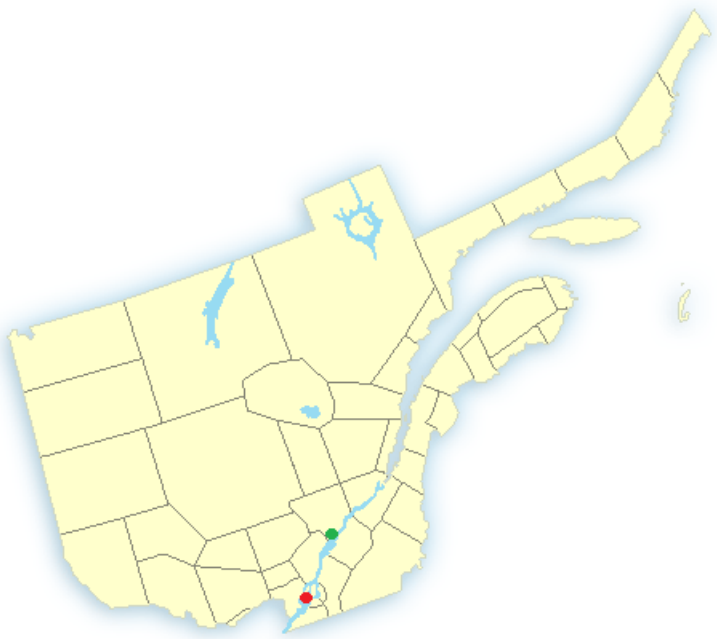

Fig. 4.5: Warning public regions of Quebec (EC). The red dot is positioned on the western edge of Montréal Island, the green dot is positioned on Trois-Rivières, and the distance between the two corresponds to approximately 180 km, close to our threshold distance differencing a good and a bad match. The gray lines delimitate the Quebec warning public region.

can see that objects two to six are all merged together, since they all had a total interest value of greater than 0.55 when compared together. Object number one had a total interest value of less than 0.55 when compared to the other objects. Therefore, it is not merged with any object. In this case, the result of the merging process is two composite objects. The first composite object is composed of the single object number 1, and the second composite object is composed of the single objects numbers 2 to 6. The MODE tool makes it easy to visualize which objects are merged together, since all objects with the same color are merged together and a thick solid contour black line, called the convex hull, encloses the resulting compound objects.

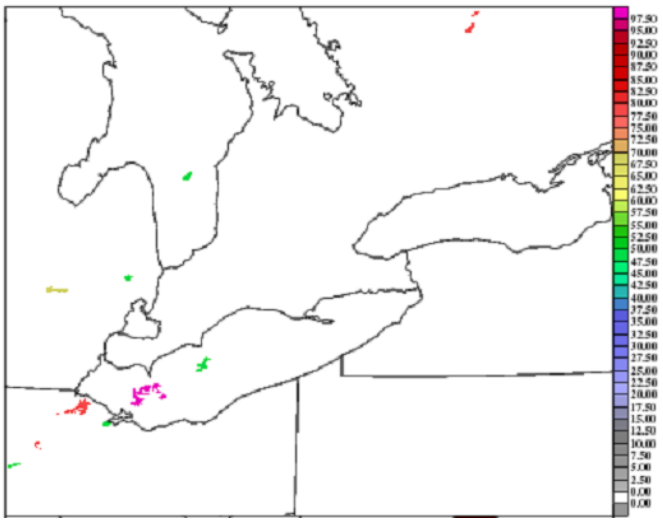

Fig. 4.6: The SWI index forecast for July 28, 2009 as the forecast field.

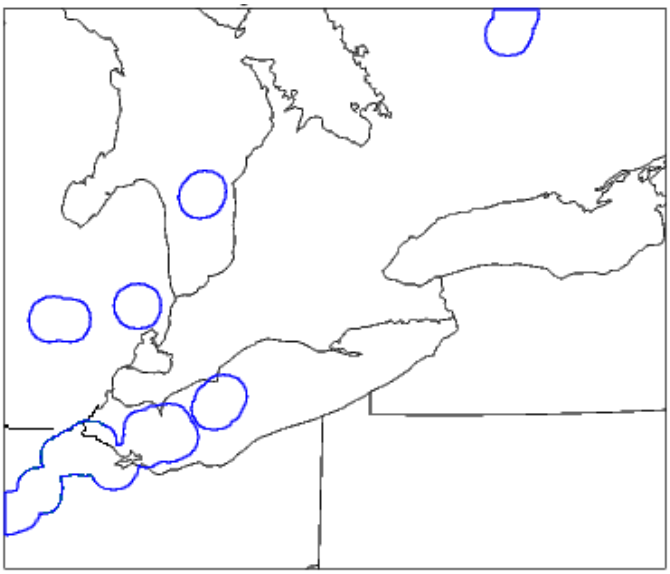

Fig. 4.7: The convolved forecast field. Each forecast object is identified by a closed blue contour. Thus, in this case, there are six forecast objects.

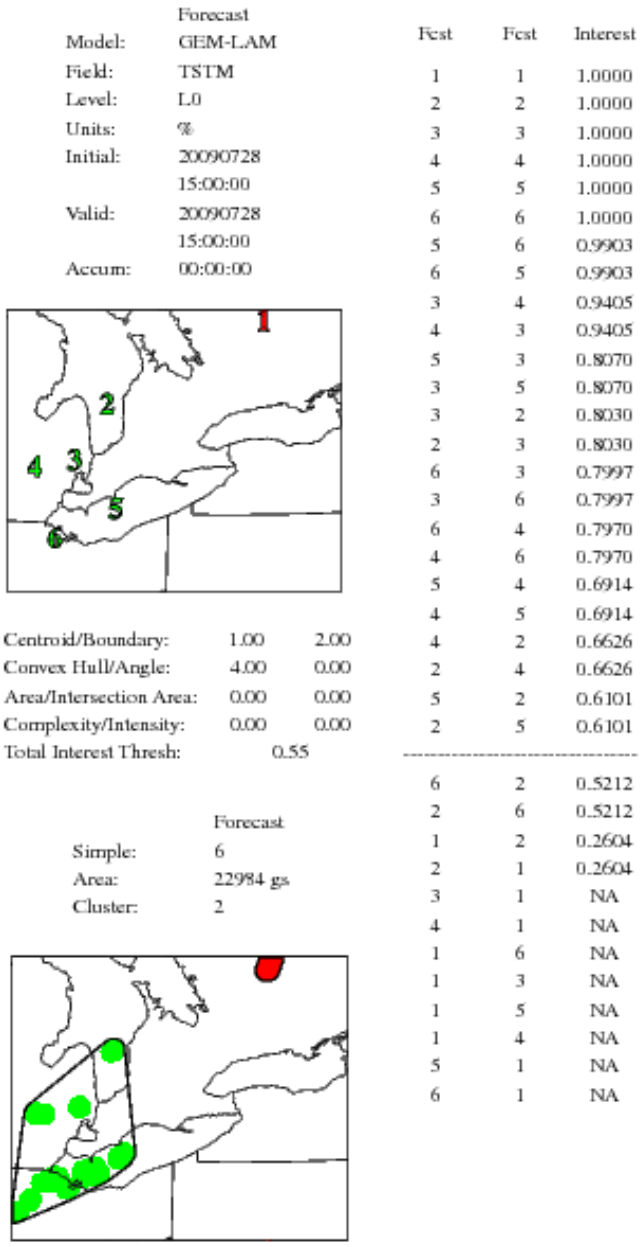

Fig. 4.8: The merging process. Each forecasted object is assigned an identification number (top image). All six forecasted objects will be compared to each other. Each time that a comparison is done between two forecasted objects a total interest value is computed. Objects with a higher total interest value than the total interest threshold will be merged together. Each object comparison is listed in the column to the right of the images. The total interest threshold is indicated by the dashed line in the column to the right of the images. Thus, every object comparison that is above the dashed line has a total interest value greater than the threshold, and the compared objects will be merged together. The bottom image illustrates the final forecasted clusters, identified by a thick solid contour line. Objects of same color belong to the same cluster.

Now, an example of the first step of the matching process is presented and illustrated in Fig. 4.9. It is very important to be aware that this is not the final matching step. The final matching step matches the forecasted clusters with the observed clusters while, on the other hand, the first step of the matching process matches the single forecasted objects with the single observed objects. The first step of the matching process verifies the potential of matching forecasted clusters with observed clusters. If there are single forecasted objects that could be matched with single observed objects, the MODE tool will go to the final matching step to match clusters together. Otherwise, it stops there. Let us go through an example of the first step of the matching process illustrated in Fig. 4.9. First, each single object in the forecast field and the observation field has been assigned an ID number. There are six single forecasted objects and two single observed objects defined by the convolution process. During the first step of the matching process, each forecast object is compared to each observation object. For each comparison between the two fields, a total interest value is calculated. If the total interest value is greater than or equal to the total interest threshold, MODE will go to the final step of matching once every comparison is done.

The final step of the matching process matches the forecasted clusters to the observed clusters. Figure 4.10 demonstrates the cluster matching process. First, each cluster's attributes are computed. Then, the paired clusters' attributes are computed. The paired clusters are deduced from the previous comparison between the forecasted single objects and the observed single objects. MODE looks to previous comparisons that had a total interest value higher than the total

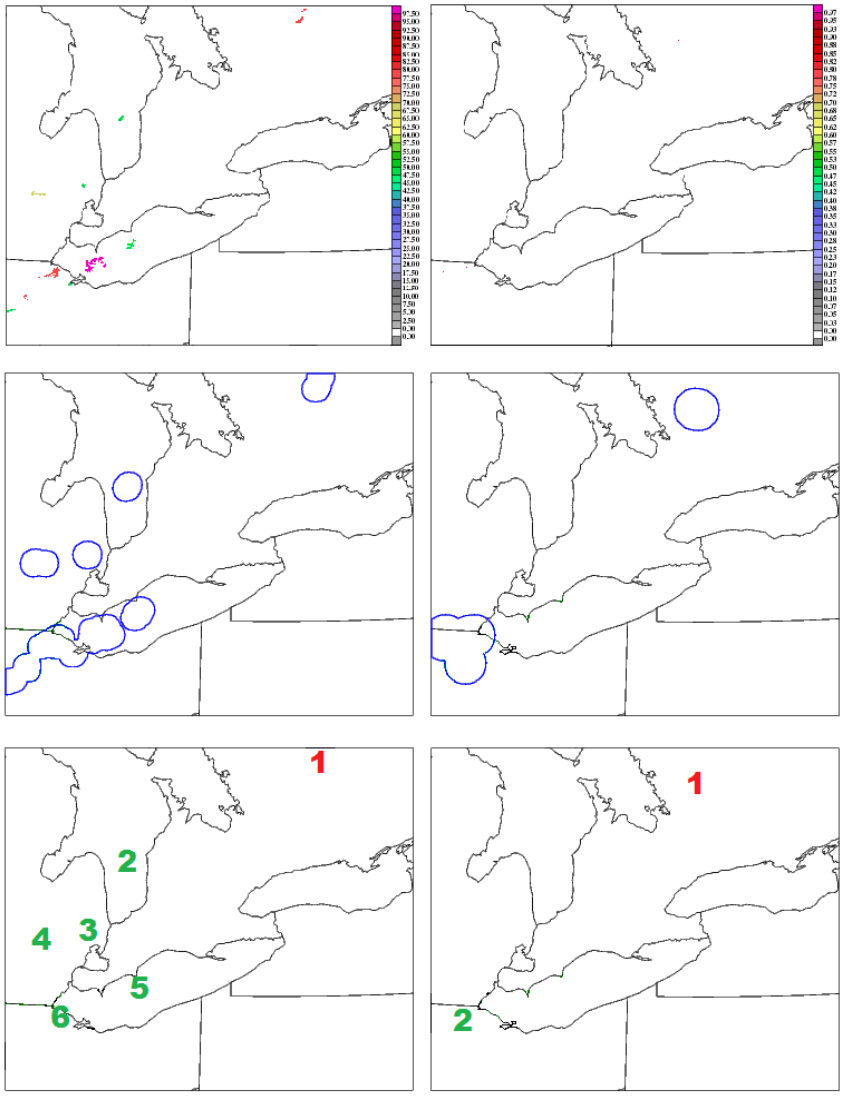

Fcst	Obs	Interest
6	2	1.0000
1	1	0.9465
4	2	0.8454
5	2	0.7778
3	2	0.7746
2	1	0.4836
2	2	0.4508
3	1	0.1849
5	1	NA
6	1	NA
1	2	NA
4	1	NA

Fig. 4.9: The first step of the matching process. The top left image is the raw forecast field, and the top right image is the raw observation field. The left centered image is the convolved forecasted field, and the right centered image is the convolved observed field. In the centered image, a closed blue contour identifies an object. Thus, there are six single forecasted objects and two single observed objects. Each object of the forecasted field is compared to each object in the observed field, and at every comparison, a total interest value is computed. In the column to the right of the images, each comparison is listed along with their corresponding total interest value. The total interest threshold is indicated by the dashed line. Thus, the first step of the matching process found that forecasted objects could be matched to the observed objects, since there are a few comparisons that have a total interest value greater than the total interest threshold. Therefore, the MODE tool will go through the final matching step.

interest threshold and identifies the clusters to which each compared single object belongs. With this information, the clusters are paired together and their paired attributes are calculated. Then, the paired attributes are used tocompute a total interest value for each paired cluster. If the paired clusters have a total interest value greater than the total interest threshold, the paired clusters are considered a match, and they are matched together. In MODE output files, it is easy to

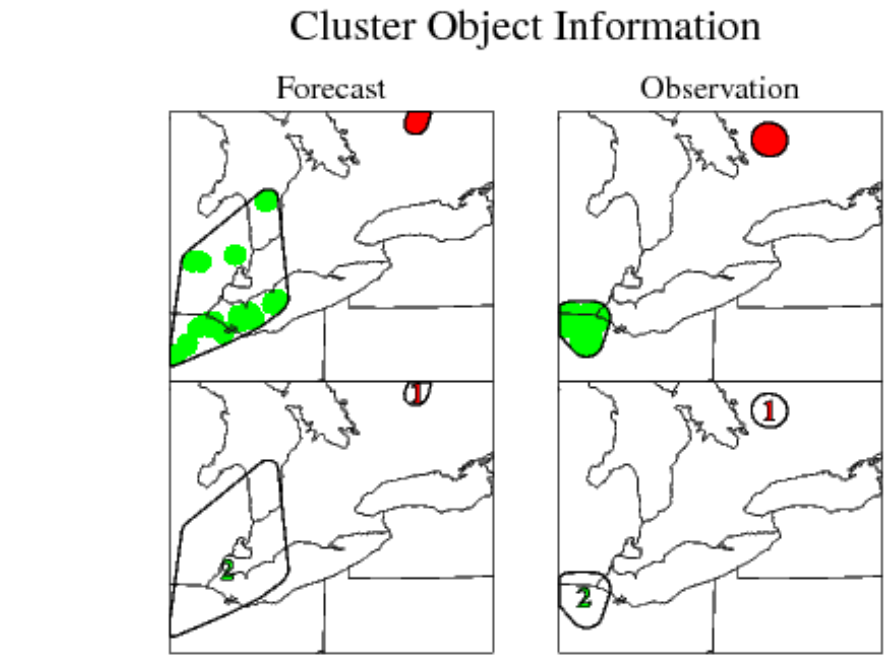

CLUS PAIR	CEN DIST	ANG DIFF	FCST AREA	OBS AREA	INTER AREA	UNION AREA	SYM DIFF	FCST INT50	OBS INT50	FCST INT90	OBS INT90	TOT INTR
1	87.51	48.61	2198	4359	0	6557	6557	80.00	100.00	80.00	100.00	0.9465
2	91.96	38.99	20786	9897	4527	26156	21629	80.00	100.00	100.00	100.00	0.9956

Fig. 4.10: The cluster matching process. The first column of images represents the forecast clusters. The second column of images represents the observation clusters. Paired clusters are chosen based on the comparison between the observed and forecasted single objects and their corresponding total interest values showed in Fig. 4.9. The paired cluster attributes are calculated and can be seen below the images. A total interest value is computed from the paired cluster attributes for each paired cluster. The paired cluster having a total interest value greater than the total interest threshold are matched together. Observed and forecasted clusters of the same colors are identified as being matched together.

visualize if any observation clusters have been matched to forecast clusters, since they will have the same color. Thus, in Fig. 4.10, one can clearly see that the forecast cluster combining the single forecast objects two to six is matched to the observed cluster containing the single observed object number two, and that the forecast object number one is matched to the observation object number one.

Finally, we want to accumulate and compare many cases to get significant statistics. In our case, we will use the MODE-Analysis tool that rapidly gets the practical information that we need from the MODE output files. This process is explained in the next section.

4.5 Scores

As mentioned previously, the MODE-Analysis tool is used to get the data that we need from the MODE output files. The MODE-Analysis tool will allow us to build a 2×2 contingency table from the MODE output files in order to compute skill scores. The MODE-Analysis tool provides the number of grid points of matched and unmatched single objects for the forecast, the observation, and both. Figure 4.14 illustrates how a 2×2 contingency table is built from the MODE-Analysis tool.

Once the MODE tool followed by the MODE-Analysis tool have run for all three regions on each summer day, producing a contingency table for each day, a bootstrap is done on the contingency tables in order to generate more meaningful statistical CI for the scores. The bootstrap method is a resampling technique that allows us to build CI, which would normally be difficult because

		Observed	
		Yes	No
Forecasted	Yes	Union of matched forecasted and observed objects	Unmatched forecasted objects
	No	Unmatched observed objects	Points outside any single objects

Fig. 4.11: Contingency table built from the object-oriented method verification. Each entry of the contingency table contains the sum of the number of grid points of that particular entry.

the distribution of the data is unknown, and provide an estimation of the distribution's uncertainty (Kyselý, 2008). More precisely, the nonparametric bootstrap method is used in this research. A summary of this method follows, but for a more detailed explanation, please consult Chernick (1999). First of all, the nonparametric bootstrap method makes no assumptions about the distribution of the data. The first step of the nonparametric bootstrap method is that a sample of the same size as the original dataset is randomly drawn from the original dataset with replacements, without considering that the sample taken is removed from the set. In our case, if there are *n* summer days over which the model was run for a region, there are *n* contingency tables. The original dataset contains the *n* contingency tables. Thus, during the first step of the nonparametric bootstrapping method, there will be *n* contingency tables that will be randomly selected from the original dataset, the *n* contingency tables, with replacements. The next step is to compute the sample's statistics of interests. In our case, the statistics of interest are scores such as the Probability of Detection. The scores used in this research will be discussed in the next section. The statistics of interests are kept in memory

for later use. These two steps are repeated a large number of times, *N*. As showed by Efron and Tibshirani (1993), *N* should be at least 1000. Therefore, in this study, *N* is 1000. Finally, the statistics of interests computed from the samples are used to generate a bootstrap CI for each statistic of interests. For this study, the bootstrap 90% CI was calculated for each score.

The scores that are computed include the Probability of Detection (POD), False Alarm Ratio (FAR), Heidke Skill Score (HSS), Peirce Skill Score (PSS), Bias (BIAS), and Equitable Threat Score (ETS). The POD represents the proportion of events that were correctly forecasted (Donaldson et al., 1975). The FAR is the proportion of forecasted events that were not observed (Donaldson et al., 1975). The HSS is the proportion of correctly forecasted events and non-events, but also takes into account the proportion of correct forecasts predicted by chance without skill (Heidke, 1926). The PSS is the proportion of correctly forecasted events minus the proportion of incorrectly forecasted events (Peirce, 1884). The BIAS is the ratio of forecasted events and observed events (Donaldson et al., 1975). The ETS can be seen as the conditional probability that an event was correctly forecasted, given that the event was either forecasted, observed, or both, but it also takes into consideration the number of hits obtained by chance (Gilbert, 1884).

Chapter 5

Results

5.1 Forecasts v. observations

As explained in Section 4.4, the object-oriented method was used to verify the SWI index forecasts against the SW observations for each domain of interest: Southern Ontario, Southern Quebec, and Alberta. The configurations for the MODE tool were the ones mentioned in Section 4.4. During the analysis, the only variable that was changed in the MODE configuration was the raw threshold used before the convolution process, because we wanted to verify the skill of the different SWI index values. An objective verification of the forecasts with the observations was achieved for these different SWI index values: ≥ 10, ≥ 20, ≥ 30, ≥ 40, ≥ 50, ≥ 60, ≥ 70, ≥ 80, ≥ 90, and 100. Once the objective analysis was achieved, the bootstrap method, described in Section 4.5, was used to generate the 90% bootstrap CI for the scores for each SWI index value.

First, the results of the verification of the SWI index forecasts with the SW observations for Southern Ontario are presented. Figure 5.1 contains a graph of the POD and the FAR bootstrap means, as well as 90% bootstrap CIs for different values of the SWI index. We expect a low FAR, since an accurate forecast has a FAR value of 0 and a bad forecast has a value of 1. We also desired a high POD, since a good forecast has a POD value of 1 and a bad forecast has a POD value of 0. We will go through these two scores presented in Fig. 5.1. For the Southern

Ontario window, the SWI index forecasts appear to match the SW observations very well, since they have an overall high POD and very low FAR, and the 90% bootstrap CIs of the POD and the FAR are extremely far from each other for all SWI index values. The FAR is, in 95% of the cases, lower than 0.15 for every value of the SWI index. On the other hand, the POD has two major ranges as we change the SWI threshold value (Fig. 5.1): for the SWI index values from ≥10 to ≥50, the POD is, in 95% of the cases, greater than 0.8. Also, for the SWI index values from ≥60 to ≥90, the POD is, in 95% of the cases, approximately greater than 0.65. In addition, the drastic drop in the POD curve between the SWI index values of ≥90 and 100 is as expected, since it indicates that the SWI index with a value of 100 is predicted less often than any other intensity value. Moreover, the 90% CI of the FAR for a SWI index value of 100 is smaller than for every other SWI index value. Therefore, even if there is a drop in the POD between SWI index values of ≥90 and 100, the SWI index with a value of 100 still has skill. The POD and the FAR show that the Southern Ontario forecasts of the SWI index are very accurate overall. Figure 5.1 also contains the bootstrap means and the 90% bootstrap CIs of the HSS and the PSS. Ideally, the HSS should have a positive value and tend towards 1, since an HSS with a value of 1 is a perfect forecast and an HSS with a value of zero is a bad forecast. The PSS behaves the same way as the HSS — if the PSS has a value of 1, the forecast is perfect, and if it has a value of 0, the forecast has no skill. An important thing of which to be aware is that if the HSS is equal to the PSS, the forecast is unbiased. In Fig. 5.1, the value of the HSS and PSS are very close to each other for SWI index values from ≥10 to ≥50,

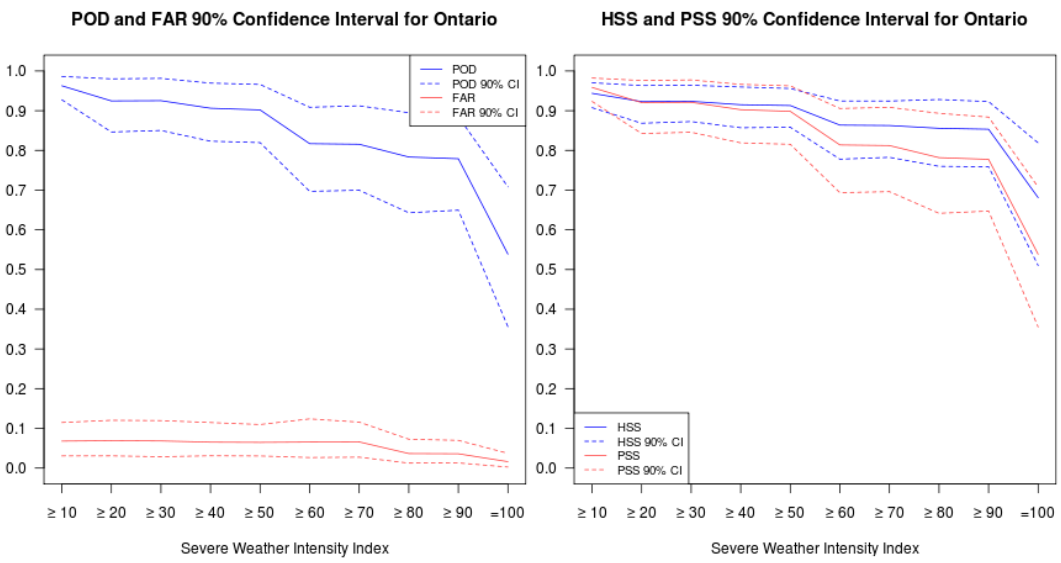

Fig. 5.1: Southern Ontario's scores. The left image corresponds to the 90% bootstrap CIs of the POD and the FAR. The POD is in blue and the FAR is in red. The right image corresponds to the 90% bootstrap CIs of the HSS and the PSS. HSS is in blue and PSS is in red. In both images, the straight lines represent the bootstrap means, while the lower and upper dashed lines are the 90% bootstrap CIs.

but the curves moves farther apart as the SWI index contains a narrower range of intensity. Therefore, the forecast of the SWI index is a little biased for values from ≥10 to ≥50, but becomes more biased as the range of intensity of the SWI index becomes narrower and contains higher intensity. Moreover, we can deduce that the SWI index forecasts have skill, since the HSS and PSS have positive values that are closer to 1 than 0. 95% of the time, both scores are greater than 0.8 for SWI index values from ≥10 to ≥50. Also, in 95% of the cases, both scores have values approximately greater than 0.65 for SWI index values from ≥60 to ≥90. Finally, let us look at the last score graph for Southern Ontario. Figure 5.2 illustrates the bootstrap means and the 90% bootstrap CIs of the BIAS and ETS. The BIAS indicates the forecast's bias — a BIAS with a value greater than 1

implies that the SWI index over-forecasts SW events, and a value smaller than 1 indicates that the index under-forecasts SW events. A forecast with an ETS value of 1 is a good forecast, while a value of 0 indicates a bad forecast. From Fig. 5.2, we notice that there is no clear tendency in the BIAS for SWI index values from ≥10 to ≥50. Depending on the sample, the SWI index forecast can over-forecast or under-forecast SW events since the 90% bootstrap CIs contain values smaller and larger than 1. However, SW events are under-forecasted for SWI index values from ≥60 to 100. The ETS curve indicates that the forecast has skill because, in 95% of the cases, its value is approximately greater than 0.75 for SWI index values from ≥10 to ≥50, and its value is approximately greater than 0.60 for SWI index values from ≥60 to ≥90. Thus, ETS is always positive, and is usually closer to 1 than to 0. In addition, the ETS, just like the other scores, shows that there is an important difference in the score between SWI index values of ≥10 and ≥20 and that there is almost no change in the score for SWI index values from ≥20 to ≥50. Also, there is an important drop in the score between SWI index values of ≥50 and ≥60, but little change from ≥60 to ≥90. Moreover, the most important difference in the score is between SWI index values of ≥90 and =100. Therefore, it shows that there are four more important values for the SWI index for which there are more difference in the scores comparatively to other values: 10, 50, 90, and 100. These values have the most impact on the scores. All the scores seen for the Southern Ontario region imply that the SWI index could be a very good forecast tool for the SW forecasters of Ontario, since every useful score with rare events indicates that the SWI index forecasts were accurate when compared to the

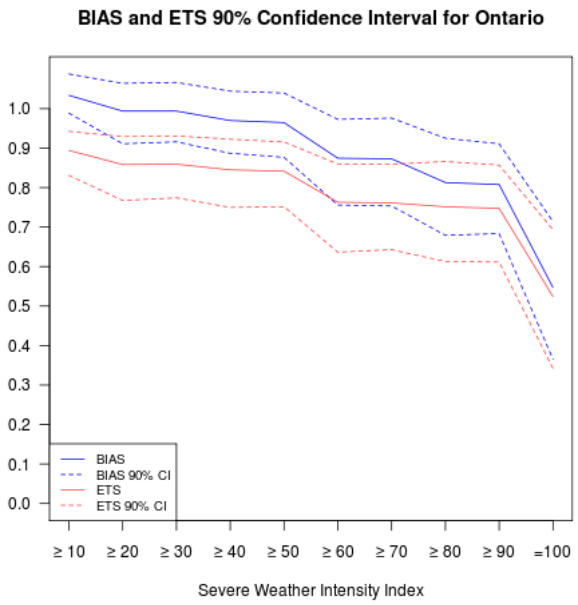

Fig. 5.2: The 90% bootstrap CIs of the BIAS and the ETS for Southern Ontario. The straight lines represent the bootstrap means. The lower and upper dashed lines are the 90% bootstrap CIs. The BIAS is in blue and the ETS is in red.

SW observations for every value of the SWI index. In addition, a subjective verification was done to compare the SWI index forecasts over Southern Ontario with the SW observations and radar images. There were a few SW events missed by the SWI index forecasts that we believe were mainly caused by a wrong initialization of the GEM-LAM 1-km. In other words, the data used to initialize the GEM-LAM 1-km, which came from the GEM-LAM 2.5-km, was not good because the GEM-LAM 1km did not see any convection or weaker convection for those SW events. However, further investigation is required to verify this hypothesis. In addition, for the days where there was no SW observation, but a SWI index value greater than zero was forecasted, SW was usually observed just outside the domain. Therefore, the subjective verification confirms the accuracy

of the SWI index forecasts. In conclusion, the SWI index could be a very good forecast tool for the SW forecasters of Ontario.

Next, the result of the verification of the SWI index forecasts with the SW observations for Southern Quebec is presented. One of the graphs in Fig. 5.3 shows the POD and FAR bootstrap means and 90% bootstrap CIs for different values of the SWI index. The SWI index forecasts have skill for all SWI index values, since the POD is always greater than the FAR and the CIs do not overlap. In fact, they are distinctively apart from each other. In addition, we notice that the FAR means and the 90% CIs decrease as the index's range of intensity becomes narrower to contain the highest intensities. This indicates that, as desired, the SWI index value of 100 is forecasted less often than the SWI index value of 10, but also when a SWI index value of 100 is forecasted, it will most likely be accurate as opposed to a value of 50. Next, Fig. 5.3 also contains the bootstrap means and the 90% bootstrap CIs for the HSS and PSS. For SWI index values from ≥10 to ≥40, the SWI index forecasts have relatively high skill for these two scores. Then, the skill decreases slowly from ≥40 to ≥70. Up to this point, the forecasts have less skill, but still have some from ≥80 to 100. Also, the forecasts are a little biased from ≥10 to ≥40 and become more biased as the SWI index value tends toward ≥90. This is because, when the SWI index's range is broader, the HSS and PSS curves are closer, and move farther apart as the index becomes narrower. Next, some interesting observations can be made about the BIAS of the forecast in Fig. 5.4. We can clearly notice that over Southern Quebec, the SWI index forecast is likely to under-forecast SW events. For SWI values from ≥10 to ≥40,

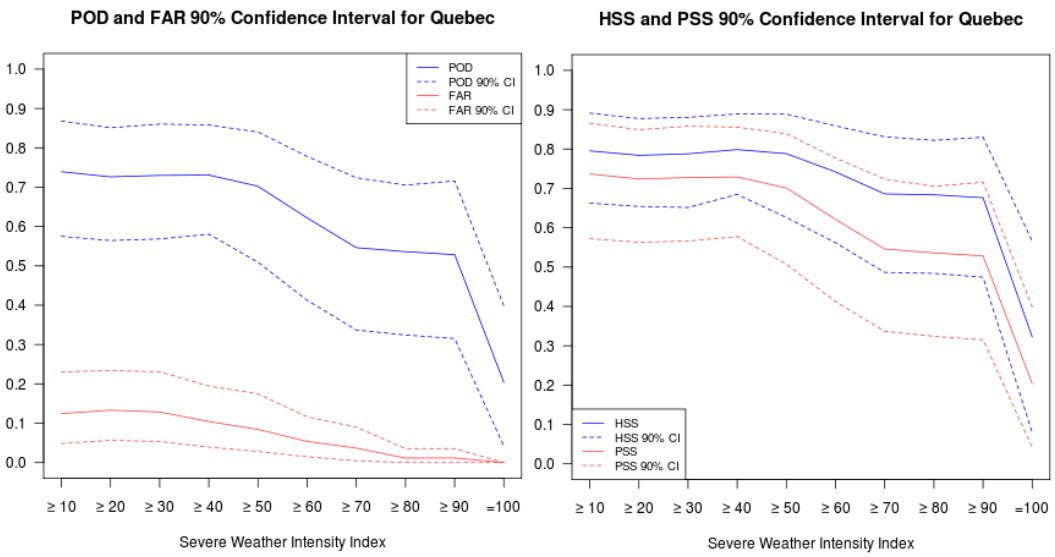

Fig. 5.3: Southern Quebec's scores. The left image corresponds to the 90% bootstrap CIs of the POD and the FAR. The POD is in blue and the FAR is in red. The right image corresponds to the 90% bootstrap CIs of the HSS and the PSS. HSS is in blue and PSS is in red. In both images, the straight lines represent the bootstrap means, while the lower and upper dashed lines are the 90% bootstrap CIs.

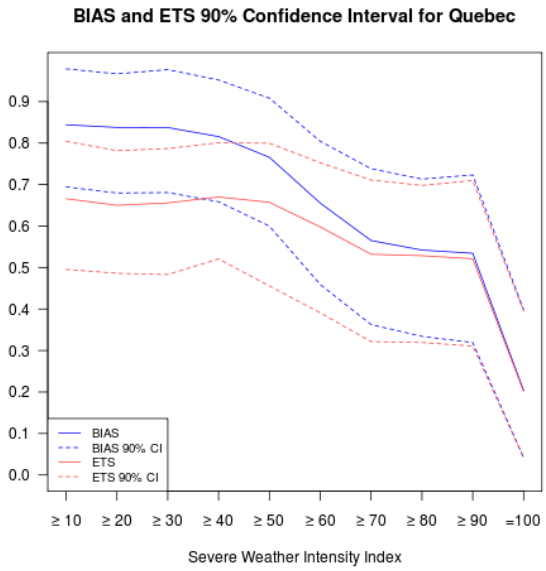

Fig. 5.4: The 90% bootstrap CIs of the BIAS and the ETS for Southern Quebec. The straight lines represent the bootstrap means. The lower and upper dashed lines are the 90% bootstrap CIs. The BIAS is in blue and the ETS is in red.

the SWI index forecasts slightly under-forecasted SW events, but for values ≥50 to 100, the SWI index forecasts pass slowly from slightly under-forecasting SW events to highly under-forecasting SW events. On the other hand, the ETS curve shows the same thing as observed previously and, just like the other scores, it shows that there are four important values for the SWI index for which there are more difference in the scores comparatively to other values: 50, 60, 90, and 100. These values have the most impact on the scores. If we compare the scores of Southern Quebec with those of Southern Ontario, we can observe that the POD, HSS, PSS, and ETS have overall smaller values for Southern Quebec than for Southern Ontario for every SWI index value. Therefore, we can conclude that the SWI index performs better over Southern Ontario than over Southern Quebec. We can also notice that the FAR values for Southern Quebec are usually smaller than those of Southern Ontario. However, this is mainly due to the fact that the SWI index forecast developed for Southern Quebec actually under-forecasts SW events: the SWI index forecast is accurate for the Southern Quebec region when compared with the SW observations, but overall, the index under-forecasts SW events over this region. Therefore, the SWI index can be useful to guide SW forecasters, but it is not as accurate over Southern Quebec as it is for Southern Ontario. A subjective verification of the SWI index forecasts with the SW observations and the radar images was made over Southern Quebec. The subjective verification showed that most of the missed SW events by the SWI index forecast were caused by the spin up of the model. Initially, the microphysical variables of the model are zero. Thus, it takes some time to the

model to create its precipitation (Clark et al., 2007). Therefore, when the convection is simulated in the first few hours of the model run, the liquid water content will be lower than the thresholds of the SWI index decision tree. Moreover, when a SW event was forecasted by the index, but not observed, most of the time, we could observe near-severe cells on the radar that were likely to produce SW. In conclusion, the spin up of the model affects our scores, but the SWI index would be a useful index to guide SW forecasters.

Lastly, the results of the verification of the SWI index forecasts with the SW observations for Alberta are presented. Figure 5.5 illustrates the POD and FAR bootstrap means and 90% bootstrap CIs for the different values of the SWI index. It is easy to notice that the SWI index has less skill over Alberta than over Southern Ontario and Southern Quebec (see Figs. 5.1, 5.3, and 5.5). In Fig. 5.5, the SWI index forecasts have some skill for SWI index values from ≥10 to ≥50, even if the lower limit of the POD CI slightly overlaps with the upper limit of the FAR CI. By comparing Fig. 5.5 to Figs. 5.1 and 5.3, we can confirm that the SWI index forecast has some skill over Alberta, but less than over Southern Ontario and Southern Quebec because, for these two regions, the POD and FAR CIs are far apart, and most importantly, do not overlap. Also, in Fig. 5.5, we can see that the skill decreases slowly from ≥10 to ≥50, and decreases rapidly from ≥60 to 100. However, for a SWI index equal to 100, the lowest limit of the POD CI tends towards 0, which implies that when the SWI index equals 100, it has almost no skill. By looking at the HSS and PSS in Fig. 5.5 and by comparing them to the equivalent graph for Southern Ontario (Fig. 5.1) and Southern Quebec (Fig. 5.3),

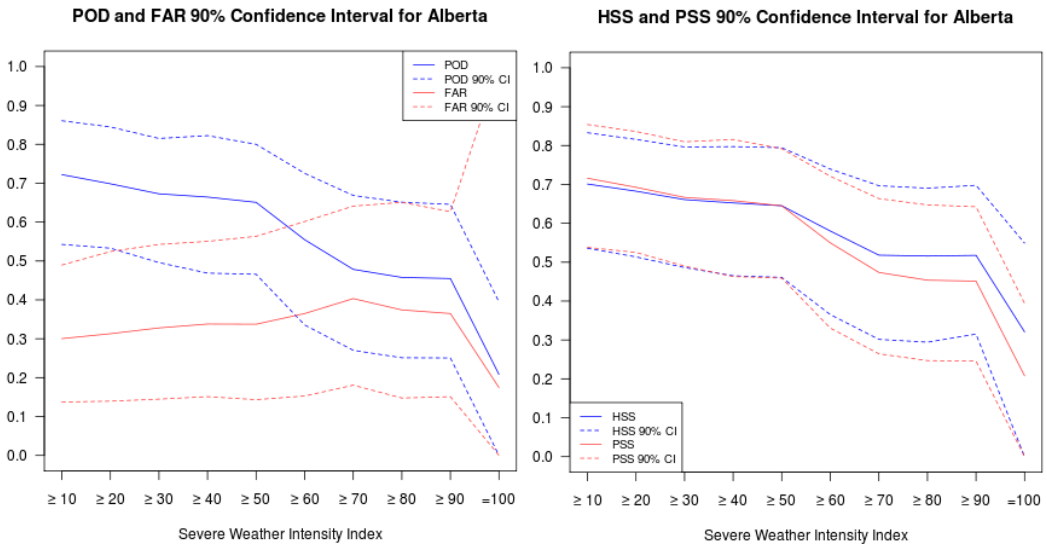

Fig. 5.5: Alberta's scores. The left image corresponds to the 90% bootstrap CIs of the POD and the FAR. The POD is in blue and the FAR is in red. The right image corresponds to the 90% bootstrap CIs of the HSS and the PSS. HSS is in blue and PSS is in red. In both images, the straight lines represent the bootstrap means, while the lower and upper dashed lines are the 90% bootstrap CIs.

we come to the same observations previously made. The values for these two scores are a little smaller than the values of the corresponding scores for Southern Quebec for almost every SWI index value. Thus, the SWI index has a little less skill for Alberta than for the Southern Quebec region. However, some new observations can be made with Fig. 5.6. In this figure, the bootstrap means and the 90% bootstrap CIs for the BIAS and ETS for every value of the SWI index are presented. It is interesting to note that there is no clear tendency about the BIAS for almost every value of the SWI index. The SWI index forecast can over-forecast or under-forecast SW events, depending on the sample for every SWI index value from ≥10 to ≥70. However, the forecasted SWI index with values from ≥80 to 100 clearly under-forecast SW events. The ETS brings no new

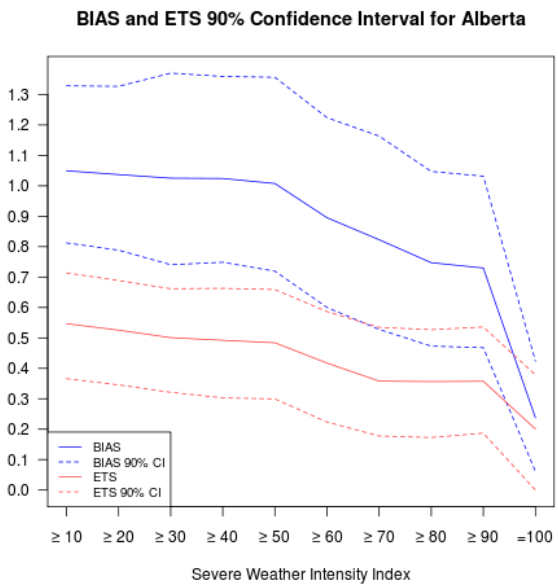

Fig. 5.6: The 90% bootstrap CIs of the BIAS and the ETS for Alberta. The straight lines represent the bootstrap means. The lower and upper dashed lines are the 90% bootstrap CIs. The BIAS is in blue and the ETS is in red.

information, it only confirms what was observed in the previous graphs and shows that there are four important values for the SWI index for which there are more difference in the scores comparatively to other values: 50, 60, 90, and 100. These values have the most impact on the scores. In conclusion, it is evident that the SWI index is less accurate over Alberta than over Southern Quebec and Southern Ontario. It still has some skill for SWI index values ranging from ≥10 to ≥50, but beyond these values, the skill decreases as the range of intensity becomes narrower and contains higher intensity. In order to identify the causes of such bad scores, I did a subjective evaluation of the SWI index forecasts, the post-processed outputs, the SW observations, and the radar images. The low POD and the high FAR are mainly due to the lack of SW observations. By comparing the SW index forecasts with the radar, I noticed that the SWI index forecast was quite

accurate. This is because, if we would have had access to the radar, the number of days where SW was forecasted and observed would have almost doubled. On the radar, most of the days where there was no SW observation available but our index forecasted SW, we could observe very strong thunderstorms with very high reflectivity, which is a good hail indicator. Therefore, the SWI index forecast is very good over Alberta to identify days where there will be intense thunderstorms and to determine whether they will be localized or not. Therefore, from the subjective evaluation, I do think that the SWI index over Alberta would help SW forecasters. However, the index misses a lot of events. From the subjective verification of the index with the radar images, I noticed that the thunderstorms on the radar images that produced SW missed by the index had reflectivity weaker than one would normally expect for severe thunderstorms. For most of the SW event missed by the index, the model did simulate weaker thunderstorm cells with less moisture available. The SWI index over Alberta might be missing near severe events and/or low precipitation supercell. However, further investigation is required to verify this statement. In conclusion, the SWI index would help the Alberta SW forecasters to forecast severe thunderstorms, but the lower category of the decision tree for this region could be modified to include near-severe events and low precipitation supercell in order to miss fewer SW events.

5.2 Forecasts v. severe thunderstorm watches

The goal of this master thesis is to develop a useful automated tool to help SW forecasters emit their SW forecast. To examine if the SWI index could improve

the SW forecast done by a SW forecaster, the SWI index needs to be compared to SW watches from a SW forecaster. Therefore, an objective verification will be performed on both products. The results of the verification of the SW forecasts against the SW observations will be compared to the results of the verification of the SWI index forecasts against the SW observations. This was performed for the Southern Quebec region only. As mentioned previously, at 15 UTC, after having done a thorough analysis of the atmospheric situation, the SW forecaster emits SW watches for every public region (Fig. 1.3) where there is a high probability of having severe thunderstorms. The watches are valid until 02 UTC and the SWI index forecast is valid from 15 UTC to 03 UTC. Thus, they cover almost the same time period, and they can easily be compared to each other. However, the SWI index forecast has a higher resolution than the SW watches. In order to have meaningful results, the data compared needs to be at the same scale. Therefore, an upscaling of the SWI index forecasts and the SW observations to the public regions is required, so that every product is at the same scale. The upscaling is performed in the following way: when the SWI index is greater than a specified value at one grid point, the public region containing this point is flagged to 1, otherwise the region is flagged to 0 (Fig. 5.7). The same procedure is applied to upscale the SW observations.

Once all data are on the same scale, the object-oriented method is used to evaluate the SWI index forecasts and the forecaster-made severe thunderstorm watches against the SW observations. The configurations for the MODE tool are the same as the ones mentioned in Section 4.4, except for the total interest

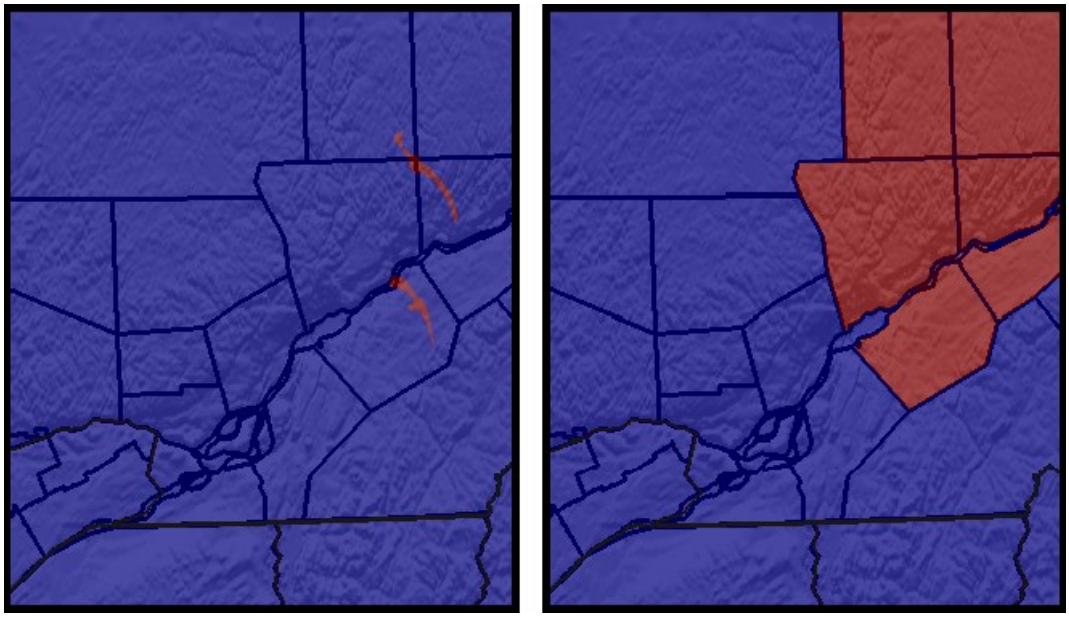

Fig. 5.7: The upscaling process. To the left is the SWI index forecast before the upscaling process, where the blue indicates where the SWI index is zero and the red indicates where the SWI index is greater than zero. To the right is the result of the upscaling process. Regions in red contain at least one point where the SWI index is greater than zero. Regions in blue are where no point with an SWI index greater than zero was found.

threshold and the convolution radius. Since we are working with data that were upscaled to the public region, the convolution process was not used. In this objective analysis, we want to see which forecast is more accurate in the positioning and the occurrence of an event. Thus, an objective analysis for two different total interest thresholds is needed. The first total interest threshold is equal to 0.99, which corresponds to a match when two objects share at least onepublic region. The objective analysis with this total interest threshold will indicate which forecast is more accurate in the positioning. The second total interest threshold is equal to 0.75, which roughly corresponds to a match when two objects are less than 100 km apart. In terms of public regions, the forecast object will be matched to the observation object if there is approximately less than

one, or if there is one public region that separates them. The objective analysis with this total interest threshold will indicate which forecast is more accurate for the occurrence of an event.

During each objective analysis, only one raw threshold, greater than zero, is used for the SW forecast. For the SWI index, the following raw thresholds are used: ≥ 10, ≥ 20, ≥ 30, ≥ 40, ≥ 50, ≥ 60, ≥ 70, ≥ 80, ≥ 90, and 100. Many different raw thresholds are used for the SWI index because we want to compare each different SWI index value to the SW forecast. Once the objective analysis is done for every forecast, the bootstrap method is used to compute the difference between the mean scores of the SWI index forecast and the mean scores of the SW forecast, and generate 90% bootstrap CI for the mean scores' difference.

The results of the bootstrap CI for the difference between the POD, FAR, HSS, PSS, ETS, and BIAS of the SWI index forecast and the SW forecast for the two different total interest thresholds can be seen in Figs. 5.8 and 5.9. The difference between the scores is always computed in the following way: the scores of the SWI index minus the scores of the SW forecast. For the scores that range from 0 to 1, 1 being a perfect forecast and 0 being a bad forecast, such as the POD, HSS, PSS, and ETS, to conclude that the SWI index forecast would improve the SW forecast, the 90% bootstrap CI of the mean score difference needs to contain only positive values. This would imply that the mean score of the SWI index forecast is always greater than the mean score of the SW forecast for every sample. In other words, it would mean that the SWI index forecast is usually better than the SW forecast. On the other hand, for the FAR, which ranges

from 0 to 1 — 0 being a perfect forecast and 1 being a bad forecast — to conclude that the SWI index forecast is better than the SW forecast, the 90% bootstrap CI of the mean score difference needs to contain only negative values. This would imply that the mean FAR of the SWI index forecast is always smaller than the mean FAR of the SW forecast for every sample and that the SWI index forecast is usually better than the SW forecast.

First, let us look to the images in the left column of Figs. 5.8 and 5.9 which correspond to the 90% bootstrap CIs of the mean scores' difference of the SWI index forecasts and the SW forecasts when the total interest threshold is 0.99. One can notice that the 90% bootstrap CIs of the score difference for the POD, HSS, PSS, and the ETS contain mostly negative values for almost every value of the SWI index. Therefore, for a total interest threshold of 0.99, the SW forecast done by a forecast is better than the SWI index forecast. In other words, the SW forecast is more accurate in the positioning of an SW event than the SWI index.

Now, we will focus on the images in the right column of Figs. 5.8 and 5.9, which correspond to the 90% bootstrap CIs of the mean scores' difference of the SWI index forecasts and the SW forecasts when the total interest threshold is 0.75. A clear tendency can be drawn from these images. For SWI index values from ≥10 to ≥60, the 90% bootstrap CIs of the mean score difference of the SWI index forecasts and the SW forecasts for the POD, HSS, PSS, and ETS are above the zero line, containing only positive values. Moreover, for SWI index values from ≥10 to ≥60, the 90% bootstrap CIs of the mean score's difference of the SWI index forecasts and the SW forecasts for the FAR contain mostly negative values.

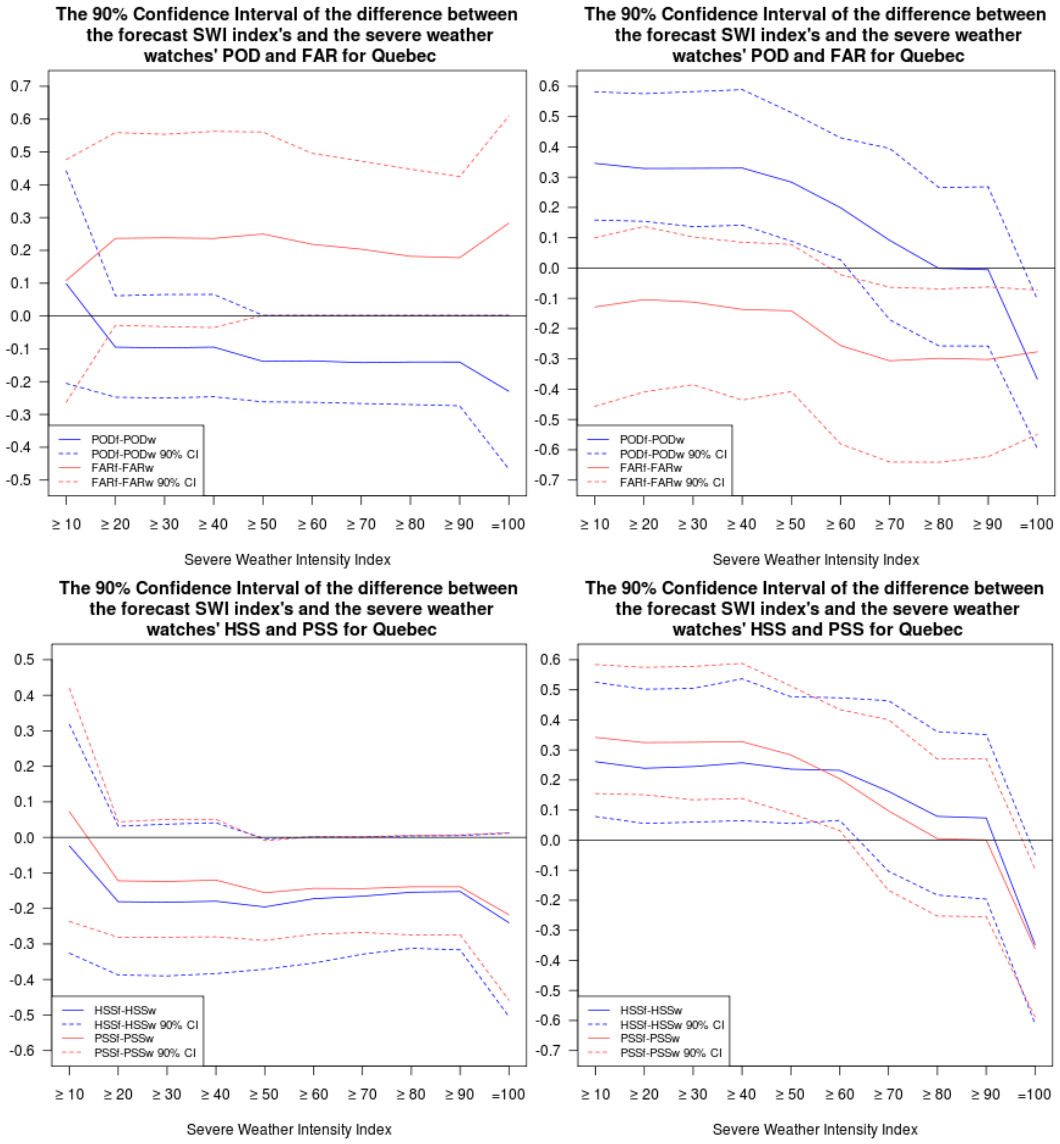

Fig. 5.8: The 90% bootstrap CI of the scores' difference of the SWI index forecasts and the SW watches for Quebec. The straight lines represent the bootstrap means. The lower and upper dashed lines are the 90% bootstrap CIs. In the top row, the difference between the POD of the SWI index forecasts (PODf) and the POD of the SW watches (PODw) is in blue, and the difference between the FAR of the SWI index forecasts (FARf) and the FAR of the SW watches (FARw) is in red. In the bottom row, the difference between the HSS of the SWI index forecasts (HSSf) and the HSS of the SW watches (HSSw) is in blue, and the difference between the PSS of the SWI index forecasts (PSSf) and the PSS of the SW watches (PSSw) is in red. Forecast or watch regions are matched to observation regions if they share at least one public region in common in the left column and if there is less than or one public region that separates them in the right column.

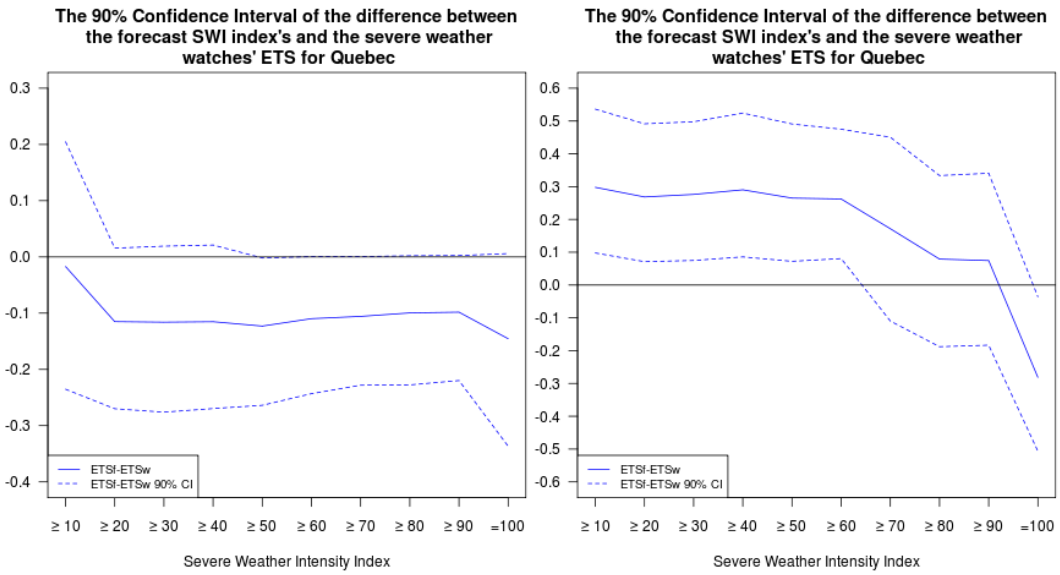

Fig. 5.9: The 90% bootstrap CI of the scores' difference of the SWI index forecasts and the SW watches for Quebec. The straight lines represent the bootstrap means. The lower and upper dashed lines are the 90% bootstrap CIs. The difference between the ETS of the SWI index forecasts (ETSf) and the ETS of the SW watches (ETSw) is in blue. Forecast or watch regions are matched to observation regions if they share at least one public region in common in the left column and if there is less than or one public region that separates them in the right column.

These results imply that the SWI index forecast for SWI index values from ≥10 to ≥60 is usually more accurate than the SW forecast. Therefore, the SWI index forecast is more accurate than the SW forecast done by a forecaster in the occurrence of a SW event.

Finally, the results of the objective analysis with the smaller distance tolerance show that the SWI index forecast would not improve the positioning of the SW forecast. However, the objective analysis with a greater distance tolerance clearly demonstrates that the SWI index forecast more accurately predicts the occurrence of SW in comparison to the SW forecast. Therefore, the SWI index forecast would be useful to a SW forecaster, since it indicates the likelihood of

SW occurrence and would give confidence to the forecasters in situations where it is difficult to decide whether or not to emit a SW watch. It seems clear that the SW forecaster's ability to position the SW watches cannot be improved with the approach proposed in this thesis.

Chapter 6

Discussions

6.1 Forecasts v. observations

In general, it is hard to get significant scores and statistics for rare events since there is not enough data available to do the verification, as was observed in the results from Section 5.1. The scarcer the data, the less representative the scores will be. Another important fact to keep in mind for SW observations is that there are no SW observations if there is nobody on location to report it. Therefore, SW observations are closely related to population density. This is quite obvious when Figs. 6.1 and 6.2 are compared. As a result, our domain of interest had to be chosen in order to focus on areas with a high population density. Our three domains of interest all have some areas that are less populated. However, this is less important over the Southern Ontario and Southern Quebec domain than over the Alberta domain. Another important fact for the Southern Ontario and Southern Quebec region is that the SW observations over the US compensate for the lack of

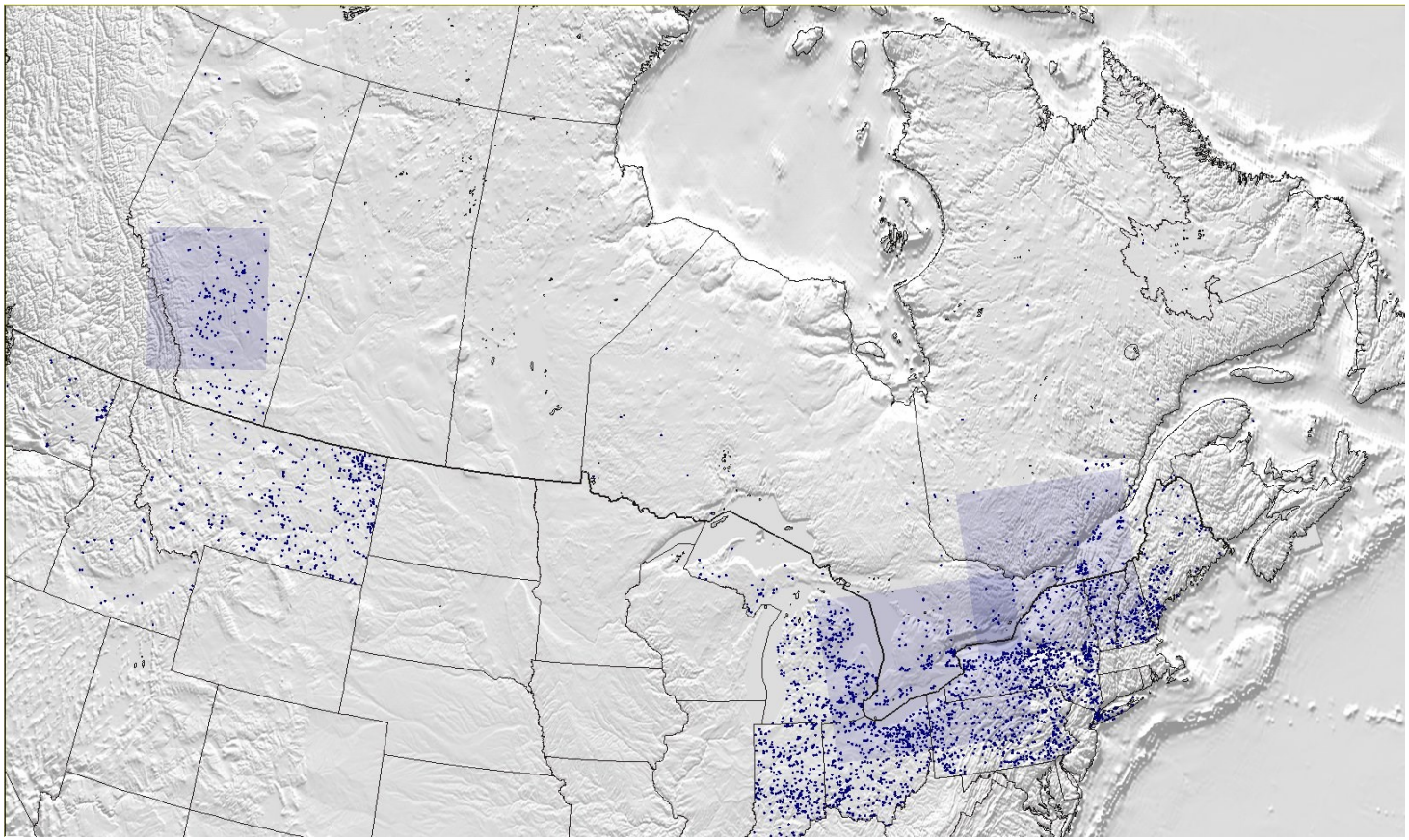

Fig. 6.1: SW observations for the summer of 2008 and the three domains of interest. The SW observations of the summer of 2008 over Alberta, Ontario, Quebec, and the states of Michigan, Indiana, Ohio, Pennsylvania, New York, Vermont, New Hampshire, Maine, Washington, Idaho, and Montana are identified as blue dots. The three domains of interest — Alberta, Southern Ontario, and Southern Quebec — are identified by the light purple square.

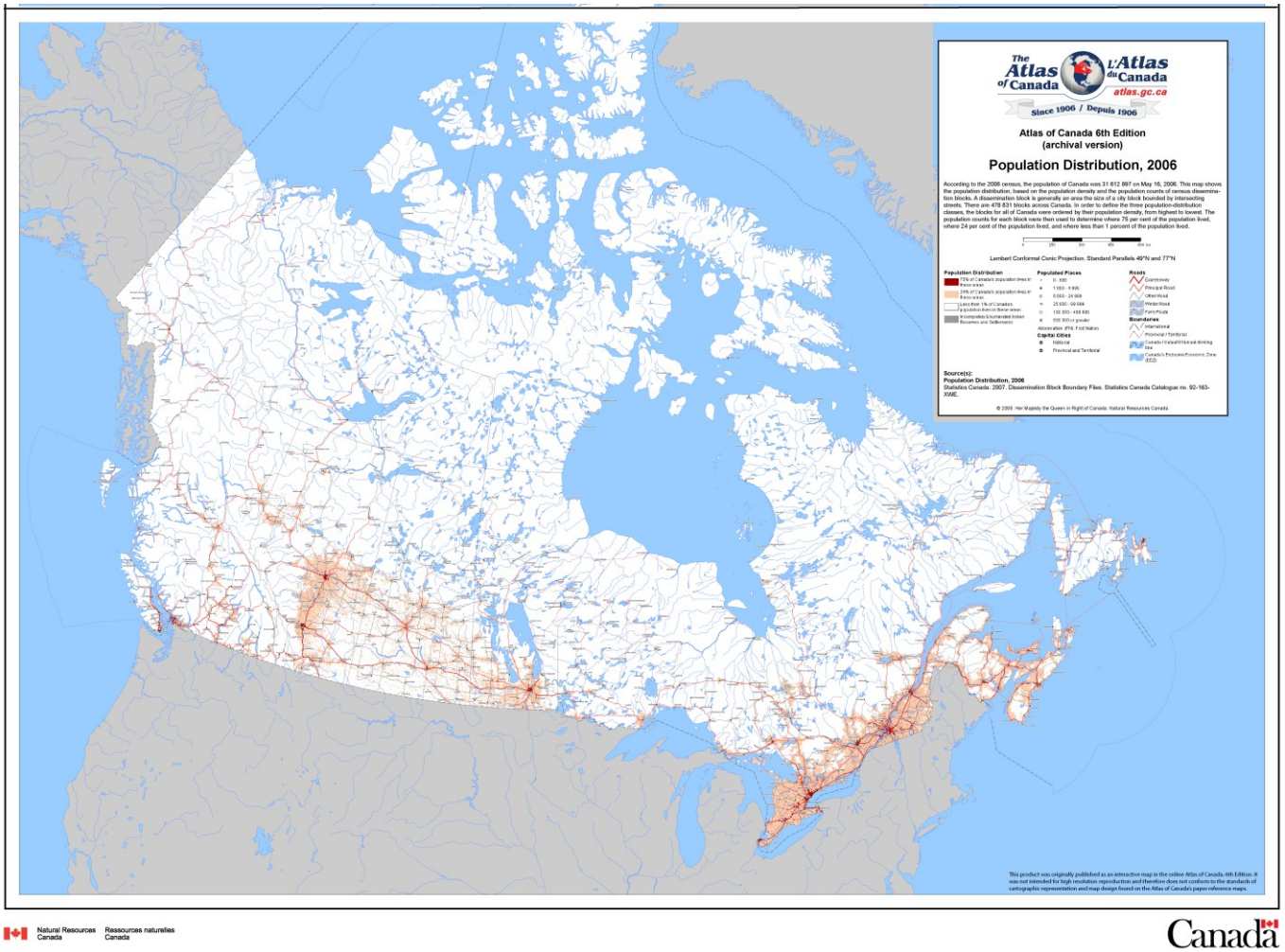

Fig. 6.2: Population density in 2006. The image is from the Natural Resource of Canada.

observations over the Canadian portion of the domain, because the US SW observations are really dense over these two domains. On the other hand, 1/3 of the Alberta domain has a very low population density. It is easily noticeable by observing Fig. 6.1 that the Alberta domain contains a lot less SW observations than the other two domains. This can partly explain the reason that over the Ontario domain, the SWI index forecast has the best scores, the one over Southern Quebec has the second best scores, and the one over the Alberta domain has the worst scores. When it was time to choose my domains of interest, I really chose the domain according to the population density and the domain of the GEM-LAM 2.5-km for Southern Ontario and Southern Quebec. However, for the Alberta domain, I took the domain used by the UNSTABLE project and this was the best choice since by including the Rockies the model better capture the important mesoscale processes in its foothills that often lead to severe convection. However, for the summer of 2008 and 2009, the eastern edge of the GEM-LAM 2.5-km domain limited us to position our Alberta domain. Presently, it would be possible to increase the size of the Alberta domain to include more populated regions because the GEM-LAM 2.5-km domains have been enlarged since the fall of 2011 (Rombough et al., 2010; Giguère and Milbrandt, 2011). It would be interesting in the near future to change the Alberta domain and redo an objective analysis for a more recent summer to compare the results.

For the three domains, the scores were affected by the scarcity of the SW observations. As we have concluded earlier, this is not really important for the Southern Ontario domain and has little importance for the Southern Quebec region, but it is really important for the Alberta domain. Therefore, it would have

been really interesting to have the radar data for the summer of 2008, because it could have compensated for the lack of data for certain regions as observed in the subjective analysis. We would certainly have different scores if we would have had access to radar data. Presently, at the High Impact Weather National Laboratory of EC, there is a project called the Canadian Precipitation Analysis (CaPA), and for the needs of this project, all the Canadian and US radar data has been archived since the summer of 2012. Therefore, it would be important in the near future to run the model and our SWI index algorithms for more recent years for which we have access to archived radar data, to do a more complete objective analysis. Radar data could be used in many different ways. Radar algorithms could be applied on the radar data to detect and identify SW features. In addition, they could be used to complete the SW observations by associating a thunderstorm line on the radar to a SW observation. In that way, we would no longer have point observation. Moreover, a threshold applied to the reflectivity could be used to detect severe echoes and high accumulation areas to associate them to SW. However, further investigation is needed before using the radar data in order to identify the best way to use these data for this research. Then, one could compare the new scores to the ones from our previous analysis and see if better results are obtained. If no better results are obtained over Alberta with the new analysis, it could mean that there is something wrong with the decision tree of our SWI index for Alberta and that we did not identify the important severe thunderstorm elements as well as we did for the other two regions. On the other hand, it could mean that the model is less accurate over this region.

The spin up of the model has had some impact on our scores, as observed with the objective analysis. The GEM-LAM 1-km is initialized at 15 UTC for all three domains. Moreover, it takes approximately three hours for the model to spin-up. For Alberta, 15 UTC correspond to 9 AM locally, and it corresponds to 11 AM locally for Southern Ontario and Southern Quebec. As we can see, the spin up time does not really affect the Alberta domain, since the convection is usually initiated after the spin up period of the model. However, for Southern Ontario and Southern Quebec, the convection can be initiated during the spin up period of the model. In the near future, the GEM-LAM 2.5-km will be pan-Canadian and will have multiple runs. Therefore, we will be able to initialize the GEM-LAM 1-km earlier for Southern Ontario and Southern Quebec, so that the spin up period would usually not fall during the initiation of convection.

In addition, we did not have a complete model dataset for the summer of 2008. We used the experimental GEM-LAM 1-km, but more importantly, it was one of the first versions of this model. As we were using it, we discovered that there were some problems in the code. On some days, the model run could not come to completion due to a division by zero. Most days where the model failed to complete its run were severe thunderstorms days. Therefore, for some of the few SW observations that we had, we could not even do the verification of our index because we did not have any model outputs for that day. It certainly had an impact on our scores. I suggest for future works to use the more recent version of the GEM-LAM 1-km, which hopefully will be problem-free and will give us a model run for every day that we need.

Finally, for all three regions, the results from the objective verification show that, on then different values of the SWI index, there are approximately four or five for which there is larger difference in the scores. Therefore, it is possible that our decision tree should not have as many categories. Mainly for the three domains, the most difference in the scores is observed for these groups of SWI index values: from 10 to 50, 60 to 90, and 100. Consequently, a color chart index indicating three categories of intensity for severe thunderstorms — weak, moderate, high — might be more adequate.

6.2 Forecasts v. severe thunderstorm watches

As mentioned earlier, high-resolution models are rarely accurate in the position of an event. However, they are often useful to determine the occurrence of an event. As mentioned in the previous discussion section, having access to the radar data would have most certainly impacted the results when comparing the position accuracy of the SWI index forecasts with the SW forecasts. For example, severe thunderstorm lines could have been identified, which could have impacted the results on the location accuracy of the index, since a line can affect more than one public region as opposed to a point observation. Thus, it would be interesting to perform the same objective analysis from Section 5.2 with a dataset where the radar data is available, to see if there is a difference in the accuracy of the position. Moreover, it would be interesting to do the same comparison, but for Southern Ontario and Alberta. It was easier to do the comparison for the Southern

Quebec domain, since SW forecasts at the QSPC are archived on paper and I had physical access to them.

One of the main objectives of the Next Generation Weather Prediction System project at EC is to provide the users with forecasts and other information on higher-resolution grids to give more precision on the location and size of the region affected by an event. During the subjective analysis of the SWI index with the SW observations and the radar images, I noticed that the SWI index forecast usually indicates whether the severe thunderstorms will be localized or widespread. Therefore, the SWI index forecast might not help the forecaster to position a SW event, but it could give an insight to the forecasters if the expected severe thunderstorms are extensive or localized. Therefore, if in the near future, the warning public regions are either decreased in scale or are transformed to warning/watch objects drawn by a forecaster, the high-resolution SWI index forecast could help the forecasters to refine the watch area, since the GEM-LAM 1-km simulates severe thunderstorm lines and localized severe thunderstorms well.

Having access to radar data would enable us to include another important object's attribute during the verification: the object's area. It would be really interesting to statistically measure the accuracy of the SWI index to indicate whether the severe thunderstorms will be localized or widespread. Also, it would be important to compare the accuracy of the area of the SWI index forecast and the SW watch area to see if the SWI index could help the forecaster to refine a SW watch area. If it could, it would be a major step toward the objectives of the Next Generation Weather Prediction System project at EC.

Chapter 7

Conclusions

In conclusion, the scores and their 90% bootstrap CIs calculated from the objective verification of the SWI index forecasts with the SW observations demonstrate that the SWI index has skill for the Southern Ontario and Southern Quebec domains, but much less for the Alberta domain. However, the subjective analysis of the SWI index forecasts with the SW observations and radar images demonstrates that, as mentioned in the discussion, it is partly due to the scarcity of the SW observations and further verification needs to be done for more recent years which have available radar data. Mostly from the subjective verification, we can conclude that the SWI index forecast would be useful to Alberta SW forecasters. On the other hand, from the results of objective and subjective verification of the SWI index forecasts with the SW observations for the Southern Ontario and Southern Quebec domain, we can conclude that the SWI index forecast would be helpful for SW forecasters to forecast SW.

To verify that the SWI index forecast would help the SW forecasters to improve their SW forecasts, an objective verification of the SW forecasts done by a forecaster with the SW observations, and the SWI index forecasts with the SW observations was done. The results showed that the SWI index forecast would help the SW forecasters to forecast the occurrence of SW events, but would not improve the localization of an event. However, as mentioned earlier, since the model forecasts severe thunderstorm lines and localized severe thunderstorms

well, the SWI index forecast may help the forecasters to refine smaller watch regions when the next generation of the weather prediction system is implemented at EC.

The goal of this thesis was to develop an automated tool from a high-resolution model to help the forecaster to forecast SW. From the results of this research, I truly believe that the SWI index could greatly help the Alberta, Ontario, and Quebec SW forecasters to forecast SW. Therefore, the next step should be to introduce the index to the operational forecaster at EC and make an experimental forecast of the SWI index available.

My future work will concentrate on the adaptation of my algorithms to the operational GEM-LAM 2.5-km to generate a SWI index forecast from the GEM-LAM 2.5-km outputs. Afterward, the object-oriented method will be used to verify the accuracy of the SWI index forecasts from the GEM-LAM 2.5-km outputs with the SW observations, and most probably the radar data as well. I also wish to be able to run the GEM-LAM 1-km over the same period as the GEM-LAM 2.5-km and perform the same objective verification as performed on the GEM-LAM 2.5-km to compare their scores and deduce if the SWI index is more accurate for one model than the other.

References

Atkins, N. T., and R. M. Wakimoto, 1991: Wet Microburst Activity over the Southern United States: Implications for Forecasting. *Wea. Forecasting,* **6**, 470-482.

Auer, A. H. Jr., and W. Sand, 1966: Updraft Measurements Beneath the Base of Cumulus and Cumulonimbus Clouds. *J. Appl. Meteor.*, **5**, 461-466.

Bidner, A., 1971: The AFGWC Severe-Weather-Threat (SWEAT) index (A preliminary report). Air Weather Service Tech Rep. 242, 229-231.

Blanchard, D. O., 1998: Assessing the Vertical Distribution of Convective Available Potential Energy. *Wea. Forecasting,* **13**, 870-877.

Bluestein, H. B., and K. W. Thomas, 1984: Diagnosis of a Jet Streak in the Vicinity of a Severe Weather Outbreak in the Texas Panhandle. *Mon. Wea. Rev.,* **112**, 2499-2520.

Brasseur, O., 2001: Development and application of a physical approach to estimating wind gusts. *Mon. Wea. Rev.,* **129,** 5–25.

Brown, R. A., 1992: Initiation and Evolution of Updraft within an Incipient Supercell Thunderstorm. *J. Atmos. Sci.,* **49**, 1997-2014.

Brown, B. G., J. L. Mahoney, C. A. Davis, R. Bullock, and C. K. Mueller, 2002: Improved approaches for measuring the quality of convective weather forecasts. *16th Conf. on Probability and Statistics in the Atmospheric Sciences*, Orlando, FL, Amer. Meteor. Soc., 20–25.

Brown, B. G., R. G. Bullock, J. H. Gotway, D. Ahijevych, C. A. Davis, E. Gilleland, and L. Holland, 2007: Application of the MODE object-based verification tool for the evaluation of model precipitation fields. *Preprints, 22nd Conf. on Weather Analysis and Forecasting/18th Conf. on Numerical Weather Prediction,* Park City, UT, Amer. Meteor. Soc., 10A.2. [Available online at http://ams.confex.com/ams/pdfpapers/124856.pdf]

Browning, K. A., 1965: The Evolution of Tornadic Storms. *J. Atmos. Sci.*, **22**, 664-668.

Burgess, D. W., and R. A. Brown, 1973: The structure of a severe right moving thunderstorms: New single-Doppler radar evidence. *Preprints, Eighth Conf. on Severe Local Storms*, Denver, Amer. Meteor. Soc., 99-106.

Burgess, D. W., V. T. Wood, and R. A. Brown, 1982: Mesocyclone evolution statistics. Preprints, *12th Conf. Severe Local Storms*, Amer. Meteor. Soc., 422-424.

Byers, H. R., and R. R. Braham, Jr., 1949: *The Thunderstorm.* U.S. Government Printing Office, Washington, DC, 287 pp.

Cai, H., 2005: Comparison between Tornadic and Nontornadic Mesocyclone Using the Vorticity (Pseudovorticity) Line Technique. *Mon. Wea. Rev.*, **133**, 2535-2551.

Chandik, J. F., and W. A. Lyons, 1971: Thunderstorms and the lake breeze front. *Preprints, Seventh Conf. on Severe Local Storms,* Kansas City, Amer. Meteor. Soc., 218-225.

Changnon, S. A., Jr., 1977: Urban effects on severe local storms at St. Louis. *Preprints, Tenth Conf. on Severe Local Storms,* Omaha, Amer. Meteor. Soc., 212-217.

Charney, J. G., and N. A. Phillips, 1953: Numerical integration of the quasi-geostrophic equations for barotropic and simple baroclinic flows. *J. Meteor.*, **10**, 71–99.

Chen, C.-S., 1980: The effect of the gust front on the generation of new convection. Ph.D. thesis, University of Illinois, 192pp.

Chernick, M. R., 1999: *Bootstrap Methods*, *A Practitioner's Guide*. Wiley, New York, 264 pp.

Chu, C. M., and Y. L. Lin, 2000: Effects of orography on the generation and propagation of mesoscale convective systems in a two-dimensional conditionally unstable flow. *J. Atmos. Sci.*, **57**, 3817-3837.

Clark, A. J., W. A. Gallus, and T.-C. Chen, 2007: Comparison of the Diurnal Precipitation Cycle in Convection-Resolving and Non-Convection-Resolving Mesoscale Models. *Mon. Wea. Rev.*, **135**, 3456–3473.

Colby, F. P., Jr., 1984: Convective inhibition as a predictor of convection during AVE-SESAME II. *Mon. Wea. Rev.,* **112**, 2239-2252.

Côté, J., S. Gravel, A. Méthot, A. Patoine, M. Roch, and A. Staniforth, 1998: The Operational CMC/MRB Global Environmental Multiscale (GEM) Model. Part I: Design Considerations and Formulations. *Mon. Wea. Rev.*, **126**, 1373-1395.

Davies-Jones, R. P., D. W. Burgess, and M. Foster, 1990: Test of helicity as a tornado forecast parameter. Preprints, *16th Conf. On Severe Local Storms,* Kananaskis Park, AB, Canada, Amer. Meteor. Soc., 588-592.

Davies-Jones, R., 2002: Linear and Nonlinear Propagation of Supercell Storms. *J. Atmos. Sci.*, **59**, 3178-3204.

Davis, C., B. Brown, and R. Bullock, 2006: Object-Based Verification of precipitation Forecasts. Part I: Methodology and Application to Mesoscale Rain Areas. *Mon. Wea. Rev.,* **134**, 1772-1784.

Davis, C. A., B. G. Brown, R. Bullock, and J. Halley-Gotway, 2009: The Method for Object-Based Diagnostic Evaluation (MODE) Applied to Numerical Forecasts from the 2005 NSSL/SPC Spring Program. *Wea. Forecasting*, **24**, 1252-1267.

Desrochers, P. R., and R. J. Donaldson, Jr., 1992: Automatic Tornado Prediction with an Improved Mesocyclone-Detection Algorithm. *Wea. Forecasting,* **7**, 373-388.

Donaldson, R. J., Jr., G. M. Armstrong, A. C. Chmela and M. J. Kraus, 1969: Doppler radar investigation of air flow and shear within severe thunderstorms. Preprints, *6th Conf. on Severe Local Storms,* Chicago, Amer. Meteor. Soc., 146-154.

Donaldson, R. J., Dyer, R. M. and M. J. Kraus, 1975: An objective evaluator of techniques for predicting severe weather events. Preprints*, Ninth Conf. on Severe Local Storms,* Norman, Oklahoma. Amer. Meteor. Soc., 321-326

Doswell, C. A., III, 1987: The distinction between large-scale and mesoscale contribution to severe convection: A case study example. *Wea. Forecasting*, **2**, 3-16.

Doswell, C. A., III, and E. N. Rasmussen, 1994: Notes and Correspondence: The Effect of Neglecting the Virtual Temperature Correction on CAPE Calculations. *Wea. Forecasting*, **9**, 625-629.

Duda, J. D., and W. A. Gallus, Jr., 2010: Spring and Summer Midwestern Severe Weather Reports in Suppercells Compared to Other Morphologies. *Wea. Forecasting*, **25**, 190-206.

Efron, B., and R. J. Tibshirani, 1993: *An Introduction to the Bootstrap*, Chapman & Hall, New York, 436 pp.

Environnement Canada, 2010: Critères d'avertissements publics. http://ec.gc.ca/meteo-weather/default.asp?lang=Fr&n=D9553AB5-1. Accessed on May 18th 2011.

Environment Canada. 2011: *Upgrade to the high resolution deterministic prediction system (HRDPS version 2.2.0) at the Canadian Meteorological Center*. http://dd.weatheroffice.ec.gc.ca/doc/genots/2011/09/19/NOCN03_CWAO_191510___14080. Accessed on January 1st 2013.

Evans, J. E., and M. E. Weber, 2000: Weather Radar Development and Application Programs. *Lincoln Laboratory Journal,* **12**, 367-382.

Foot, G. B., 1984: Influence of gust fronts on the propagation of storms. *Proc. Ninth Int. Cloud Physics Conf.,* Tallin-Estonia, USSR, Academy of Sciences of the USSR, 419-422.

Frenette, R., 2006: Évaluation du programme de diagnostique d'orage. Rapport interne du Laboratoire national des conditions météorologiques menaçantes, Environnement Canada, 29 pp.

Galway, J. G., 1956: The lifted index as a predictor of latent instability. *Bull. Amer. Meteor. Soc.,* **37**, 528-529.

Galway, J. G., 1958: Composite charts for tornado situations under northwest flow aloft, 24 pp. [Unpublished report available from National Weather Service, Central Region, Scientific Services Division, Kansas City.]

George, J. J., 1960: Weather Forecasting for Aeronautics, Academic Press, 673 pp.

Giguère, A., and J. Milbrandt, 2011: DRAFT: The Experimental High Resolution Deterministic Prediction System (v_2.2.0) Technical Summary of the 22 September 2011 Upgrade. Development and Operations divisions at the Canadian Meteorological Center Report, Environment Canada, 30 pp.

Gilbert, G. K., 1884: Finley's tornado predictions. *Amer. Meteor. J.*, **1**, 166-172.

Haltiner, G. J., and R. T. Williams, 1980: Numerical Prediction and Dynamic Meteorology, 2nd ed.: Wiley, New York, 477 pp.

Hart, J. A., and W. D. Korotky, 1991: The SHARP workstation user's manual−v1.50. A skew/hodograph analysis and research program for the IBM and compatible PC. *NOAA/NWS Forecast Office*, Charleston, WV*,* 62 pp.

Heidke, P., 1926: Calculation of the success and goodness of strong wind forecasts in the storm warning service. *Geogr. Ann. Stockholm*, **8**, 301-349.

High Resolution GEM-LAM Visualization Platform, 2009: http://web-mrb.cmc.ec.gc.ca/~armngr8/unstable/. Accessed on February 21st 2010.

Hudson, H. R., 1971: On the relationship between horizontal moisture convergence and convective cloud formation. *J. Meteor.,* **10**, 752-755.

Joe, P., D. Burgess, R. Potts, T. Keenan, G. Stumpf and A. Treloar, 2004: The S2K Severe Weather Detection Algorithms and their Performance. *Wea. Forecasting,* **19**, 43-63.

Kain, J. S., S. J. Weiss, J. J. Levit, M. E. Baldwin and D. R. Bright, 2004: Examination of Convection-Allowing Configurations of WRF Model for the Prediction of Severe Convective Weather: The SPC/NSSL Spring Program 2004. *Wea. Forecasting,* **21**, 167-181.

Kyselý, J., 2008: *Notes and Correspondance* : A Cautionary Note on the Use of Nonparametric Bootstrap for Estimating Uncertainties in Extreme-Value Models. *J. Appl. Meteorol. Clim.,* **47**, 3236-3251.

Kitzmiller, D. H., W. E. McGovern and R. E. Saffle, 1995: The WSR-88D Severe Weather Potential Algorithm. *Wea. Forecasting,* **10**, 141-159.

Klemp, J. B., and R. B. Wilhelmson, 1978: Simulations of Right- and Left-Moving Storms Produced Through Storm Splittng. *J. Atmos. Sci.*, **35**, 1097-1110.

Kloth, C. M., and R. P. Davies-Jones, 1980: The relationship of the 300 mb jet stream to tornado occurrence. NOAA Tech. Memo. ERL-NSSL-88, National Severe Storms Laboratory, Norman, 66 pp.

Maddox, R. A., and C. A. Doswell III, 1982: An examination of jet stream configuration, 500 mb vorticity advection and low level thermal advection patterns during extended periods of intense convection. *Mon. Wea. Rew.,* **110**, 184-197.

Mailhot, J., S. Bélair, M. Charron, C. Doyle, P. Joe, M. Abrahamowicz, N. B. Bernier, B. Denis, A. Erfani, R. Frenette, A. Giguère, G. A. Isaac, N. McLennan, R. McTaggart-Cowan, J. Milbrandt, and L. Tong, 2010: Environment Canada's Experimental Numerical Weather Prediction Systems for the Vancouver 2010 Winter Olympic and Paralympic Games. *Amer. Meteor. Soc.*, 1073-1085.

Marwitz, J. D., 1972: The structure and motion of severe hailstorms, Part II. Multicell storms. *J. Appl. Meteor.*, **11**, 189-201.

McCann, D. W., 1994: WINDEX−A New Index for Forecasting Microburst Potential. *Wea. Forecasting*, **9**, 532-541.

McDonald, M., 2000: Cold core tornadoes: A forecasting technique. Prairie Storm Prediction Centre Internal Rep., Environment Canada, 7 pp.

McNulty, R. P., 1995: Severe and Convective Weather: A Central Region Forecasting Challenge. *Wea. Forecasting,* **10**, 187-202.

Mesinger, 1984: A blocking technique for representation of mountains in atmospheric models. *Revista di Meteorologica Aeronautica,* **XLII**, 196-202.

Milbrandt, J. A., and M. K. Yau, 2005: A Multimoment Bulk Microphysics Parameterization. Part II: A Proposed Three-Moment Closure and Scheme Description. *J. Atmos. Sci.,* **62**, 3065-3081.

Miller, R. C., 1972: Notes on analysis and severe-storm forecasting procedures of the Air Force Global Weather Central. AWS Tech. Rep. 200 (rev), Air Weather Service, Scott AFB, IL, 190 pp.

Mogil, H. M., and H. S. Groper, 1976: On the short-range prediction of localized excessive convective rainfall. Preprints, First Conf. on Hydrometeorology, Ft Worth, Amer. Meteor. Soc., Boston, 9-12.

Moncrieff, M. W., and M. J. Miller, 1976: The dynamics and simulation of tropical cumulonimbus and squall lines. *Quart. J. Roy. Meteor. Soc.,* **102**, 373-394.

National Weather Service, 2009: Mesoscale Analysis Parameter Description. *NOAA*. http://www.erh.noaa.gov/btv/mesoanalysis/description.shtml. Accessed on August 8th 2010.

Newman, W. R., 1972: The relationship between horizontal moisture convergence and severe thunderstorm occurrence. M.S. thesis, University of Oklahoma, 54 pp.

Pappas, J. J., 1962: A Simple Yes-No Hail Forecasting Technique. *J. Appl. Meteor.,* **1**, 353-354.

Phillips, N. A., 1957: A coordinate system having some special advantages for numerical forecasting. *J. Meteor.,* **14**, 184-185.

Pierce, C. S., 1884: The numerical measure of the success of predictions. *Science*, **4**, 453-454.

Rauber, R. M., J. E. Walsh and D. J. Charlevoix, 2005: Severe and Hazardous Weather: An Introduction to High Impact Meteorology. *Kendall/Hunt Publishing Company*. Dubuque, Iowa.

Rombough, H., H. Greene, B. Niska-Aro, B. Power, D. Schmidt, O. Stachowiak, C. Wielki, and A. Yun, 2010: GEM-LAM Convective Forecasts: How Can they be used in an Operational Forecast Environment? *25th Conf. on Severe Local Storms,* AB, Canada, Amer. Meteor. Soc., P4.19. [Available online at https://ams.confex.com/ams/pdfpapers/176251.pdf].

Roy, G., V. Turcotte and M.-A. Chartier, 2007: Vérification des algorithmes radars du Gem Lam 2.5 km. Rapport interne du Laboratoire national des conditions météorologiques menaçantes, Environnement Canada, 31 pp.

Sander, F., and R. J. Paine, 1975: The structure and thermodynamics of an intense mesoscale convective storm in Oklahoma. *J. Atmos. Sci.,* **32**, 1563-1579.

Showalter, A. K., 1953: A stability index for thunderstorm forecasting. *Bull. Amer. Meteor. Soc.,* **34**, 250-252.

Taylor, N., D. Sills, J. Hanesiak, J. Milbrandt, C. Smith, G. Strong, S. Skone and P. McCarthy, 2008: The UNderstanding Severe Thunderstorms and Alberta Boundary Layers Experiment: 2008 Pilot Experiment Operations Plan. http://www.umanitoba.ca/faculties/environment/envirogeog/weather/unstable/Operations/2008_OpsPlan_Final.doc. Accessed on June 6th 2013.

Taylor, N. M., D. M. L. Sills, J. M. Hanesiak, J. A. Milbrandt, C. D. Smith, G. S. Strong, S. H. Skone, P. J. McCarthy, and J. C. Brimelow, 2010: The Understanding Severe Thunderstorms and Alberta Boundary Layers Experiment (UNSTABLE) 2008. Submitted to *Bull. Amer. Meteor. Soc.*.

Trapp, R. J., G. J. Stumpf, and K. L. Manross, 2005: A Reassessment of the Percentage of Tornadic Mesocyclones. *Wea. Forecasting,* **20**, 680-686.

Turcotte, V., 2007 : Algorithmes d'orages violents pour la saison 2007. Rapport interne du Laboratoire national des conditions météorologiques menaçantes, Environnement Canada, 6 pp.

Turcotte, V., and D. Vigneux, 1987: Severe thunderstorm and hail forecasting using derived parameters from standard RAOB data. Preprints, *Second Workshop on Operational Meteor.,* Halifax, Nova Scotia, Canada, Atmos. Env. Serv./Canadian Meteor. And Oceanogr. Soc., 142-153.

Uccellini, L. W., 1975: A case study of apparent gravity wave initiation of severe convective storms. *Mon. Wea. Rev.,* **103**, 497-513.

Uccellini, L. W., and D., R. Johnson, 1979: The coupling of upper and lower tropospheric jet streaks and implications for the development of severe convective storms. *Mon. Wea. Rev.,* **107**, 682-703.

Vaillancourt, P., 2006a: Rapport d'application des indices de temps violent du CMC et d'autres centres de prévision au modèle GEM à résolution de 15 km. Rapport interne du Laboratoire national des conditions météorologiques menaçantes, Environnement Canada, 32 pp.

Vaillancourt, P., 2006b: Rapport d'application des critères radar au modèle GEM-LAM à résolution de 2.5 km. Rapport interne du Laboratoire national des conditions météorologiques menaçantes, Environnement Canada, 49 pp.

Vaillancourt, P., L. Fillion, J. St-James, A. Patoine, M. Reszka, M. Tanguay, M. Lajoie, A. Plante, A. Zadra, R. Mctaggart-Cowan, C. Creese, L. Lam, A. Rahill, S. Roy, and V. Thomas, 2012 : Amélioration du système

régional de prévision déterministe (SRPD) de la version 2.0.0 à la version 3.0.0. http://collaboration.cmc.ec.gc.ca/cmc/cmoi/product_guide/docs/lib/op_systems/doc_opchanges/technote_rdps300_20121003_f.pdf. Accessed on June 6th 2013.

Vaisiloff, S. V., E. A. Brandes, R. P. Davies-Jones, and P. S. Ray, 1986 : An Investigation of the Transition from Multicell to Supercell Storms. *J. Climate Appl. Meteor.*, **25**, 1022-1036.

Verkaik A., and J. Verkaik, 2000: Severe Weather Watcher Handbook: A Guide for Identifying and Reporting Summer Severe Weather. *Federal Minister of Environment.* Elwood, Ontario.

Wakimoto, R. M., 1985: Forecasting Dry Mircroburst Activity over the High Plains. *Mon. Wea. Rev.,* **113**, 1131-1143.

Weisman, M. L., and J. B. Klemp, 1982: The dependence of numerically simulated convective storms on vertical wind shear and buoyancy. *Mon. Wea. Rev.*, **110**, 504-520.

Weisman, M. L., and J. B. Klemp, 1984: The structure and classification of numerically simulated convective storms in directionally varying wind shears. *Mon. Wea. Rev.*, **112**, 2479-2498.

Weisman, M. L., and J. B. Klemp, 1986: Characteristics of isolated convective storms. *Mesoscale Meteorology and Forecasting,* P. S. Ray, Ed., Amer. Meteor. Soc., 331-358.

Weisman, M. L., and R. Rotunno, 2000: The use of vertical wind shear versus helicity in interpreting supercell dynamics. *J. Atmos. Sci.*, **57**, 1452-1472.

Weiss, C. E. and J. F. W. Purdom, 1974: The effect of early morning cloudiness on squall-line activity. *Mon. Wea. Rev*, **102**, 400-402.

Yager R. R., S. Ovchinnikov, R. M. Tong, and H. T. Hguyen, 1987: *Fuzzy sets and Applications, Selected Papers by L.A. Zadeh*. John Wiley and Sons, 685 pp.